A CALORIMETRIC STUDY ON NUCLEAR REACTOR MATERIALS AT HIGH TEMPERATURES

KEIJI NAITO, HIDEAKI INABA and TSUNEO MATSUI

Department of Nuclear Engineering

(Received May 31, 1983)

Abstract

A review on the calorimetric studies of nuclear materials at high temperatures carried out recently in our laboratory is given. The apparatus used in this study are as follows; an adiabatic scanning calorimeter, a direct heating pulse calorimeter, an apparatus for measuring thermal conductivity by means of a scanning temperature method, a twin microcalorimeter of Tian-Calvet type, a time-of-flight mass-spectrometer with a Knudsen-cell, *etc.* Heat capacities of U_4O_{9-y}, U_3O_{8-z}, $Mn_xFe_{3-x}O_4$, $Cr_xFe_{3-x}O_4$, VO_x, NbO_2 and doped NbO_2 with various compositions have been measured and the mechanisms of phase transitions are discussed from the entropy changes due to the transitions as a function of composition. Thermal conductivities of U_4O_{9-y}, U_3O_{8-z} and $Mn_xFe_{3-x}O_4$ have been measured and discussed as a function of composition. Heats of formation of NbO_x with various x have been measured and the stability of the compounds is discussed in comparison with VO_x and Ta_2O_5. Vaporization of the niobium-oxygen system, Nb_2O_{5-x}, $NbO_{2\pm x}$, $NbO_{1\pm x}$, and Nb-O solid solution phases has been measured with emphasis on their nonstoichiometry. The congruently vaporizing phase in the niobium-oxygen system is determined to be NbO_2. The enthalpy of ormationf and dissociation energy for $NbO_2(g)$ and $NbO(g)$, enthalpy and entropy of fusion for $NbO_2(s)$ and $Nb_2O_5(s)$ and the partial molar enthalpy and entropy of oxygen in solid phases are determined from the vapor pressure data. The defect structure of Nb-O solid solution and $NbO_{2\pm x}(s)$ is discussed from the partial molar enthalpy and entropy of oxygen and the phase diagram of the niobium-oxygen system at high temperatures is presented.

CONTENTS

I . Introduction

The knowledge of thermal properties, such as heat capacity, vapor pressure, heat of formation, thermal conductivity, *etc.* at high temperatures is one of the most important informations for the research and development of refractory materials, since the physical and chemical integrities of the materials at high temperatures are mainly determined by these thermal properties.

Calorimetric study, as a part of our study in high temperature chemistry, on nuclear reactor materials has been carried out extensively in our laboratory, Department of Nuclear Engineering, Faculty of Engineering, Nagoya University, since 1968, and the provision of a new equipment, which consists of an adiabatic scanning type calorimeter, a Tian-Calvet type twin microcalorimeter and a mass spectrometer with a Knudsen vaporization cell, has been granted by the Ministry of Education, Science and Culture of Japan in 1977. Since then, the calorimetric studies on nuclear reactor materials have been still continued in our laboratory, making use of this equipment as well as some other apparatus we have developed (a direct heating pulse calorimeter, an apparatus for measuring thermal conductivity by means of scanning temperature method, *etc.*). The accumulation of results thus obtained has reached the point where a summary of these studies should be opportune.

The present review will cover the outline of apparatus we used, some of which have been designed in our laboratory, the heat capacity and thermal conductivity of uranium oxides, the heat capacity and thermal conductivity of ferrites, the calorimetric study of niobium oxides and vanadium oxides and the vaporization of the niobium-oxygen system, of which studies have been carried out mainly in recent five years since the provision of the equipment.

II . Apparatus

2. 1. Measurement of heat capacity

2. 1. 1. Adiabatic scanning calorimeter

Calorimetry at high temperatures has become important in the development of high temperature materials. Although drop calorimetry has been extensively used at high temperatures, this method requires a large number of drop measurements and it is furthermore not suitable to apply to the systems in which phase transitions or chemical reactions occur on heating. On the other hand, adiabatic calorimetry can determine directly the heat capacity at each temperature and can use for the study of phase transitions, but this method has been mainly used at low temperatures because of the increase of the heat exchange between the sample and the surroundings with increasing temperature.

Two methods of adiabatic calorimetry are known; one is the continuous (or dynamic) method and the other is the intermittent (or Nernst) method. The former is applicable not only for continuous measurement of heat capacity but also for measurement of reaction heat, but the correction for the heat leakage during measurement is difficult. The latter is tedious and takes a long time for the measurement and the use for chemical reaction systems is difficult, but the correc-

tion for the heat leakage during the measurement can be made precisely.

A precise absolute calorimetry at high temperatures is very difficult because the heat leakage between the sample and the surroundings increases rapidly with increasing temperature mainly due to radiation. In order to clarify the heat leakage in the dynamic calorimeter, we have measured the heat leakage at various conditions[1]: The heat leakage in a calorimeter with the two heating methods of the sample (internal heating and external heating) has been measured at various temperatures with various heating rates, and a result obtained at 773 K ander vacuum (~ 0.1 Pa) is shown in Fig. 1. It is seen from the figure that the heat leakage is proportional to heating rate and that the heat leakage with the internal heating is larger than that with the external heating. It is therefore concluded that the heat leakage is dependent on the heating rate and the external heating method is preferable in the view point of the heat leakage.

In the continuous heating method, a constant power is usually supplied to the sample, so that the heating rate hence the heat leakage depends on the heat capacity of the sample, especially when the sample has phase transitions. In order to make a precise absolute measurement regardless of the amount or kind of sample, we have developed an adiabatic scanning calorimeter as shown in Fig. 2[2], where the heating rate of the sample is controlled to be constant. The constant heating rate of the calorimeter can be achieved by using an electronic programmer: the difference between the voltage of the programmer and the electromotive force of a thermocouple in the sample vessel is brought to zero by controlling the power of an internal heater (external heating method) using a PID transistor driver type controller. Heating rate is usually chosen as 2 K min^{-1} and the error of the control is within ± 0.01 K min^{-1}. The voltage and current of the internal heater at each temperature are converted
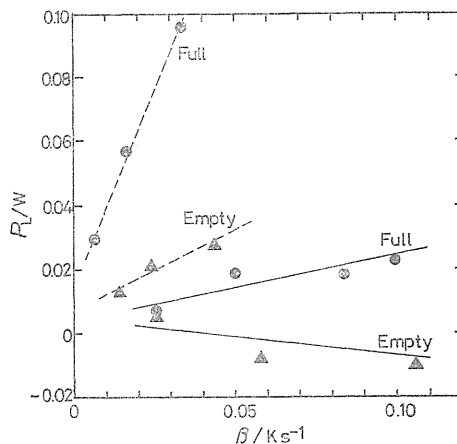
Fig. 1. Heat leak for the full and the empty calorimeter plotted against heating rate:[1] broken line, internal heating; solid line, external heating.
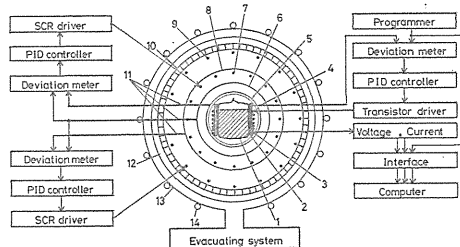
Fig. 2. Schematic drawing of the adiabatic scanning calorimeter.[2]
1. sample (in quartz vessel)
2. alumina bobbin
3. internal heater
4. thermocouple for program control
5. double platinum sphere
6. first adiabatic shield
7. first external heater
8. second adiabatic shield
9. second external heater
10. alumina thermal shield
11. thermocouples for adiabatic control
12. stainless thermal shield
13. stainless vessel
14. coolant system

into digital signals and stored in a disk using an on-line minicomputer OKITAC 50/40. The adiabatic control is made by using the two external heaters. The temperature difference between the inner vessel and the outer shield is detected by a differential thermocouple, and the difference is reduced to zero by controllng the power of the external heater, using a PID thyristor type controller. The adiabatic control is usually within ±0.01 K. The sample is sealed in a clean quartz cylindrical vessel, about 20 mm in diameter and 28 mm in height. The quartz sample vessel is filled with helium gas at a reduced pressure of about 2×10^4 Pa. Thermocouples used are inconel sheathed chromel-alumel, 0.5 mm in diameter. The measurement is made in an inert gas atmosphere at reduced pressure (400∼1300 Pa). Measurement can also be made below room temperature: the system is cooled by filling it with about two liters of liquid nitrogen and evacuated before the measurement begins.

As a standard sample, alumina of 13.102 g provided by U. S. National Bureau of Standard is used and the results are shown in Fig. 3,[2] where the data by Furukawa et al.[3] are also shown in a solid line for comparison. The imprecision of the measurement is within ±1% and inaccuracy is seen from Fig. 3 to be within ±2%. This imprecision and inaccuracy is considered to be satisfactory for the absolute measurement of heat capacity at high temperatures. The systematic error in the measurement with other samples can be corrected by the measurement with a standard sample as shown in Fig. 3.

The dehydration reaction of hydrated cupric sulphate ($CuSO_4 . 5H_2O$) has been studied[2] as a typical example of a sample in which chemical reaction occurs. $CuSO_4 . 5H_2O$ of chemically pure grade was sifted by a 200 mesh, and 100 mg of the powder was uniformly mixed with about 3.8 g of alumina powder. The measurements were made in a nitrogen atmosphere at about 1 kpa and at heating rates of 1, 2, 4 and 8 K min^{-1}. The results are shown in Fig. 4. The dehydration reaction of $CuSO_4 . 5H_2O$ is believed to be as follows:
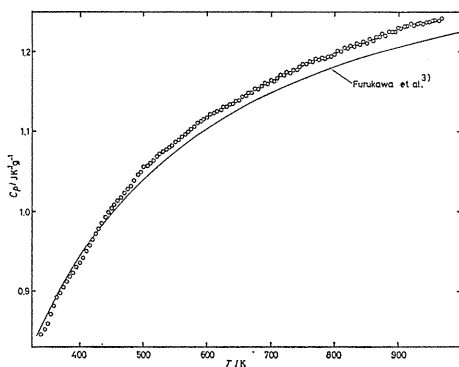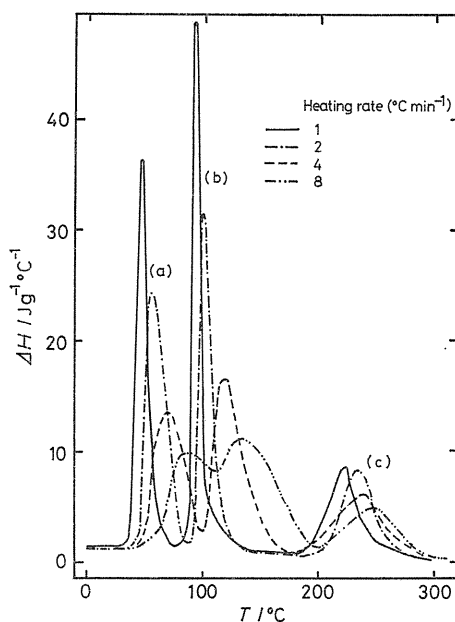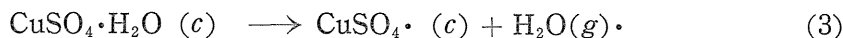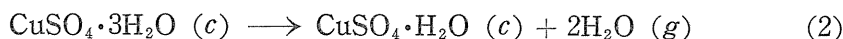

Fig. 3. Heat capacity of alumina.[2]

Fig. 4. Reaction heat of $CuSO_4 \cdot 5H_2O$ plotted against temperature at various heating rates.[2]

$$CuSO_4 \cdot 5H_2O \ (c) \ \longrightarrow \ CuSO \cdot 3H_2O \ (c) + 2H_2O \ (g) \tag{1}$$

$$CuSO_4 \cdot 3H_2O \ (c) \ \longrightarrow \ CuSO_4 \cdot H_2O \ (c) + 2H_2O \ (g) \tag{2}$$

$$CuSO_4 \cdot H_2O \ (c) \ \longrightarrow \ CuSO_4 \cdot \ (c) + H_2O(g) \cdot \tag{3}$$
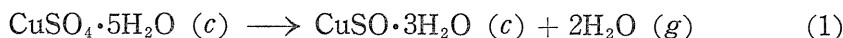
Peak (a) in Fig. 4 is caused by the reaction (1), peak (b) by reaction (2) and peak (c) by reaction (3). It is noted that the separation between peaks (a) and (b) at low heating rates, say 1 K min^{-1}, is very clear compared with the usual data obtained by differential thermal analysis.

2. 1. 2. Direct heating pulse calorimeter

As has been descried in the preceding section, heat leak increases rapidly as temperature rises and the absolute measurement of specific heat capacity above 1000 K becomes extremely difficult by means of adiabatic calorimetry. For the measurement at temperatures higher than 1000 K, a direct heating pulse calorimeter has been constructed for semiconducting materials[4]. In this calorimeter, the energy for heating the sample Q is supplied directly by electrical power source and a temperature rise of sample $\varDelta T$ is measured:

$$C_p = \frac{Q}{m \varDelta T}, \tag{4}$$

where C_p is the specific heat capacity and m is the mass of the sample. Since the temperature of the sample in this method rises rapidly and homogeneously, the time period for the measurement can be very short, giving the heat leakage small. For semiconducting samples, however, it is difficult to make the heating rate very rapid because of poor electrical conductivity, which would cause a larger error compared with highly conductive samples. In order to avoid this difficulty, the sample is surrounded by a molybdenum shield and both the sample and the shield are heated simultaneously and individually by electrical pulses from t_0 to t_1 so as to obtain the same temperature rises for the purpose of keeping an adiabatic condition, as shown in Fig. 5[4]. The changes of the sample temperature $\varDelta T$ and the shield temperature T_{sh} are shown schematically in Fig. 6[4]. In practice, during
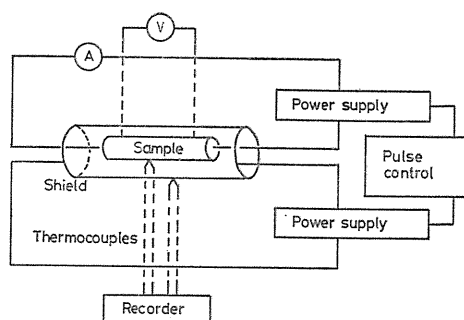

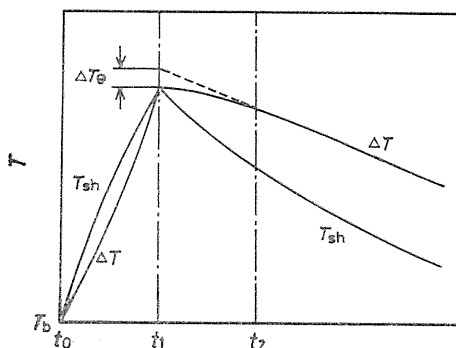Fig. 5. Block diagram of the direct heating pulse calorimeter with an adiabatic control.[4]

Fig. 6. Temperature changes of the sample $(\varDelta T)$ and shield (T_{sh}) during measurement.[4]

the pulse heating and for a short time afterwards, temperature measurement is not possible because of voltanic noise on the thermocouple, hence, the measurement of temperature is started at t_2 in Fig. 6 and only a decreasing curve is obtained. Then, ΔT can be obtained by extrapolation as shown by a broken line.
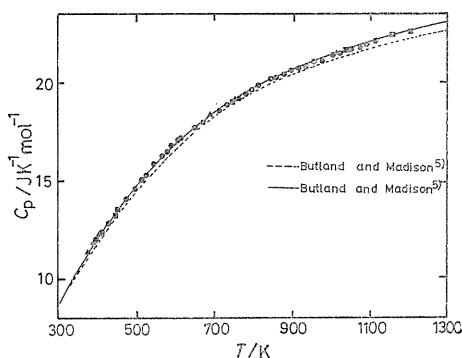

Fig. 7. Heat capacity of graphite.[4]   Fig. 8. Heat capacity of silicon carbide.[4]
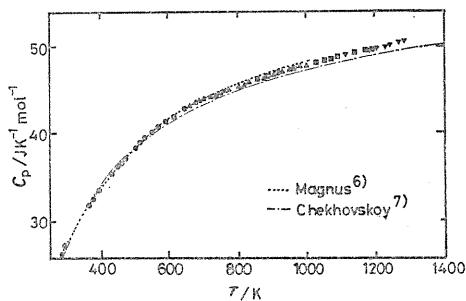
Two examples measured by this calorimeter are shown in Figs. 7 and 8[4]. Figure 7 shows the heat capacity of graphite which is commercially available of 99.9 % purity, 150 mm long, 3.85 mm in diameter and 27.52 % porosity. In this figure, the solid and broken lines indicate the data compiled by Butland and Madison[5] with a good agreement with our results. The imprecision of this calorimeter is within ±0.5 %. The electrical condutivity of the sample can also be obtained simultaneously within an imprecision of ±0.5%. Figure 8 shows the heat capacity of silicon carbide which is commercially available α-type silicon carbide of 99.99 % purity, 100 mm long, 9.9 mm in diameter and 25.88 % porosity. The results are obtained with an imprecision within 0.5 % as seen from the figure, where other authors data[6,7] obtained by the drop method are also shown.

2. 1. 3. Heat leakage in calorimetry at high temperatures

The error of calorimeter is mainly caused by the heat leakage between the sample and the surroundings, which usually cannot be measured directly. Since the most part of the heat exchange at high temperatures is due to radiation, the quantity of the heat exchange W is nearly proportional to the surface area of sample S, its emissivity ε and the average temperature difference between the sample surface and the surroundings ΔT_s:

$$W \propto \varepsilon S \Delta T_s. \tag{5}$$

If the time required for measurment of temperature rise is t_m and the heat leakage Q' during t_m is

$$Q' = \int_0^{t_m} W dt \propto \varepsilon S \int_0^{t_m} \Delta T_s dt$$

$$= \varepsilon S \overline{\Delta T_s} t_m, \tag{6}$$

where $\overline{\Delta T_s}$ is the average of ΔT_s during the time t_m.   Since the energy absorbed by sample is a product of heat capacity of sample C and the temperature rise ΔT, the relative error due to heat exchange δ is

$$\delta = \frac{Q'}{C \Delta T} \propto \frac{\varepsilon S \overline{\Delta T_s} t_m}{C \Delta T}. \tag{7}$$

In the case of adiabatic calorimeter, the value of C/S becomes rather large when the sample is contained in a vessel, but ε can be taken as a small value by selecting a proper metal as a vessel material.   Since heater, sample, sample vessel and thermometer are in the metal vessel enclosing the sample and thermal contact among them is not sufficient, relatively long time is required for thermal equilibrium, resulting in large t_m, while the ratio $\overline{\Delta T_s}/\Delta T$ can be kept to be small by a precise adiabatic control.   The error of adiabatic control is about ± 0.001 K at 1000 K in the best of calorimeter at present, but $\overline{\Delta T_s}$ may become larger than it, because there are temperature distributions on the sample surface.   Hence the value of $\overline{\Delta T_s}$ determines the limit of the precision of the adiabatic calorimeter.   In order to reduce temperature distribution in the sample surface, a double platinum sphere has been used and inert gas of reduced pressure has been introduced in the adiabatic scanning calorimeter.   In the intermittent heating method of the adiabatic calorimeter, the heat leakage can be corrected to some extent from the measurement of temperature drift in steady states before and after heating and the deviation of adiabatic control.   Grønvold[8] has used this method and obtained an imprecision of $\pm 0.3 \%$ up to 1050 K using a standard sample of alumina.   In the cases of flash calorimetry, direct heating pulse calorimetry and AC calorimetry, they intend to keep t_m to be small, although $\overline{\Delta T_s}/\Delta T$ becomes large.   In the direct heating calorimeter, the sample temperature rises instantaneously when the electric current is led to the sample and t_m is very small, and futhermore an adiabatic control by heating a shield simultaneously has been made in order to decrease $\overline{\Delta T_s}/\Delta T$ in our apparatus. In the flash calorimeter, the temperature of a surface of sample, on which a high-intensity light pulse is impinged, rises rapidly and gradually approaches to the thermal equilibrium. t_m is proportional to the square of thickness and inversely proportional to the thermal diffusivity of sample.   Using this type of calorimeter Takahashi et al.[9] have obtained an imprecision within 1% and an inaccuracy within 2% up to 1100 K.

2. 2. Measurement of heat of formation

A twin microcalorimeter of Tian-Calvet type is useful for measurements of heat of formation, partial molar enthalpy, heat of mixing or heat of solution and heat of gas adsorption on solids.   It measures the heat flux q, which flows to a heat reservoir at a constant temperature through a conductive medium, by measuring the temperature difference ΔT between the sample vessel and the heat reservoir:

$$q = C \frac{d(\Delta T)}{dt} + h \Delta T, \tag{8}$$

where C is heat capacity of the calorimeter and h is a general thermal conductivity coefficient.   After a long period of time, the quantity of heat Q emitted from or absorbed in the sample, can be obtained by integrating Eq. (8) to infinite time,

$$Q = C \left[\Delta T \right]_0^\infty + h \int_0^\infty \Delta T \, dt . \tag{9}$$
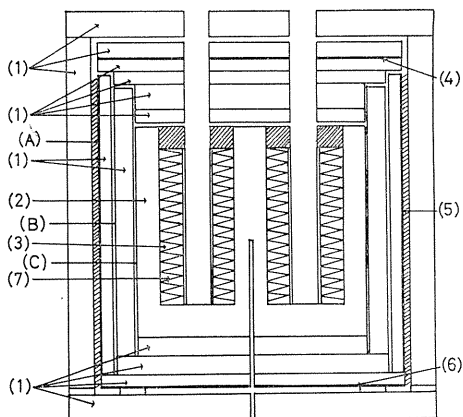
Fig. 9. Schematic drawing of the calorimeter.[10] (1) thermal insulator (2) alumina block (3) alumina powder (4) upper plane heater (5) main heater (6) lower plane heater (7) thermoelectric piles (Pt/Pt Rh 13% thermocouples) (A), (B), (C) show the positions of thermocouples for the measurement of temperature.

ΔT is regarded as zero before the heat absorption or emissin ($t=0$) and after a long period of heat event ($t\to\infty$). Therefore the first term of Eq. (9) is neglected and Q can be obtained solely by integrating ΔT, where the apparatus constant h in the second term of Eq. (9) can be determined from the calibration using a known heat event. The main part of the calorimeter is shown schematically in Fig. 9.[10] It consists of two calorimeter units located in two wells of an alumina block maintained at a constant temperature, of which diameter is 18 cm and height is 15 cm. The temperature difference between the calorimeter block and the surrounding block is measured by means of 120 junctions of Pt/Pt Rh 13% thermocouple of 0.3 mm in diameter. The two thermopiles of the two calorimeters are connected in series but in opposition to each other in order to detect the heat absorbed by or emitted from the sample in one side of the two calorimeters. The output of the thermopiles is supplied to an integrater and a recorder through a d. c. amplifier.

An ideal twin calorimeter should be perfectly symmetrical with respect to the two calorimeters; the sample and the reference sides. In practice, however, some deviations from perfect symmetry such as difference in thermal contacts of the thermocouples to the calorimeter block and the surrounding block and small deviation from the symmetry in size of the calorimeter block, the surrounding blocks, the wells of constant temperature block and the main heater, etc., cannot be avoided especially when ceramic materials are used for the purpose of high temperature operation. The presence of unsymmetry in the two calorimeters would result in a baseline fluctuation through the fluctuation of the temperature of the main heater and that of room temperature.

In order to know how the fluctuation of the temperature of the main heater affects the baseline, three Pt/Pt Rh 13% thermocouples were set in the places (A), (B) and (C) shown in Fig. 9. Temperature variation of four periods of a sine curve with amplitude of 12.5 K and period of 660 sec was applied in the main heater (the position (A) in Fig. 9) by adjusting current of the main heater
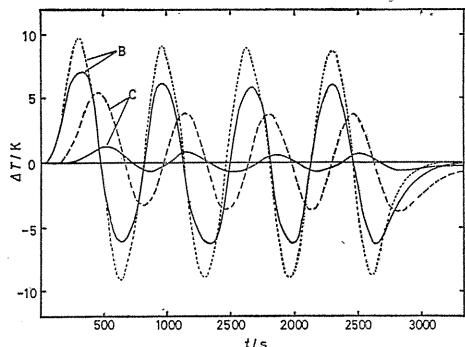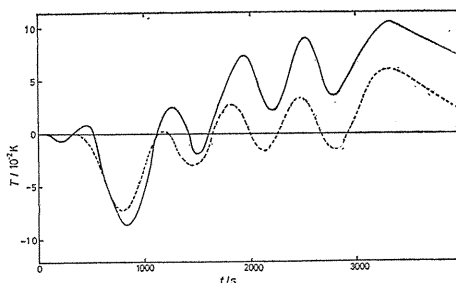
Fig. 10. Temperature variation of the calorimeter after giving temperature oscillation of four cycles of a sine curve with an amplitude of 12.5 K and a period of 660 sec at the main heater.[10] B and C represent the positions of 1 and 3 cm inside from the main heater, respectively.
—— observed one ; ------ calculated one.

Fig. 11. The temperature drift of the baseline of the calorimeter.[10]
—— observed curve ;
------ calculated curve.

manually, and the temperatures of the positions (B) and (C) and the baseline of the calorimeter were recorded as a function of time. The results are shown in Figs. 10 and 11 in solid lines[10]. As can be seen from the figures, the amplitude of the sine curve decreases and the delay of phase of sine curve increases as the position goes inside.

The temperature variation as functions of time and position can be compared with the computer calculation: If we assume that the heat leak in upper and lower directions can be neglected and the temperature can be determined solely by the position in the radial direction, we have the following diffusion equation:

$$\frac{\partial T(r, t)}{\partial t} = \kappa \left\{ \frac{\partial^2 T(r, t)}{\partial r^2} + \frac{1}{r} \frac{\partial T(r, t)}{\partial r} \right\}, \tag{10}$$

where $T(r,t)$ is the temperature as a function of the distance from the center r and time t, κ is the thermal diffusivity and $\kappa = \lambda/C_p\rho$, λ is the thermal conductivity, C_p the specific heat capacity and ρ the density. Eq. (10) is changed into a finite difference form for computer calculation. The results by the computer calculation are shown in broken lines in Fig. 10. Although the calculated values of the period of temperature oscillation are in good agreement with the observed ones, the calculated amplitudes are lower than the observed ones, which may be originated from the uncertainty of the parameters used in the calculation, or from the heat leak to upper and lower directions, neglected in the calculation. In order to simulate the baseline fluctuation due to some unsymmetry existing in the calorimeter, it is assumed that the calorimeter is displaced 0.25cm from the symmetrical position. The results of the calculation based on this assumption are shown

in Fig. 11[10]. The agreement between the observed and the calculated values is fairly good in spite of a simple assumption for the calculation.

The calibration of the calorimeter was made by two methods: One is the measurement of enthalpy difference of alumina with various mass between the temperature of the calorimeter, say 917 K, and room temperature by dropping it into the calorimeter. A typical thermogram of input energy 400 J is shown in Fig. 12. The other method was the chemical calibration; the two chemical reactions were used for calibration:
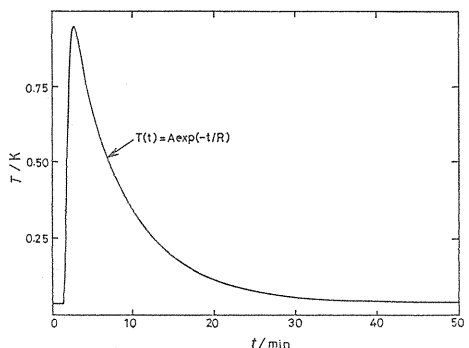
Fig. 12. A typical thermogram of input energy about 400 J.[10]

$$\frac{1}{2}Cu_2O + \frac{1}{4}O_2 = CuO, \qquad (11)$$

$$Nb + \frac{5}{4}O_2 = \frac{1}{2}Nb_2O_5. \qquad (12)$$

Niobium powder used was in 99.99 % purity with respect to the other metals. The reaction was started by introducing oxygen gas into an evacuated reaction tube at 920 K. The results obtained by the two methods are shown in Fig. 13. A fairly good agreement between the two chemical calibrations is observed. Small difference in the two methods is thought to be mainly due to the difference in the thermal conductance of the reaction tubes, because an open tube is used in the dropping method and an air tight tube with reduced gas pressure is used in the chemical calibration.

Fig. 13. Results of the calibration of the calorimeter.[10]
    ◉, drop method using enthalpy difference of alumina; ○, chemical calibration using the oxidation reaction of Cu_2O; △, chemical calibration using the oxidation reaction of niobium metal.
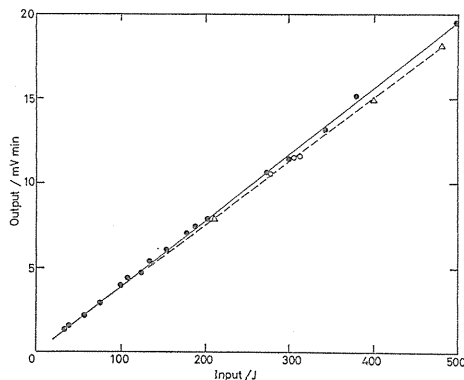
2. 3. *Measurement of thermal conductivity and thermal diffusivity*

Many methods have been adopted for measuring the thermal conductivity of solid materials, but few are applicable to the continuous measurement over a wide range of temperature with small size of sample. We have developed a method for simultaneous measurements of thermal conductivity and thermal diffusivity by heating a small sample at a constant heating rate, which we called a scanning temperature method[11]. When a cylindrical specimen is heated on its base plane without heat leakage in the radial direction, the differential equation for heat conduction through the sample is expressed as follows,

$$dT/dt = \kappa(d^2T/dx^2),\tag{13}$$

where T is the temperature, t the time, x the axial distance from the base plane, and κ the thermal diffusivity. If we assume that the heating rate β and the heat flow Q per unit time through a cross section are constant, the boundary conditions are given by

$$t>0,\ x=0:\quad dT/dt=\beta,\tag{14}$$

$$t>0,\ x=l:\quad -S\lambda(dT/dx)=Q,\tag{15}$$

where S is the cross section of the specimen, l its length, and λ is the thermal conductivity. By solving Eq. (13) using these boundary conditions, the temperature difference between the base and top surfaces is obtained under quasi-steady state:

$$\Delta T = (l^2\beta/2\kappa) + (Ql/\lambda S).\tag{16}$$

When a conducting block is placed on the top of the specimen, it serves as heat sink; heat flows through the specimen and passes into the sink from the top surface. Then Eq. (16) becomes

$$\Delta T = (l^2/2\kappa + C_M M_M l/\lambda S)\beta = (A + C_M M_M B)\beta,\tag{17}$$

where A represents $l^2/2\kappa$, B is $l/\lambda S$, and C_M, M_M are the specific heat capacity and the massof metal block. When $\Delta T/\beta$ is plotted against $C_M M_M$, A is obtained by extrapolation of $C_M M_M$ to zero and B from the slope of the line. The thermal conductivity λ and the thermal diffusivity κ of the specimen are then obtained simultaneously from B and A, by measuring the temperature difference ΔT at a constant heating rate β for various heat capacities of heat sink $C_M M_M$.

The apparatus is shown schematically in Fig. 14. The specimen is sandwiched between silver blocks of 12 mm in diameter. As a heating element for the specimen, a nickel-chromium sheathed heater of 1 mm in diameter is sandwiched between a ceramic disk and a silver disk. A thin hemispherical silver dome serves as an adiabatic thermal shield, which is heated by an external heater. Chromel-alumel sheathed thermocouples are placed at the points marked 1, 2 and 3 in Fig. 14. The thermocouples at the points 1 and 2 are inserted into holes of 1 mm in diameter drilled on the silver blocks, and fixed with silver paste. The heating rate β is set by an electronic programmer, and the difference between the voltage from the programmer and the electromotive force from the thermocouple at the point 1 is brought to zero by controlling the power of the internal heater, using a PID
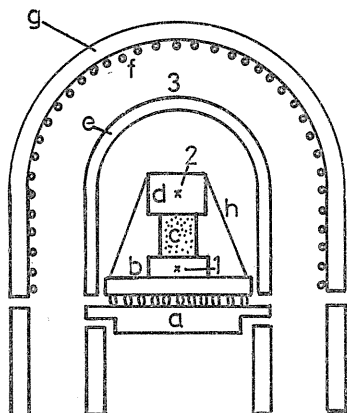
Fig. 14. Apparatus for the thermal conduct
ivity and thermal diffusivity me-
asurements called a scanning tem-
perature method.[11)
a: heating element
b: lower silver block
c: specimen
d: upper silver block
e: silver adiabatic shield
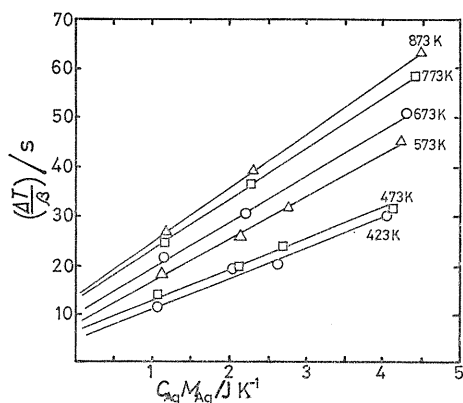f: external heater
g: furnace
h: molybdenum wire

Fig. 15. $\Delta T/\beta$ vs. heat capacity of silver
block.[11)

thyristor-type controller. The temperature difference ΔT, between the top and
the base surfaces of alumina single crystal sample is measured at various heating
rates using various heat capacities of silver block. The results are shown in Fig.
15, where $\Delta T/\beta$ at various temperatures is plotted against heat capacity of silver
block. From the results shown in Fig. 15, thermal conductivity of single crystal
alumina is obtained, which is in good agreement with the reference data[12).

2. 4. Measurement of vapor pressure

The vapor pressure at high temperatures is measured by means of a combina-
tion of mass-effusion (weight loss measurements) and mass-spectrometry.

The apparatus for the mass effusion is shown schematically in Fig. 16. The
total weight loss is measured to determine the total vapor pressures as a function
of time, and the sample is contained in a tungsten Knudsen-cell in a graphite
holder. The sample in a tungsten Knudsen-cell surrounded by tantalum radiation
shields is heated by an induction coil.

Mass-spectrometric measurements are carried out to identify the vapor species
and to measure the partial vapor pressures using a time-of-flight mass-spectrometer
(CVC model MA-2) equipped with a tungsten Knudsen-cell in a tungsten holder
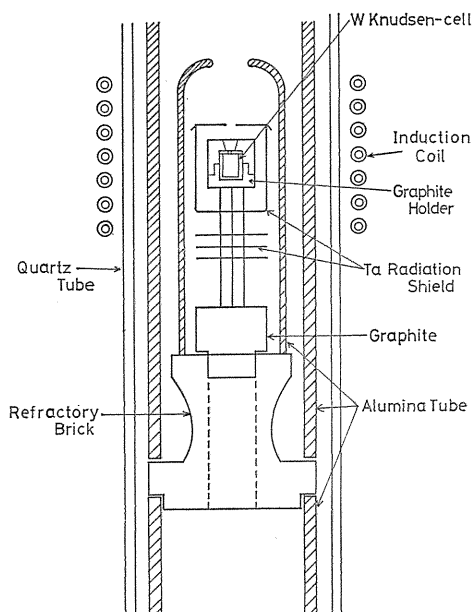
Fig. 16. Schematic drawing of the apparatus for the mass-effusion measurements.
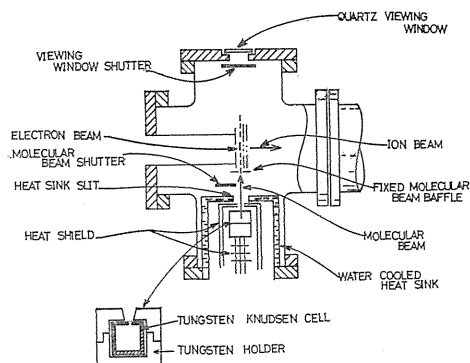

Fig. 17. Schematic drawing of the apparatus for the mass-spectrometry.

heated by electron bombardment.   The system for the time-of-flight analysis is shown schematically in Fig. 17.   The Knudsen-cell consists of a tungsten crucible and a tungsten plate lid.   The tungsten crucible is approximately 10 mm long and 10 mm outer diameter with 1.5 mm wall thickness.   The tungsten lid is about 0.18 mm thick and provides an orifice of about 0.5 mm in diameter at the center.   The assembly of the crucible and the lid is tightly contacted with a tungsten holder surrounding the assembly.   The intensity of each vapor species originating from the Knudsen-cell is determined from the difference in the ion currents with the molecular beam shutter open and closed.   The electron energy to ionize vapor species is selected to be slightly higher ($\sim$2-3 eV) than the observed ionization potential of vapor species.   The absolute pressures are calculated by comparing the intensities of the ionic current of the vapor species with those of silver metal used as the internal standard.   The isotopic abundance ratio and the vapor pressure of silver are taken from the literature[13,14].   Atomic ionization cross-sections are taken from the tabulation by Mann[15] and the additivity principle suggested by Otvos and Stevenson[16] is used to calculate the molecular cross-sections of molecular species such as NbO and NbO_2.   The relative multiplier gain is calculated by assuming that it is to be inversely proportional to the square root of the mass[17,18]. Temperature measurements are made with a Leeds and Northrup disappearing-filament optical pyrometer, of which error is determined to be $\pm$5K by comparing with the melting point of platinum metal and the EMF of Pt–Pt 13 % Rh thermo-couple.   Observation is made through an orifice of the Knudsen-cell.

III. Heat capacity and thermal conductivity of uranium oxides

Uranium dioxide, $UO_{2\pm x}$ has been used as a nuclear fuel for the nuclear reactor and its thermophysical properties such as heat capacity and thermal conductivity are very important for the design and operation of the nuclear reactor. The thermophysical properties of higher oxidation compounds, $U_4O_{9\pm y}$ and U_3O_{8-z} are also important not only because of the comparison with $UO_{2\pm x}$ but also because of their characteristic properties in the relatively wide ranges of nonstoichiometry originated from the different valence states of uranium. A phase diagram of uranium oxides is shown in Fig. 18[19]. A considerable number of studies on the phase relations and thermal properties in the uranium-oxygen system have been carried out owing to the importance of $UO_{2\pm x}$ as a nuclear fuel. Heat capacity and thermal conductivity on uranium higher oxides U_4O_{9-y} and U_3O_{8-z} have been measured extensively in our laboratory in relation to the phase transitions, which will be described below briefly.
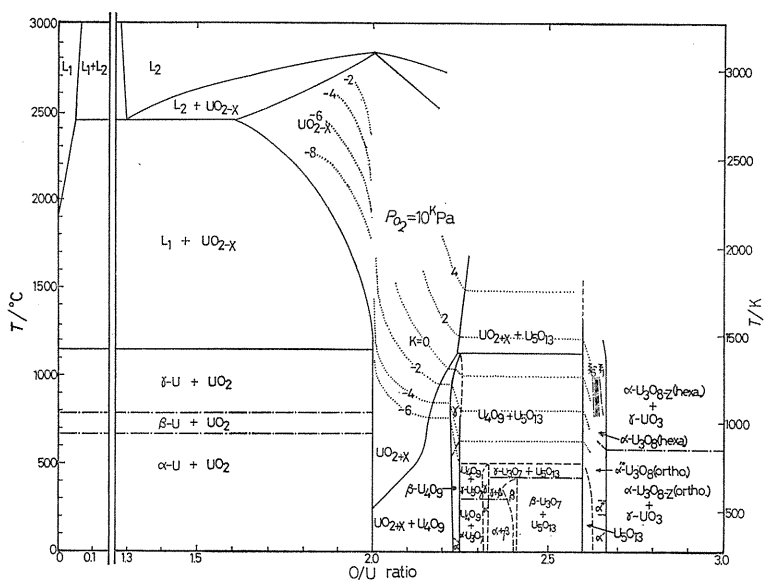
Fig. 18. Phase diagram of uranium oxides.[19]

3. 1. U_4O_{9-y} and doped-U_4O_{9-y}

3. 1. 1. Low temperature phase transition

A λ-type anomaly in heat capacity of U_4O_9 was first observed by Gotoo and Naito[20], and independently by Westrum et al.[21], at slightly above room temperature. The mechanism of this phase transition has been an object of the study carried out in our laboratory for many years, and it is concluded that the transition is originated from an order-disorder rearrangement of U^{4+} and U^{5+} ions and succeeding displacement of oxygen ions[22]. The measurement of heat capacities of U_4O_{9-y} with different O/U ratio is very useful to discuss the mechanism of the phase

transition[23].

Heat capacities of U_4O_{9-y} with O/U ratio 2.228, 2.240 and 2.250 were measu red[24] by means of the adiabatic scanning calorimeter and the results are shown

Fig. 19. Heat capacities of U_4O_{9-y}.[24]

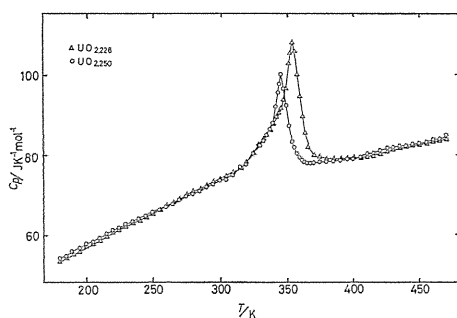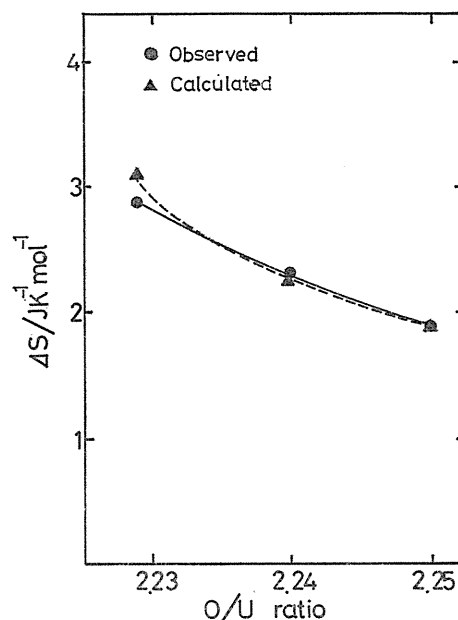Fig. 20. Observed and calculated entropy change against O/U ratio of U_4O_{9-y}.[27]

Table 1. The compositions and entroy change of U_4O_{9-y} between the low- and high-temperature phases[27].

	Ratio of X-ray superlattice lines	Composition of low-temperature phase	Composition of high-temperature phase
$UO_{2.228}$	2.0	$UO_{2-0.094}O'_{0162}O''_{0.162}$	$UO_{2-0.228}O'_{0.228}O''_{0.228}$
$UO_{2.240}$	1.55	$UO_{2-0.146}O'_{0.193}O''_{0.193}$	$UO_{2-0.240}O'_{0.240}O''_{0.240}$
$UO_{2.250}$	1.0	$UO_{2-0.250}O'_{0.250}O''_{0.250}$	$UO_{2-0.250}O'_{0.250}O''_{0.250}$

	calculated					observed
	ΔS_n	ΔS_i	ΔS_d	ΔS_e	$\Delta S_d + \Delta S_e$	ΔS
	$JK^{-1}mol^{-1}$	$JK^{-1}mol^{-1}$	$JK^{-1}mol^{-1}$	$JK^{-1}mol^{-1}$	$JK^{-1}mol^{-1}$	$JK^{-1}mol^{-1}$
$UO_{2.228}$	2.80	−0.9	2.01	1.17	3.18	2.93
$UO_{2.240}$	1.76	−0.75	1.01	1.30	2.31	2.34
$UO_{2.250}$	0	0	0	1.92	1.92	1.92

in Fig. 19, where significant differences in the transition temperature and the enthalpy change are seen between the two samples with slightly different O/U ratios. From heat capacity data, the entropy change due to the phase transition can be obtained, which is shown in Fig. 20 and the last column of Table 1. The entropy change due to the transition ΔS is expressed to be the sum of that due to the displacement of oxygen atoms, ΔS_d, and that due to the order-disorder rearrangement of U^{4+} and U^{5+} ions, ΔS_e[24] :

$$\Delta S = \Delta S_d + \Delta S_e. \tag{18}$$

The entropy change due to the displacement of oxygen atoms can be calculated using the data of the intensities of X-ray superlattice lines[25] before and after the phase transition as follows[24]. Taking the model proposed by Willis[26] as the crystal structure of U_4O_{9-y}, the formula for U_4O_{9-y} are written as $UO_{2-a}O'_bO''_c$, where a corresponds to the number of vacant oxygen lattice sites in the fluorite lattice, b the number of O' site located at a distance of 0.85 Å along the $\langle 110 \rangle$ direction from the center of the large interstice and c the number of the O'' site located at a distance of 1.05 Å along the $\langle 111 \rangle$ direction. The compositions of the high- and low-temperature phases are calculated for different O/U ratios using the data of the X-ray superlattice lines before and after the phase trasition, and are given in Table 1, where the occupation numbers b and c are assumed to be equal for the sake of simplification. The entropy change due to the displacement of oxygen ions consists of two terms : (i) the term due to the displacement of oxygen ions in the normal fluorite sites, ΔS_n, and (ii) the term due to the displacement of oxygen ions in the interstitial sites, ΔS_i. In the case of $UO_{2.240}$, for example, ΔS_n and ΔS_i are calculated as follows.

$$\Delta S_n = k(ln_{2N}C_{1.76N} - ln_{2N}C_{1.854N}) = 1.76 \text{JK}^{-1}\text{mol}^{-1}. \tag{19}$$

$$\Delta S_i = k(ln_{0.25N}C_{0.24N} - ln_{0.25N}C_{0.193N}) = -0.75 \text{JK}^{-1}\text{mol}^{-1}. \tag{20}$$

Hence, the total entropy change due to the displacement of oxygen ions, ΔS_d, for $UO_{2.240}$ is $\Delta S_d = \Delta S_n + \Delta S_i = 1.01$ JK^{-1}mol^{-1}. The results are also given in Table 1. The entropy change due to the order-disorder rearrangement of U^{4+} and U^{5+} ions, ΔS_e, is calculated from the jump width, J, in the Z–type jump of the electrical conductivity shown in Fig. 21[27]. Assuming a hopping model, ΔS_e is obtained as[27]

$$\Delta S_e \propto log\, \nu_h/\nu_e = J, \tag{21}$$

where ν_h and ν_e are hopping frequencies at high and low temperatures, respectively. The relative jump widths for $UO_{2.250}$, $UO_{2.240}$ and $UO_{2.228}$ are obtained as 1.0, 0.68 and 0.60, respectively, where the jump width for $UO_{2.250}$ is taken as unity. Since it is known from the X-ray diffraction study[25] on superlattice lines of U_4O_{9-y} that the entropy change due to the displacement of oxygen ions, ΔS_d, is zero for $UO_{2.250}$, the entropy change 1.92 JK^{-1}mol^{-1} observed for $UO_{2.250}$ is thought to represent the entropy change due to the order-disorder rearrangement of U^{4+} and U^{5+} ions. Therefore, ΔS_e for substoichiometric samples can be calculated from the jump width as shown in the eighth column in Table 1. The total entropy change $(\Delta S_e + \Delta S_d)$ thus calculated and the entropy change observed are compared in Table 1 and Fig. 20, where a good agreement between the calculated and observed
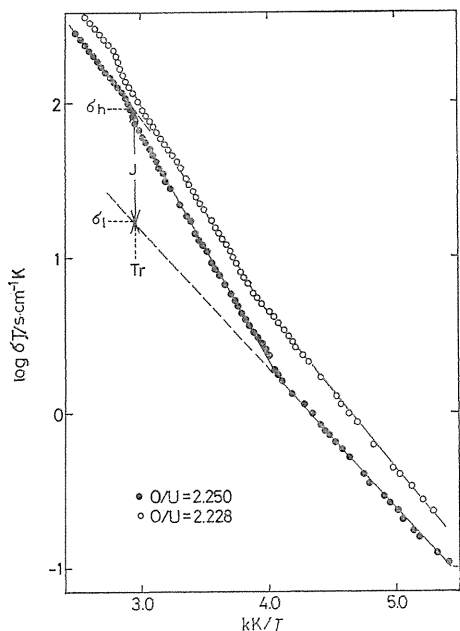
Fig. 21. Z-type jump-of electrical conduc-
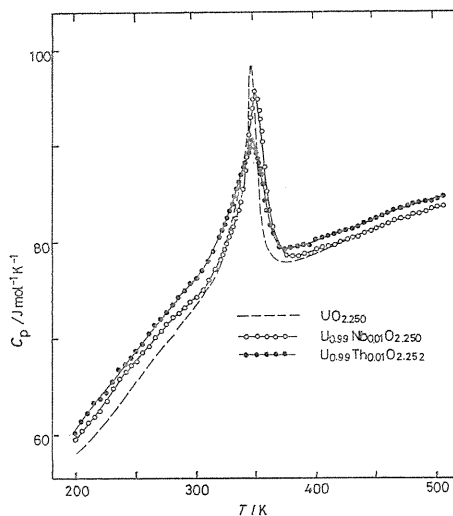tivity for $UO_{2.228}$ and $UO_{2.250}$.[27]

Fig. 22. Heat capacities of doped and un-
doped U_4O_{9-y}.[28]

values is seen[27].

Heat capacity of U_4O_{9-y} doped with Th and Nb has also been measured and
the results for $U_{0.99}Th_{0.01}O_{2.252}$ and $U_{0.99}Nb_{0.01}O_{2.250}$ are shown in Fig. 22[28],
where the data for $UO_{2.250}$ are also shown for comparison. It is seen from the
figure that a λ-type peak in the heat capacity curve becomes broader by doping,
and this tendency is more prominent in the sample doped by thorium than by
niobium. In the case of $U_{0.99}Th_{0.01}O_{2.252}$, for example, uranium ions in the lattice
may be replaced by thorium ions. The valence of thorium ion is 4, while the
average valence of the surrounding cation lattice is about 4.5, then the anions and
cations adjacent to the Th^{4+} ion must rearrange to maintain the charge balance;
the valence of the uranium cations neighbouring Th^{4+} ions would be likely to be
5+, while that at a distance from a Th^{4+} ion would be likely to be 4+. With U^{4+}
and U^{5+} ions distributed in this way, the thermal energy required to cause the
phase transition namely disordering of the ordered arrangement of U^{4+} and U^{5+}
ions with corresponding rearrangement of oxygen ions is different at different
locations within the crystal. Accordingly, the transition temperature also varies
with position in the crystal so that the peak in the heat capacity curve becomes
broader. This effect is more prominent in the sample doped with thorium than
with niobium presumably because niobium can exhibit a valence of 4+ besides 5+,
as indicated by the existence of the compound NbO_2 as well as Nb_2O_5. The entropy
change of the transition for both doped and undoped U_4O_{9-y} is plotted in Fig. 23[28]
against the average valence of the uranium. The valances of thorium and niobium
are taken as 4+ and 5+, respectively. The entropy change is seen to vary linearly
with the average valence of the uranium for both doped and undoped samples,
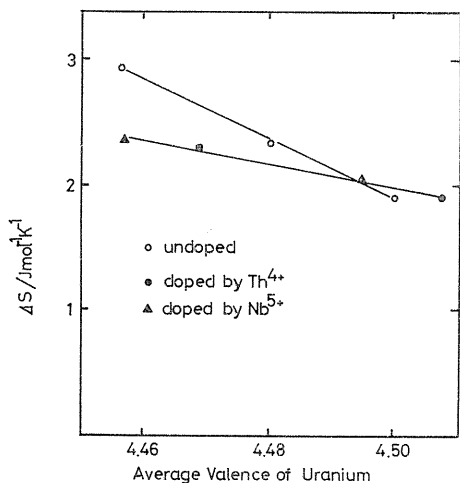
Fig. 23. The entropy change of the transition for doped and undoped U_4O_{9-y} plotted against the average valence of the uranium.[28]
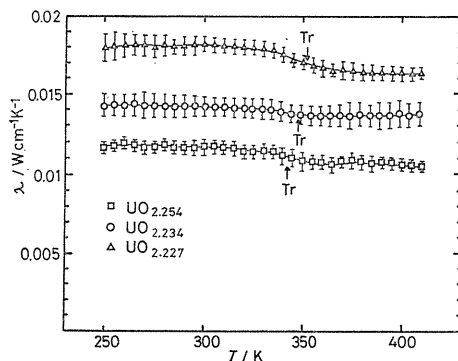
Fig. 24. Thermal conductivity of U_4O_{9-y}.[29]

suggesting that the order-disorder rearrangement of U^{4+} and U^{5+} would be a main factor of this phase transition.

The thermal conductivity of U_4O_{9-y} with various O/U ratios (2.227, 2.234, 2.254) has been measured by means of the scanning temperature method[29]. The results are shown in Fig. 24, where the transition temperatures obtained by the heat capacity measurement[24] are marked by arrows. The thermal conductivity of U_4O_{9-y} is much smaller than that of UO_2 probably due to the increase of the scattering of phonons by the interstitial oxygen atoms in U_4O_{9-y}. If the electronic contribution to thermal conductivity is neglected in U_4O_{9-y}, the thermal conductivity is expressed as

$$\lambda = \frac{1}{3} C_V u_L l_L, \tag{22}$$

where C_V is the heat capacity per unit volume at constant volume, u_L the average velocity of phonons and l_L the phonon mean free path. From Eq. (22), the phonon mean free path is calculated for each O/U composition and plotted against $1/T$ as shown in Fig. 25.[29] It is observed from the figure that the phonon mean free path in U_4O_{9-y} is very small, and is comparable with the nearest neighbor spacing of atoms in the U_4O_{9-y} lattice. The mean free path decreases as the O/U ratio increases. It is also noted that a small change in the slope is observed in the transition range in Fig. 25. Considering the facts that the nearest neighbour distances U–U and O–O in the stoichiometric U_4O_9 are about 3.8 and anout 2 Å, respectively, and th average O–O spacing becomes larger as the O/U ratio decreases, it is suggested that the mean free path of phonons in U_4O_{9-y} phase is determined mainly by the nearest neighbour O–O distance. The change in the phonon mean free path in the transition range shown in Fig. 25 is considered to be due to the change in scattering of phonons caused by the order-disorder rearrangement of U^{4+} and

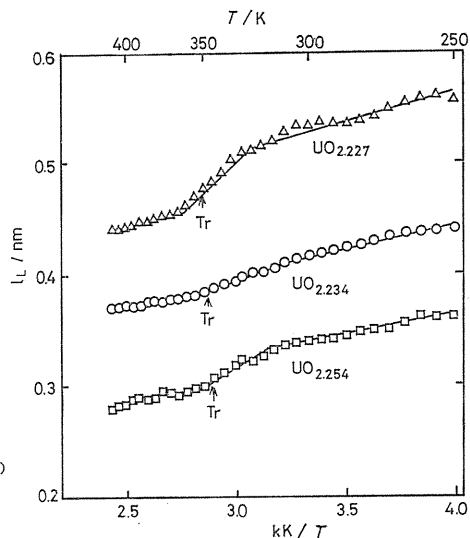U^{5+} ions and the subsequent displacement of oxygen atoms.

Fig. 25. Phonon mean free path of U$_4$O$_{9-y}$.[29]

3. 1. 2. High temperature phase transition

Heat capacity and electrical conductivity of U$_4$O$_{9-y}$ with various ratios in a high temperature region have been measured by the direct heating pulse calorimeter. The results of heat capacity measurement are shown in Fig. 26[30]. The second and the third peaks in the heat capacity curve as well as the first peak around 350 K discussed in the preceding section are observed around 1000 and 1100 K, respectively. These two peaks are considered to be due to the $\beta-\gamma$ transition related to the order-disorder rearrangement of U^{4+} and U^{5+} ions[31]. The excess heat capacity ΔC_p due to phase transition for stoichiometric U$_4$O$_9$ is obtained by adopting the following relation[23]:

$$\Delta C_p = \frac{1}{4} C_p(\mathrm{U}_4\mathrm{O}_9) - \frac{13}{12} C_p(\mathrm{UO}_2). \tag{23}$$

with the reference data[32] of $C_p(\mathrm{UO}_2)$, ΔC_p is obtained as shown in Fig. 27, where the results obtained by adiabatic calorimetry by Grønvold et al.[32] and those by
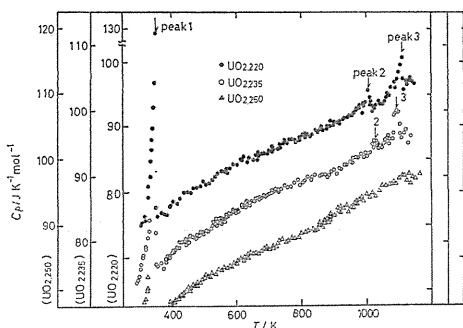

Fig. 26. Heat capacity of U$_4$O$_{9-y}$[30] The ordinate scale for each sample is displaced by 7.5 JK^{-1}mol^{-1}.

drop calorimetry by MacLeod[33] are also shown. ΔC_p shows up around 800 K and increases as temperature increases.

The excess heat capacity ΔC_p consists of two contributions. One is the contribution increasing monotonically with temperature, which is considered to be caused by the onset of the γ-U_4O_9-UO_{2+x} transition. As seen from the broken line in Fig. 27, the results by MacLeod[33] show that ΔC_p increases linearly up to 1400 K where the γ-U_4O_9-UO_{2+x} first-order transition occurs. Thus ΔC_p due to the onset of the γ-U_4O_9-UO_{2+x} transition can be extrapolated linearly up to 1400 K as an approximation, as shown by the solid line in Fig. 27. In the onset of the γ-U_4O_9-UO_{2+x} transition, the disordering of clusters of oxygen atoms may take place with increasing temperature, and the long-range ordering of the clusters disappears at 1400 K to give the UO_{2+x} phase. It is noted that ΔC_p does not become zero above 1400 K as it is seen in Fig. 27, indicating that the short-range ordering of the clusters of oxygen atoms still exists and contributes to the excess heat capacity. The other contribution to ΔC_p is an anomalous term in addition to the linear term, as it is seen in Fig. 26. This anomalous term is considered to be due to the β-γ transition.
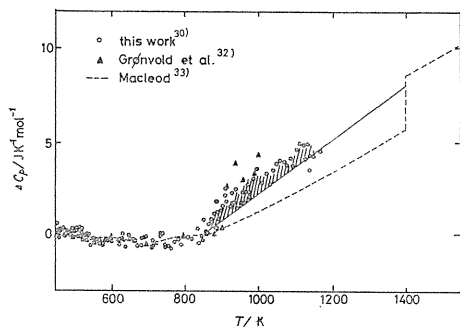

Fig. 27. Excess heat capacity of stoichiometric U_4O_9[30]

The excess entropy ΔS_2 for U_4O_9 sample due to the $\beta-\gamma$ transition is calculated from the shaded region shown in Fig. 27, and the excess entropy ΔS_0 for stoichiometric U_4O_9 due to the onset of the γ-U_4O_9-UO_{2+x} transition is also calculated from the linear extrapolation up to 1400 K as shown in Fig. 27. The total entropy change ΔS_{total} due to the phase transition from α-U_4O_9 to UO_{2+x} is obtained as shown in Table 2 where those for α-β and γ-U_4O_9-UO_{2+x} transitions are taken from the results by the authors[24] and by MacLeod[33], respectively.

The entropy change for $UO_{2.250}$ due to the order-disorder rearrangement of

Table 2. Entropy change due to three phase transitions of stoichiometric $UO_{2.250}$[30].

	α-β	β-γ	γ-U_4O_9-UO_{2+x}		Total	Calculated	
ΔS	ΔS_1	ΔS_2	ΔS_0	ΔS_t*	ΔS_{total}	ΔS_e	ΔS_d
JK^{-1}mol^{-1}	1.93±0.04	0.28±0.20	2.07±0.37	1.67	5.95	5.76 ($=R\ln2$)	2.88 ($=\frac{1}{4}R\ln4$)

* Due to the latent heat of first-order transition, from ref. 33).

U^{4+} and U^{5+} ions, ΔS_e, is evaluated to be $R\ ln\ 2$ (5.76 JK^{-1}mol^{-1}). This calculated value seems to be in good agreement with the experimental value ΔS_{total} (5.95 JK^{-1}mol^{-1}), but this may not be correct with the following two reasons: ΔS_e may be less than $R\ ln\ 2$ because of the presence of the residual entropy at 0 K, as the case of Fe_3O_4. In fact, using the jump width of the electrical conductivity and the relation given in Eq. (21), ΔS_e from α-U_4O_9 to UO_{2+x} is calculated as 3.78 JK^{-1}mol^{-1}: about two thirds of the value $R\ ln\ 2$. Although ΔS_d from α-U_4O_9 to UO_{2+x} is evaluated to be $1/4\ R\ ln\ 4 \simeq 2.88$ J, the existence of residual entropy at 0 K due to disordering of the clusters of oxygen atoms and the short range ordering of the clusters of oxygen atoms at high temperatures would give a value less than the evaluated value of ΔS_d. Hence, the difference between the calculated $\Delta S_d + \Delta S_e$ ((2.88+3.78) JK^{-1}mol^{-1}) and the observed ΔS_{total} (5.95 JK^{-1}mol^{-1}) may be ascribed to these causes.

3. 2. U_3O_{8-z}

The occurrende of phase transitions of U_3O_8 have been reported at different temperatures mainly by X-ray diffraction, but only one λ-type heat capacity anomaly has been known at 482.7 K by Girdhar and Westrum[34]. Discrepancy in the different temperatures of the phase transition reported previously is thought to be due to the differencies in O/U ratio and the thermal history of sample used as well as the difference in the methods of measurement. We have measured heat
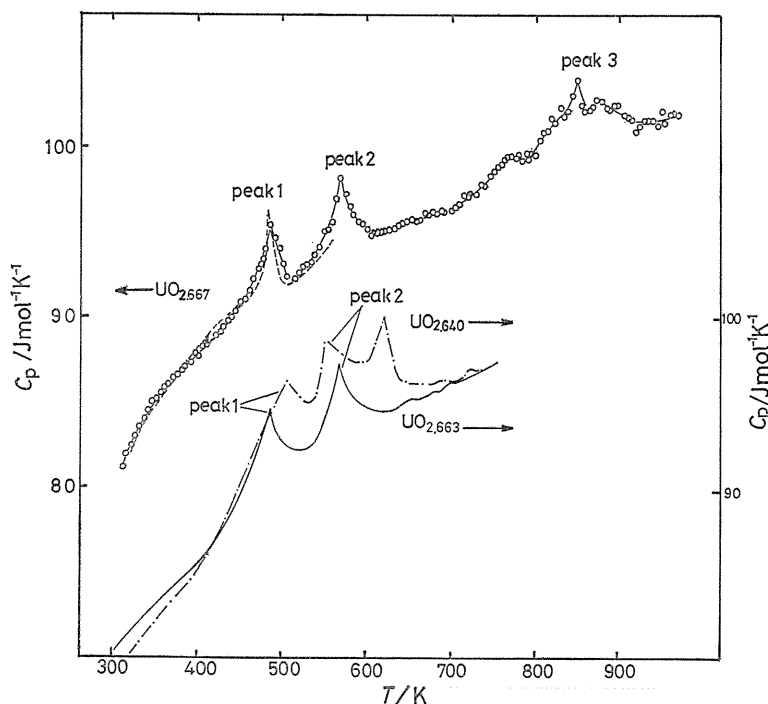
Fig. 28. Heat capacity of $UO_{2.667}$, $UO_{2.663}$ and $UO_{2.640}$.[35,36] The ordinate in the left side is for $UO_{2.667}$ and that in the right side is for $UO_{2.663}$ and $UO_{2.640}$.

capacities of U_3O_{8-z} with various O/U ratios, using the samples well annealed at 1273 K and cooled to room temperature over a period of 300 h by means of adiabatic scanning calorimetry and the results for $UO_{2.667}$, $UO_{2.663}$ and $UO_{2.640}$ are shown in Fig. 28[35,36]. For the stoichiometric sample $(UO_{2.667})$[35], the two additional heat capacity anomalies are seen at 568 and 850 K as well as the known anomaly at 483 K. For the substoichiometric samples, $UO_{2.663}$, $UO_{2.656}$ and $UO_{2.640}$[36], the heat capacity anomalies of $UO_{2.663}$ and $UO_{2.656}$ are similar to the stoichiometric sample, but an additional heat capacity anomaly is seen at 618 K for $UO_{2.640}$ in Fig. 28. The transition temperatures due to the first and second peaks become higher as O/U ratio increases. The entropy changes due to the first and second peaks are plotted as a function of O/U ratio in Fig. 29. The transition temperatures and entropy changes increase with decreasing O/U ration as in the case of $\alpha-\beta$ transition of U_4O_{9-y}. The phase transitions of U_3O_{8-z} possess such behaviors similar to those of U_4O_{9-y} that these transitions are assumed to be due to the order-disorder rearrangement of U^{5+} and U^{6+} ions.

The structure of U_3O_8 has been reported[37] to be orthorhombic and the two kinds of uranium atoms are surrounded by six oxygen atoms in close contact at distances between 2.07 and 2.23 Å, with a seventh oxygen atom at 2.44 Å for the U(1) atom and at 2.71 Å for the U(2) atom, and the U(1) and U(2) atoms are suggested to correspond to U^{6+} and U^{5+} ions, respectively. At
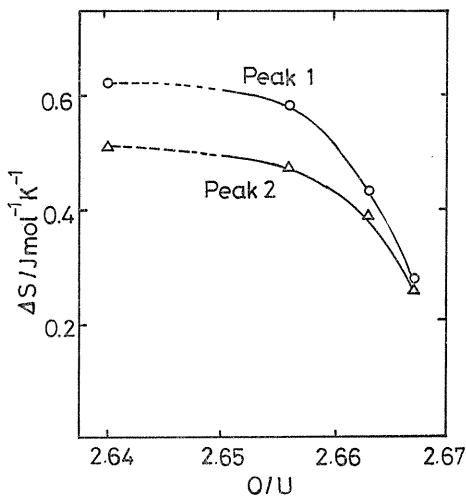

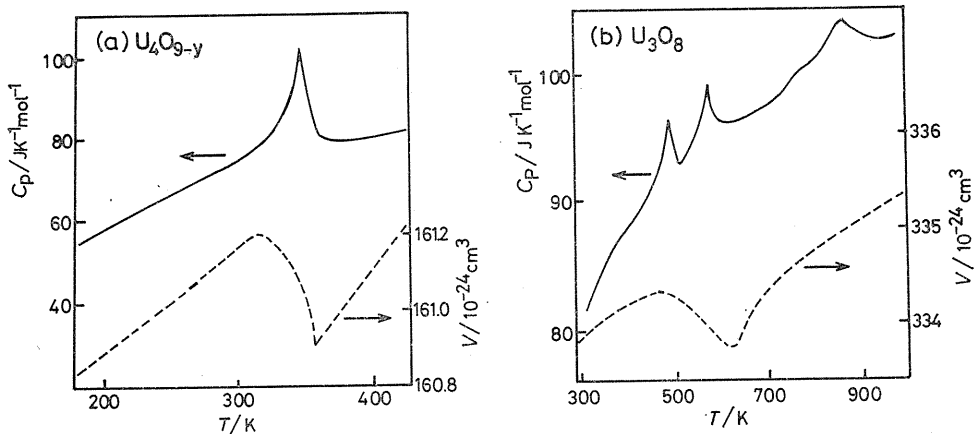Fig. 29. Entropy change for transitions of U_3O_{8-z} as a function of O/U ratio.[36]

Fig. 30. Thermal expansion and contraction behavior of the cell volume and heat capacity of U_3O_8 in comparison with U_4O_{9-y}.[36]

631 K, the structure becomes almost hexagonal[37] and the two kinds of uranium atoms, U(1) and U(2), can hardly be distinguished any longer by occupying single threefold position. The thermal expansion of U_3O_8 has been measured by high temperature X-ray diffraction[38], and the cell volume of U_3O_8 has a maximum around 483 K and a minimum around 623 K, as shown in Fig. 30, where the thermal expansion and contraction behaviors of U_4O_9 lattice are also shown together with the heat capacity data. It is seen from the figure that the expansion and contraction curves are quite similar between the two samples and the maximum and the minimum points of the cell volume correspond to the temperatures at which the λ-type heat capacity anomaly rises and ends off, respectively, for both samples. The only difference between the two samples is that there are two heat capacity anomalies between the temperatures of the maximum and the minimum cell volumes in U_3O_8, while only one anomaly occurs in U_4O_{9-y}. This would probably indicate that the second peak is due to some subsequent process of the phase transition corresponding to the first peak in U_3O_8. Accordingly, from the analogy with U_4O_{9-y}, the lattice expansion and contraction behaviors can be understood as the result of an order-disorder process of U^{5+} and U^{6+}.

The thermal conductivity of U_3O_{8-z} has been measured[39] by means of the scanning temperature method and the reciprocal mean free path of phonons in U_3O_{8-z} is obtained as a function of temperature as shown in Fig. 31. A break in the line of the reciprocal mean free path of phonons in U_3O_8 is seen around 470 K, but no detectable change is observed around the temperature corresponding to the heat capacity anomaly, peak 2, as seen in the figure. This would show that the subsequent process of the phase transition corresponding to peak 2 results only in little change in the mean free path of phonons.
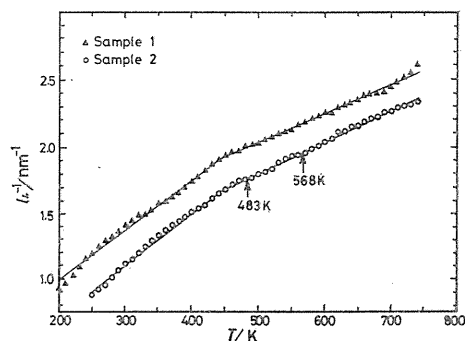

Fig. 31. The reciprocal phonon mean free
path $1/l_L$ for U_3O_8.[39]

3. 3. Heat capacity and thermal conductivity of uranium oxides

The heat capacity and thermal conductivity of uranium oxides, especially those of UO_2 have been measured by many investigators at high temperatures, since these are of great importance as basic properties of nuclear fuel at high temperatures. A brief review on the heat capacity and thermal conductivity of uranium oxides is to be given in the following section.

3. 3. 1. Heat capacity of uranium oxides at high temperatures

The heat capacity data of UO_2 at high temperatures so far reported are shown
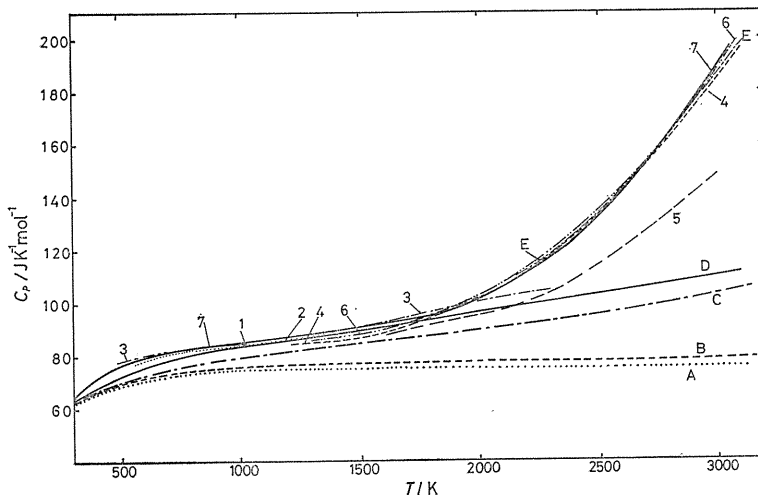
Fig. 32. Heat capacity of UO₂ at high temperatures measured by various authors.
1, Grϕnvold et al.[32];   2, Fredrickson and Chasanov[41];
3, Ogard and Leary[44];   4, Hein et al.[42,43];
5, Affortit and Marcon[45];   6, Szwarc[46]
7, Kerrisk and Clifton[40];   A, B, C, D, E show the resolved heat capacities
evaluated by Browning[50]. A: C_h; B: C_h+C_{ah}; C: $C_h+C_{ah}+C_d$;
D: $C_h+C_{ah}+C_d+C_{sh}$; E: $C_h+C_{ah}+C_d+C_{sh}+C_{eh}$.

in Fig. 32. Grϕnvold et al.[32] measured the heat capacity of UO₂ up to 1000 K means of adiabatic calorimetry and resolved the heat capacity into three terms: a lattice vibrational, a dilational and an electronic excitation (Schottky) terms. The electronic excited levels were obtained to be 900, 1600 and 2900 cm⁻¹. The heat capacity data above 1000 K shown in Fig. 32 are obtained by means of drop calorimetry[40~44] except the results by Affortit and Marcon[45], which are obtained by means of direct heating pulse calorimetry. As seen in Fig. 32, the heat capacity curve of UO₂ rises markedly above 2000 K.

Szwarc[46] analized this excess term as a contribution of formation of oxygen Frenkel defects with a formation energy of 1.55 eV/defect:

$$C_p/\mathrm{JK^{-1}mol^{-1}} = 17.78 + 2.04 \times 10^{-3}T + \frac{7.541 \times 10^{10}}{T^2} exp\left(-\frac{14916}{RT}\right). \quad (24)$$

Kerrisk and Clifton[40] made a similar analysis based on their own data and obtained the formation energy of the Frenkel defect as 1.64 eV/defect. Although these analysis fitted well to the experimental heat capacity curve, this interpretation has become doubtful, because the value of defect formation energy obtained by a computer calculation[47] showed to be a much higher value of about 5 eV/defect. Catlow[48] and Thorn et al.[49] have suggested that a contribution of electron-hole disorder in UO₂ is important as the excess heat capacity at high temperatures:

$$2U^{4+} \longrightarrow U^{5+} + U^{3+}. \quad (25)$$

The formation energy for electron-hole disorder is obtained to be 1.64 ~ 1.74

eV/defect by the computer calculation[47]. The heat capacity of UO_2 has recently been reevaluated by Browning[50] and it is expressed as

$$C_p = C_h + C_{ah} + C_d + C_{sh} + C_{eh}, \tag{26}$$

where C_h is the harmonic lattice contribution, C_{ah} the anharmonic lattice contribution, C_d the dilational contribution, C_{sh} the schottky contribution and C_{eh} the contribution due to the electron-hole disorder. The analysis according to Eq. (26) is shown in Fig. 32. From the analysis, he has obtained the value 1.71 eV/defect for the formation energy of the electron-hole disorder, which is in good agreement with the computer calculation[47].

High temperature heat capacities of uranium oxides with higher O/U ratios are shown in Fig. 33. The heat capacities, excluding the heat capacity anomalies, of these compounds can roughly be expressed by the following relation[23]:
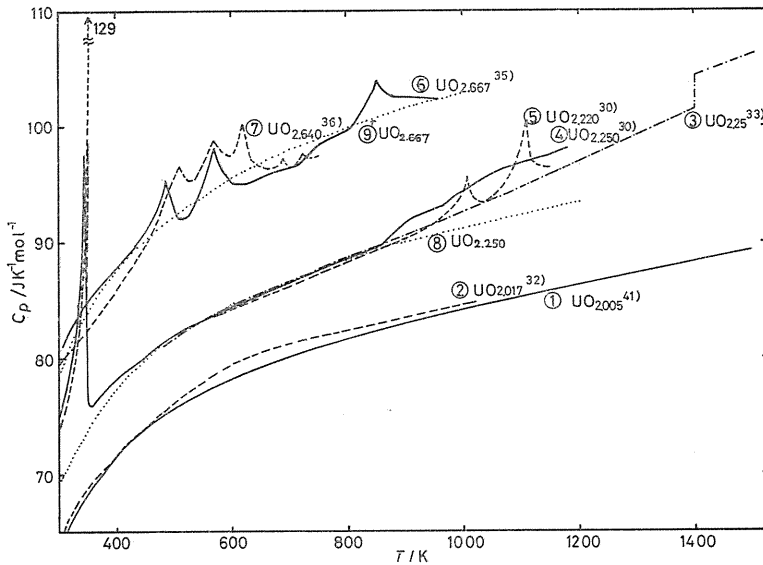
$$C_p(UO_x) = \frac{1+x}{3} \cdot C_p(UO_2), \tag{27}$$

Fig. 33. Heat capacities of UO_{2+x}, U_4O_{9-y} and U_3O_{8-z}.
8. ··· $UO_{2.250}$ calculated by using Eq. (27) and the data of UO_2[41].
9. ··· $UO_{2.667}$ calculated by using Eq. (27) and the data of UO_2[41].

where x is the O/U ratio of the compound ($x>2$). No anomalies in the heat capacity are seen in the UO_2 phase, but many anomalies in U_4O_{9-y} and U_3O_{8-z} phases are found. The order-disorder rearrangement between U^{4+} and U^{5+} ions (U_4O_{9-y}) and that between U^{5+} and U^{6+} ions (U_3O_{8-z}) have been suggested as the main origin of the phase transitions as described in the preceding section.

As seen in the cases of U_4O_{9-y}[24] and U_3O_{8-z}[36], very small changes in non-stoichiometric composition result in large differences in heat capacity anomalies. It has been also shown that the entropy change of phase transition as a function

of the O/U ratio is very valuable for the discussion of the mechanism of the transition. The direct heat capacity measurement can find the heat capacity anomaly, while the enthalpy measurements sometimes miss to find the anomaly, as seen in the heat capacity curve in Fig. 33, where is no anomaly between 900 and 1000 K in curve 3 obtained by drop calorimetry[33], but anomaly is seen in curve 4 by direct heating pulse calorimetry[30].

3. 3. 2. Thermal conductivity of uranium oxides at high temperatures

The thermal conductivity of uranium oxides at various temperatures against the O/U ratio is shown in Fig. 34,[51] based on the results obtained in our laboratory[29,39] and by other workers.[52~54] The thermal conductivity sharply decreases with the O/U ratio in the UO_{2+x} and U_4O_{9-y} phases, but slightly increases with the O/U ratio in the U_3O_{8-z} phase. This strong O/U ratio dependence on the thermal conductivity is thought to be caused by the scattering of phonon by the oxygen interstitials or vacancies in the uranium oxides. The phonon mean path l_L can be expressed by the terms of phonon-phonon interaction (Umklapp-process) and phonon-defect interaction:
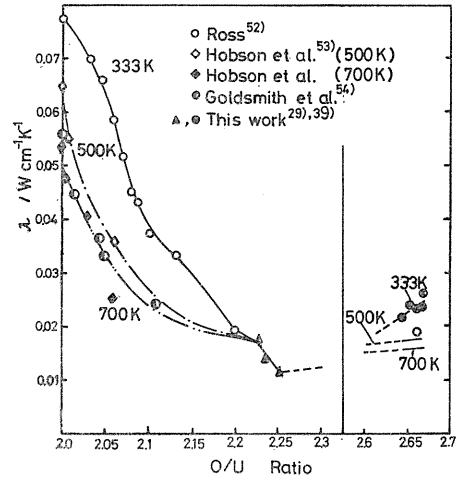

Fig. 34. Thermal conductivity of uranium oxides as a fuction of O/U ratio.[51]

$$1/l_L = 1/l_I + 1/l_U = T/D + E, \qquad (28)$$

where l_U and l_I are the phonon mean free path of Umklapp process and the phonon-defect scattering, respectively, T the temperature, and D and E are the constants depending on the lattice vibration and the defects, respectively. It is expected from the O/U dependence of the thermal conductivity of uranium oxides that E is proportional to the defect concentration. Considering the presence of different types of defects i, $1/l_I$ is expressed as the sum of the reciprocal mean free path due to the individual type of defects $1/l_i$:

$$1/l_I = \sum_i 1/l_i = \sum_i \sigma_i N_i, \qquad (29)$$

where σ_i is the average phonon scattering cross section of the defect type i, and N_i the concentration of the defects. Although the defect structure of uranium oxides is complex, oxygen interstitials for UO_{2+x} and U_4O_{9-y} and oxygen vacancies for U_3O_{8-z} are thought to be the predominant defects for the phonon scattering. With this assumption, the reciprocal phonon mean free path in U_4O_{9-y} is plotted against the defect concentration in Fig. 35[51]. The decrease in $1/l_L$ is explained by the decrease in the concentration of oxygen interstitials. The phonon scattering cross-section due to oxygen interstitials in U_4O_{9-y} can be obtained to be $2.26 \times 10^{-14}/cm^2$ from the slope in Fig. 35 using Eq. (29), where $1/l_U$ is negligibly small

in U_4O_{9-y} and $1/l_L$ is nearly equal to $1/l_I$. Similarly, the phonon scattering cross sections for UO_{2+x} and $(U, Pu)O_{2-x}$ are obtained to be $6.3 \times 10^{-15}/cm^2$ and $6.5 \times 10^{-15}/cm^2$, respectively, using the data of the thermal conductivity by Goldsmith et al.[54] and Schmidt[55], respectively. The phonon scattering cross section in U_3O_{8-z} due to oxygen vacancies is also obtained to be $1.05 \times 10^{-14}/cm^2$ at the low temperature range and $2.5 \times 10^{-14}/cm^2$ at the low temperature range and $2.5 \times 10^{-14}/cm^2$ at the high temperature range using the thermal condcitvity by the authors[39]. The phonon scattering cross section of oxygen interstitials in UO_{2+x} and that of vacancies in $(U, Pu)O_{2-x}$ are the same order of magnitude as the each unit lattice size, and those for U_4O_{9-y} and U_3O_{8-z}

Fig. 35. The reciprocal phonon mean free path against the defect concentration in U_4O_{9-y} at 400 K.[51]

are about four times larger than those for UO_{2+x} and $(U, Pu)O_{2-x}$. This may be caused by the complex defect structures of U_4O_{9-y} and U_3O_{8-z}.
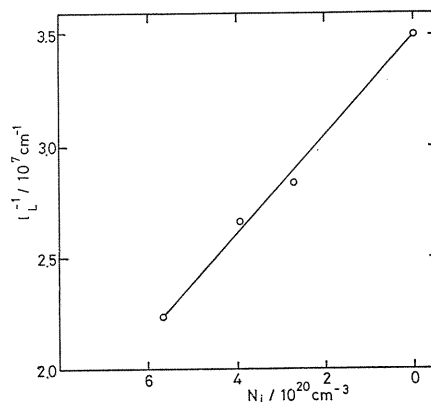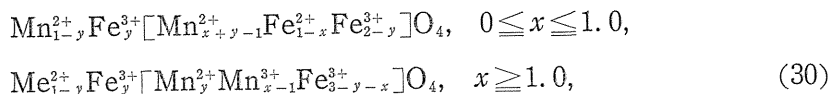
Ⅳ. Heat capacity and thermal conductivity of ferrites

As corrosion products in the coolant system of a nuclear water reactor, various kinds of ferrites such as $Mn_xFe_{3-x}O_4$, $Cr_xFe_{3-x}O_4$ and $Co_xFe_{3-x}O_4$ are thought be formed. Even if the amounts of these corrosion products in water are small, they are activated in the core and form radioactive nuclides such as [54]Mn, [58]Co and [60]Co. As basic data for the corrosion in water reactor, heat of formation, heat capacity and thermal conductivity of these compounds with various compositions would be needed. The compositional dependence of heat capacity are also of great interest, because a ferri-magnetic transition is expected in these compounds.

4. 1. $Mn_xFe_{3-x}O_4$

Manganese ferrites, $Mn_xFe_{3-x}O_4$, have been known to possess a spinel structure, in which the metal ions partially occupy the tetrahedral (A site) and octahedral (B site) interstices of the close-packed oxygen lattice. The cation distribution of $Mn_xFe_{3-x}O_4$ can be expressed as[56]

$$Mn_{1-y}^{2+}Fe_y^{3+}[Mn_{x+y-1}^{2+}Fe_{1-x}^{2+}Fe_{2-y}^{3+}]O_4, \quad 0 \leq x \leq 1.0,$$

$$Me_{1-y}^{2+}Fe_y^{3+}[Mn_y^{2+}Mn_{x-1}^{3+}Fe_{3-y-x}^{3+}]O_4, \quad x \geq 1.0, \tag{30}$$

where the cations before the brackets occupy tetrahedral (A) sites, and those in the brackets the octahedral (B) sites, and y denotes the degree of inversion. Various physical properties of $Mn_xFe_{3-x}O_4$ have been measured as a function of composition x, and discussed in terms of cation distribution among these sites.
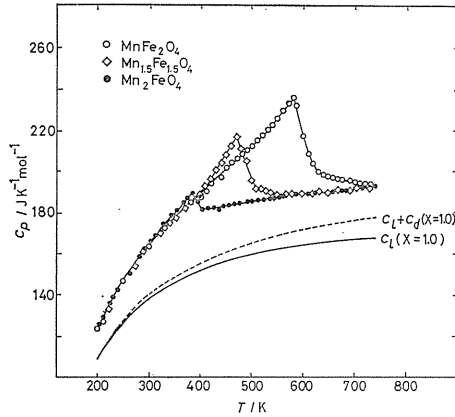
Fig. 36. Heat capacity of $Mn_xFe_{3-x}O_4$.[56]

Since manganese ferrites, $Mn_xFe_{3-x}O_4$, have a ferri-paramagnetic transition, it is expected that the heat capacity anomaly due to the transition depends strongly on the composition x.

The heat capacities of $Mn_xFe_{3-x}O_4$ with the composition $x=1.0$, 1.5, and 2.0 have been measured by means of adiabatic scanning calorimetry, and the results[56] are shown in Fig. 36. As seen in the figure, the λ-type heat capacity anomaly due to the ferri-paramagnetic transition is largely dependent on the composition.

In order to estimate the entropy change due to the transition of $Mn_xFe_{3-x}O_4$, the observed heat capacity, C_p, is considered to be the sum[56]:

$$C_p = C_L + C_d + C_m, \tag{31}$$

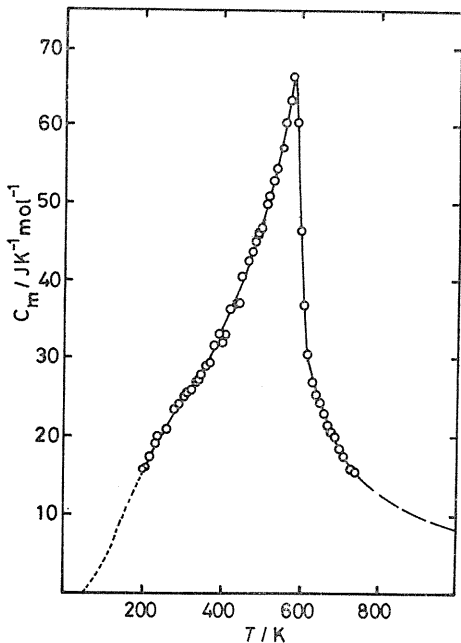where C_L is the lattice contribution, C_d the dilational contribution and C_m the

Fig. 37. Magnetic heat capacity of Mn-Fe$_2$O$_4$[56]: $\bigcirc$, magnetic heat capacity obtained from Eq. (31); - - -, magnetic heat capacity calculated by spin wave theory; — — extrapolated magnetic heat capacity.
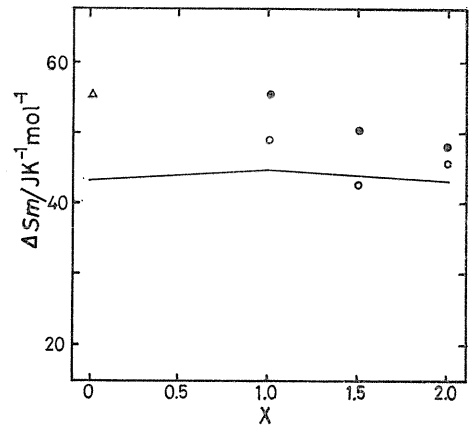

Fig. 38. Entropy change due to ferri-paramagnetic transition of $Mn_xFe_{3-x}O_4$ against composition x[56]
⬤, present experimental results before subtracting the term due to the exchange reaction;
$\bigcirc$, results after subtracting the term due to the exchange reaction:
△, the result of Fe_3O_4 by Grϕnvold and Sveen[58]; ——, calculated entropy change from Eq. (32).

magnetic contribution.   The calculated C_L based on the method proposed by Grimes[57] and C_d are shown in Fig. 36.   The magnetic contribution C_m is obtained by subtracting C_L and C_d from the observed heat capacity C_p.   The resulting C_m for $MnFe_2O_4$ is shown in Fig. 37[56] as an example, showing a usual λ-type curve.   In Fig. 37, a broken line below 200 K represents the magnetic heat capacity calculated from the equation derived by Grimes[57], taking the acoustic and optical branchs of spin wave into account.   From Fig. 37, the entropy change due to the transision ΔS_m (exp) is calculated numerically for $MnFe_2O_4$.   The entropy changes of $Mn_x Fe_{3-x}O_4$ with various x thus obtained are plotted against composition in Fig. 38, where the results of Fe_3O_4 by Grønvold and Sveen[58] are also shown.

The origin of the ferri-paramagnetic transition is thought to be the randomization of unpaired electron spins of each ion, and the entropy change due to the transition can be described, assuming that the cation distribution is expressed by Eq. (30) as follows[56],

$$\Delta S_m(calc.) = R\{(2ln6 + ln5) + (ln6 - ln5)x\}, \quad 0 \leqq x \leqq 1.0,$$
$$= R\{(4ln6 - ln5) - (ln6 - ln5)x\}, \quad x \geqq 1.0, \tag{32}$$

which are also shown a solid line in Fig. 38.   As seen in the figure, the experimental values are from 6 to 10 $JK^{-1}mol^{-1}$ larger than the calculated ones.   An anomaly in the thermal expansion has been observed by Bravers[59] at 400°C, besides the anomay due to the magnetic transition in the sample of $MnFe_2O_4$, and the anomaly is interpreted to be due to the cation exchange reaction.   An additional contribution to the observed entropy change $\Delta S_m(exp.)$ may come from the cation exchange reaction between the tetrahedral and octahedral sites of 2-3 spinel AB_2-O_4:

$$AB_2O_4 \rightleftarrows A_{1-y}B_y[A_yB_{2-y}]O_4, \tag{33}$$
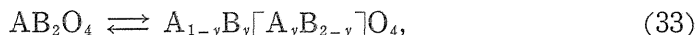
where y and bracket have the same meaning as Eq. (30).   According to Navrotsky and Kleppa[60], the entropy change due to the exchange reaction is considered to be mainly a configurational one, which is expressed by

$$\Delta S(exchange) = -R[ylny + (1-y)ln(1-y) + yln(y/2)$$
$$+ (2-y)ln(2-y)/2], \tag{34}$$

The configurational entropy has a maximum at $y = 3/2$, which corresponds to the random distribution of cations on both sites.   The additional entropy change due to cation exchange can be estimated by Eq. (34) assuming that the reaction Eq. (33) takes place until random distribution of the cations is attained.   The results obtained by subtracting the additional entropy change from the observed entropy change ΔS_m (exp.) are shown in Fig. 38[56] together with $\Delta S_m(calc.)$ for comparison.   As seen in the figure, $\Delta S_m(exp.) - \Delta S(exchange)$ is roughly in agreement with $\Delta S_m(calc.)$.

Thermal conductivity of polycrystal $Mn_x Fe_{3-x}O_4$ samples with various x $(0 \leqq x \leqq 1.5)$ has been measured by means of the scanning temperature method and the results are shown in Fig. 39[61], where the results of Fe_3O_4 by Kamilov et al.[62] and those of $MnFe_2O_4$ by Shchelkotunov et al.[63] are also shown for comparison.
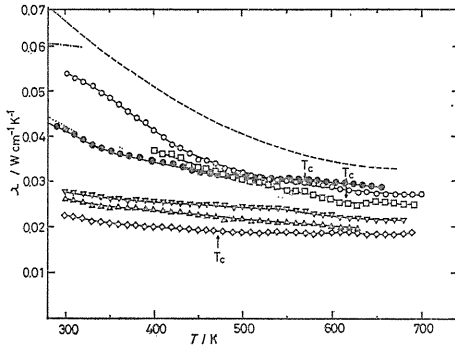
Fig. 39. Thermal conductivity of Mn_xFe_{3-x}-O_4.[61]
  $\triangle$ $Mn_{0.25}Fe_{2.75}O_4$; $\triangledown$ $Mn_{0.5}Fe_{2.5}O_4$;
  $\square$ $Mn_{0.8}Fe_{2.2}O_4$; $\bigcirc$ $MnFe_2O_4$
  $\diamondsuit$ $Mn_{1.5}Fe_{1.5}O_4$
  ⬤ Fe_3O_4 (polycrystal),
  ··· Fe_3O_4 (polycrystal)[62],
  —·—· Fe_3O_4 (single crystal)[62],
  --- $MnFe_2O_4$ by Shchelkotunov et al.[63]

Although the thermal conductivity of the single crystal Fe_3O_4 sample[62] is obtained to be higher than those of the polycrystal samples, the present results on the polycrystal Fe_3O_4 are in good agreement with the results of the polycrystal samples by Kamilov et al.[62]. The thermal conductivities of $Mn_xFe_{3-x}O_4$ with x-values 0.25, 0.5 and 1.5 are observed nearly independent of temperature and lower than $MnFe_2O_4$, as seen in Fig. 39[61]. The peak temperature T_c observed by the diffusivity measurement is indicated by an arrow in Fig. 39, where the anomaly in thermal conductivity due to the magnetic transition is slightly seen in $x=0.8$ but no anomaly is seen in $x=1.0$ and 1.5. The thermal conductivity of ferrites can be considered consisting of the contributions of phonon and magnon, which is expressed with the mean free path concept as follows,

$$\lambda = \lambda_L + \lambda_m$$
$$= (C_L u_L l_L + C_m u_m l_m)/3, \tag{35}$$

where λ, C, u and l are thermal conductivity, heat capacity per unit volume, mean velocity and mean free path of energy carrier, respectively, and the suffix L and m denote the contribution of phonon and magnon, respectively In the magnetic transition, the following two cases would be considered; the one is that λ_m increases due to λ-type magnon heat capacity C_m and the other is that λ_L decreases due to the scattering of phonon with magnon. Since the little change in the thermal conductivity of $Mn_xFe_{3-x}O_4$, is observed at the magnetic transition as seen in Fig. 39, it is likely that the spin-lattice relaxation time is relatively long and the phonon contribution to the thermal conductivity is dominant in the case of $Mn_xFe_{3-x}O_4$.

The composition dependence of thermal

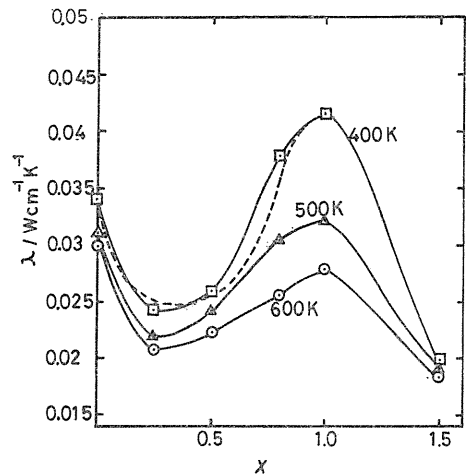Fig. 40. Composition dependence of thermal conductivity of $Mn_xFe_{3-x}O_4$.[61] ----, calculated (400 K).

conductivity of $Mn_xFe_{3-x}O_4$ at each temperature is shown in Fig. 40[61]. Here, two maxima are observed at the composition $x=0$ and 1.0. According to the solid solution model of thermal conductivity proposed by Abeles[64], the scattering of phonons in the mixed substances depends on a scattering cross section Γ, which is expressed by

$$\Gamma = \sum_i x_i [\{(M_i - M)/M\}^2 + \varepsilon\{(\delta - \delta_i)/\delta\}^2], \tag{36}$$

where x_i is the fractional concentration of the component i of solid solution, and M and δ are the average mass and radius per unit atom of solid solution, and M_i and δ_i are the atomic mass and radius when the host lattice is wholly occupied by i-th atom, and ε is regarded as a phenomenological adjustable parameter depending on the nature of bond in the lattice. Using cation radii of Mn^{2+}, Mn^{3+}, Fe^{2+} and Fe^{3+} ions in $Mn_xFe_{3-x}O_4$ given by Gorter[65], the cation distribution shown in Eq. (30) and y value reported by Rieck and Diessens[66], the scattering cross section Γ is calculated assuming ε as 40. With Γ thus obtained and the method by Abeles[64], the composition dependence of thermal conductivity of $Mn_xFe_{3-x}O_4$ is calculated. The results at 400 K are shown in a broken line in Fig. 40, where a good agreement between the observed and calculated is seen. The composition dependence of thermal conductivity of $Mn_xFe_{3-x}O_4$ is mainly explained by the cation distribution in the tetrahedral site, since the difference in Γ comes mainly from the difference in the radius between Mn^{2+} and Fe^{3+} ions in the tetrahedral site.

4. 2. $Cr_xFe_{3-x}O_4$

Iron-chromium spinels, $Cr_xFe_{3-x}O_4$ ($0 \leq x \leq 2$) also possess a spinel structure with the cation distribution[67]:

$$Fe_{1-y}^{3+}Fe_y^{2+}[Fe_{1-y}^{2+}Fe_{1-x+y}^{3+}Cr_x^{3+}]O_4, \tag{37}$$
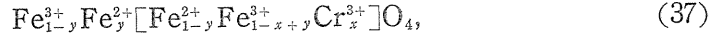
$$y = 0.3x, \quad 0 \leq x \leq 0.3, \tag{37 a}$$

$$y = 0.6(x-0.2), \quad 0.3 \leq x \leq 0.7, \tag{37 b}$$

$$y = x-0.4, \quad 0.7 \leq x \leq 1.3, \tag{37 c}$$

$$y = \frac{1}{7}(x+5), \quad 1.4 \leq x \leq 2.0, \tag{37 d}$$

where the symbols ahead of the brackets denote the cations in tetrahedral (A) site and those inside the brackets the cations in octahedral (B) sites, and y is the degree of inversion.

Since $Fe_{3-x}Cr_xO_4$ exhibits a ferri-paramagnetic transition, it is expected that the heat capacity anomaly due to the transition should depend strongly on the composition x. The heat capacities[67] of $Fe_{3-x}Cr_xO_4$ with $x=0.6$, 0.8, and 1.0 measured by means of adiabatic scanning calorimetry are shown in Fig. 41. As seen in the figure, the λ-type heat capacity anomaly due to the ferri-paramagnetic transition becomes small and broad as x in $Fe_{3-x}Cr_xO_4$ increases. The difference in heat capacities of the samples with various compositions is small except for the temperature range of the transition, as the Kopp-Neumann law predicts.

The observed heat capacity of $Cr_xFe_{3-x}O_4$ can also be expressed by Eq. (31),

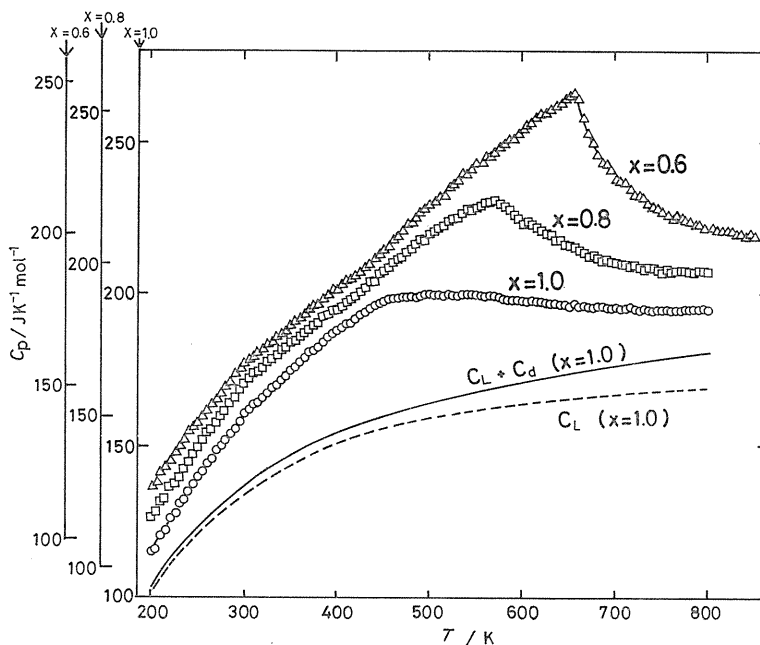Fig. 41. Heat capacity of $Fe_{3-x}Cr_xO_4$[67] Vertical axis is shifted to upper side by 10 and 20 $JK^{-1}mol^{-1}$ for $x=0.8$ and $x=0.6$, respectively.

Fig. 42. Magnetic heat capacity of $Fe_{3-x}Cr_xO_4$.[67] Vertical axis is shifted to upper side by 10 and 20 $JK^{-1}mol^{-1}$ for $x=0.8$ and $x=0.6$, respectively.

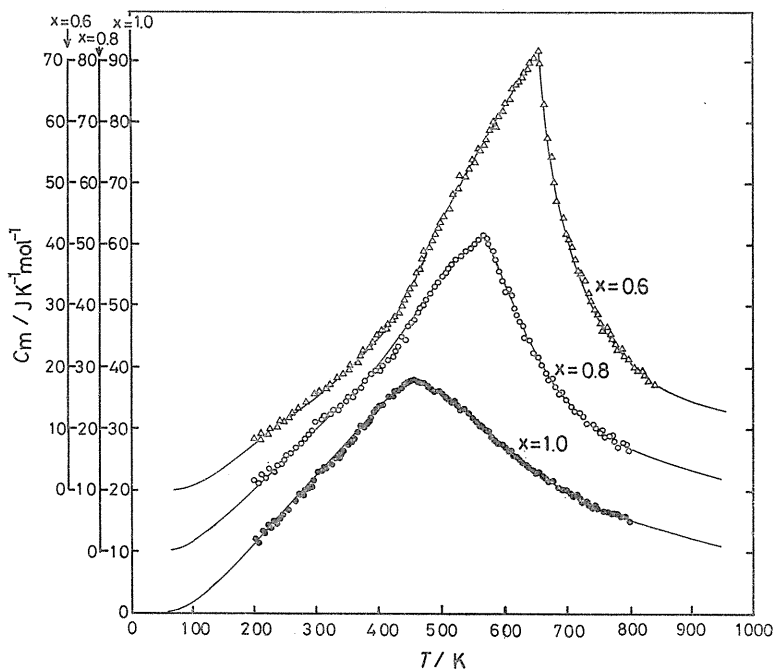and C_L and C_d of $Cr_xFe_{3-x}O_4$ are able to be calculated similarly as the case of $Mn_xFe_{3-x}O_4$. The calculated C_L and $C_L + C_d$ of $CrFe_2O_4$ are shown in Fig. 41, and the magnetic heat capacities calculated by using Eq. (31) are shown in Fig. 42[67], where the heat capacities below 200 K are calculated using Grimes equation[57]. Thus the entropy changes due to the magnetic transition can be obtained by integrating C_m/T, and the results are shown in Fig. 43 as a function of the composition x, where the results of Fe_3O_4 obtained by Grϕnvold and Sveen[58] are also shown for comparison.

The origin of the ferri-paramagnetic transition is thought to be the randomization of unpaired electron spins of each ion. Hence, the entropy change due to the transition is calculated by assuming that the cation distribution is expressed by Eq. (37) as follows,

Fig. 43. Entropy change due to transition as a function of x in $Fe_{3-x}Cr_xO_4$[67]. ○ observed; △ result by Grϕnvold and Sveen;[58] ··· ΔS_{spin} according to Eq.(38); —— $\Delta S_{spin} + \Delta S_{orb}$.

$$\Delta S_{spin} = R[ln5 + (2-x)ln6 + xln4], \quad 0 \leq x \leq 2. \tag{38}$$

ΔS_{spin} is shown against composition as a broken line in Fig. 43. As seen in the figure, the experimental values are 7 to 12 $JK^{-1}mol^{-1}$ higher than the calculated ones.

Grϕnvold and Sveen[58] explained the difference between the experimental and the theoretical entropy changes for Fe_3O_4 by taking into account the orbital contribution to heat capacity due to Fe^{2+} ion in octahedral site to give an additional entropy change $R\ ln\ 3$ or 9.1 $JK^{-1}mol^{-1}$. As for $Fe_{3-x}Cr_xO_4$, this kind of orbital contribution to the heat capacity should be taken into account, since there are octahedral Fe^{2+} ions. As seen in Eq. (37), tetrahedral Fe^{2+} also exists in $Fe_{3-x}Cr_xO_4$, depending on the degree of inversion y. In the case of Fe^{2+} ion in the tetrahedral site, the E_g ground level is split into two levels, and the additional entropy of this term is calculated to be $R\ ln\ 2$ or 5.8 $JK^{-1}mol^{-1}$. Since Fe^{3+} ($3d^5$) and octahedral $Cr^{3+}(3d^3)$ have a nondegenerate ground state, the orbital contribution of these ions is regarded as negligibly small. The total additional entropy change by the orbital contributions is calculated using the cation distribution expressed in Eq. (37) as follows,

$$\Delta S_{orb} = (1 - 0.3x)Rln3 + 0.3Rln2, \quad 0 \leq x \leq 0.3, \tag{39 a}$$

$$\Delta S_{orb} = (1.2 - 0.6x)Rln3 + (0.6x - 0.12)Rln2, \quad 0.3 \leq x \leq 0.7, \tag{39 b}$$

$$\Delta S_{orb} = (1.4 - x)Rln3 + (x - 0.4)Rln2, \quad 0.7 \leq x \leq 1.3, \tag{39 c}$$

where x is the chromium content in $Fe_{3-x}Cr_xO_4$ and R is gas constant. ($\Delta S_{spin} + \Delta S_{orb}$) are shown plotted against composition as a solid line in Fig. 43. The calcu-
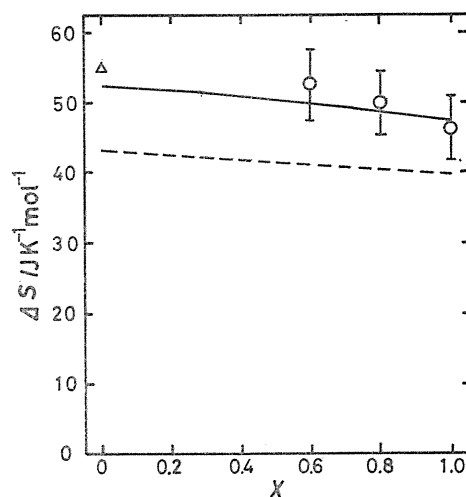
lated $\Delta S_{spin} + \Delta S_{orb}$ are in agreement with the observed values.

4. 3. Heat capacity of ferrites

A brief review on the heat capacity of several kinds of ferrites is to be given below.

Heat capacities of ferrites: Fe_3O_4[58], $CrFe_2O_4$[67], $MnFe_2O_4$[56], $CuFe_2O_4$[68], $NiFe_2O_4$[69], $CoFe_2O_4$[69] and $ZnFe_2O_4$[69] measured by different investigators are shown in Fig. 44. It is seen that heat capacities of these ferrites show anomalies at various temperatures from 500 to 900 K due to para- to ferri-magnetic transition. Heat capacity anomaly in Fe_3O_4 is the largest and its Curie temperature is the highest among the ferrites because of strong Fe^{3+}-Fe^{3+} (A site-B site) interaction. The strength of Fe^{3+}-Fe^{3+} (A-B) interaction, which is responsible for increasing the Curie temperature of inverse spinels, depends on the cation distribution in the spinel.

The site preference energies for some divalent and trivalent ions in spinels empirically obtained by Navrotsky and Kleppa[60] are shown in Fig. 45, where the ion with a positive value prefers the octahedral (A) site and that with a negative value prefers the octahedral (B) site. Since Zn^{2+} strongly prefers the A site, Fe^{3+} cannot enter the A site in $ZnFe_2O_4$. Accordingly, Fe^{3+}-Fe^{3+}(A-B) interaction does not occur in $ZnFe_2O_4$ and no magnetic transition takes place as seen in Fig. 44. Mn^{2+} prefers the A site slightly stronger than Fe^{3+} and the cation distribution of $MnFe_2O_4$ is $Mn^{2+}{}_{0.8}Fe^{3+}{}_{0.2}[Mn^{2+}{}_{0.2}Fe^{3+}{}_{1.8}]O_4$ in accordance with Eq. (30). Since the fraction of Fe^{2+} in the A site is small, the Fe^{3+}-Fe^{3+}(A-B) interaction is weak in $MnFe_2O_4$ and a small heat capacity anomaly is seen at a
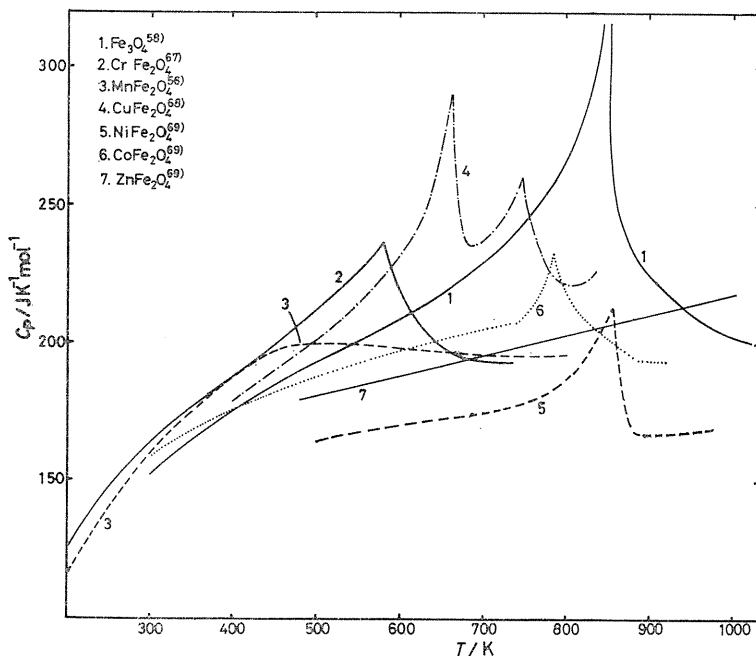

Fig. 44. Heat capacities of ferrites.

lower temperature as shown in Fig. 44. Since the site preference energies of Co^{2+}, Cu^{2+} and Ni^{2+} are between Fe^{3+} and Cr^{3+} and hence the Fe^{3+}-Fe^{3+} (A-B) interaction is fairly strong in $CoFe_2O_4$, $CuFe_2O_4$ and $NiFe_2O_4$, relatively large heat capacity anomalies appear in these ferrites as seen in Fig. 44. In the case of $CuFe_2O_4$, two heat capacity anomalies are observed. A heat capacity anomaly at about 740 K is due to the magnetic transition and that at about 660 K is due to the structural transition associated with the *Jahn-Teller* effect. Since the trivalent Cr^{3+} ion strongly prefers the octahedral site, the number of Fe^{3+} in the octahedral site decreases in $CrFe_2O_4$, which leads to the cation distribution as $Fe^{3+}_{0.4}Fe^{2+}_{0.6}$ $[Fe^{2+}_{0.4}Fe^{3+}_{0.6}Cr^{3+}]$ O_4, and the *Curie* temperature decreases because of the weak Fe^{3+}-Fe^{3+}(A-B) interaction.
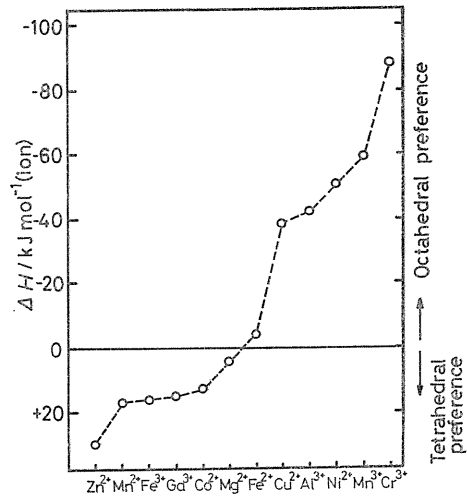

Fig. 45. Empirical site preference energies for some divalent and trivalent ions in the spinel structure[60].

Ⅴ. Calorimetric study of niobium oxides and vanadium oxides

As the first wall and structural materials of nuclear fusion reactor, refractory metals (group 5A and 6A in the periodic table) seem to be promising. But these materials react easily with oxygen, nitrogen and carbon existing in the plasma and coolant such as liquid alkali metals and helium gas. Niobium and vanadium, ones of these potential materials as the first wall, are known to react most readily with oxygen, so that it is important to determine precisely the thermodynamic quantities of these oxides, which are formed by the reaction with oxygen.

### 5. 1. Heat capacity of NbO_2 and doped-NbO_2

Niobium dioxide (NbO_2) is known to have a distorted rutile structure with a tetragonal ($2\sqrt{2}a$, $2\sqrt{2}a$, $2c$) superstructure. A second-order phase transition in NbO_2 has been reported at about 1070 K with a structural change from distorted rutile to rutile structure[70] with a change in electronic band structure[71].

The heat capacity and electrical conductivity have been simultaneously measured by means of direct heating pulse calorimetry[72] and the results of heat capacity are shown in Fig. 46. A λ-type heat capacity anomaly at 1074 K, as shown in the figure, and a sharp increase in the electrical conductivity due to the transition from semiconductor to semi-metal at 1086 K are observed.

The heat capacity is expressed as follows,

$$C_p = C_l + C_d + \Delta C, \tag{40}$$

where C_l is the lattice heat capacity, C_d the dilational contribution and ΔC contains
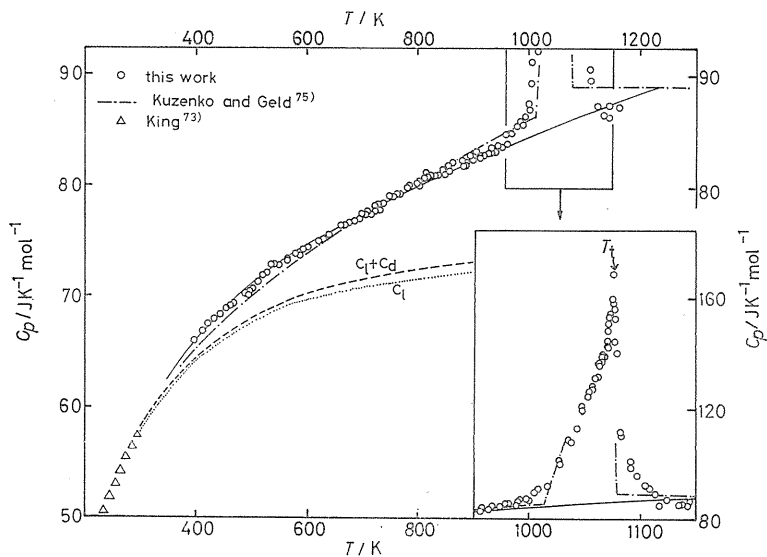
Fig. 46. Heat capacity C_p of NbO_2.[72]

the terms due to the electronic heat capacity and that due to the phase transition. C_l and C_d calculated using the reference data[73,74] are shown in Fig. 46 and the obtained excess heat capacity ΔC and the excess entropy ΔS are shown in Fig. 47, where the excess entropy ΔS at 1120 K is obtained to be 9.35 ± 0.71 $JK^{-1}mol^{-1}$. The excess entropy ΔS consists of the two terms:

$$\Delta S = \Delta S_l + \Delta S_e, \tag{41}$$
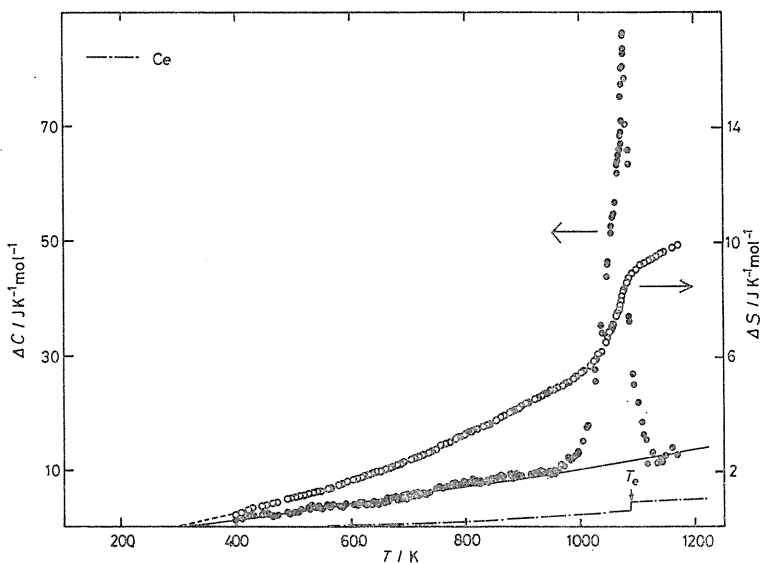
Fig. 47. Excess heat capacity ΔC and excess entropy ΔS of NbO_2.[72]

where ΔS_l is the lattice vibrational term and ΔS_e the electronic term. At the structural phase transition, S_l varies with change of vibrational mode as follows[72],

$$\Delta S_l = S_{l(H)} - S_{l(L)} = \int_0^T C_{l(H)}/T\,dT - \int_0^T C_{l(L)}/T\,dT, \qquad (42)$$

where (H) and (L) represent the high- and low-temperature phases, respectively. In the case of NbO_2, "hard" distorted rutile phase changes to "soft" rutile phase as temperature increases. $C_l(L)$ is obtained from the low temperature heat capacity of NbO_2[73] and $C_l(H)$ is estimated from the heat capacity of TiO_2[76] and Raman spectroscopic data of $Nb_{1-x}TiO_2$[77], which are isostructural with NbO_2 in the high temperature phase. The vibrational excess entropy ΔS_l thus calculated is 4.31 J·K^{-1}·mol^{-1}. The electronic entropy ΔS_e is calculated as 5.71 JK^{-1}mol^{-1}, based on a model of the band structure shown in Fig. 48[72]. The calculated excess entropy ($\Delta S = \Delta S_l + \Delta S_e$) is obtained to be 10.02 JK^{-1}mol^{-1}, which is in fairly good agreement with the observed one 9.35±0.71 JK^{-1}mol^{-1}.
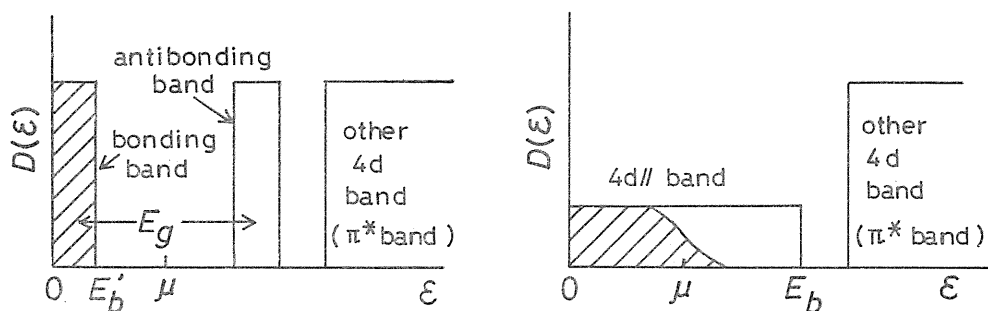

Fig. 48. Model of band structure for NbO_2:[72] (a) low-temperature phase $E_g=77$ kJmol^{-1}, $\mu=43.5$ kJmol^{-1} (b) high-temperature phase $\mu=43.5$ kJmol^{-1},
$D(\varepsilon)=\begin{cases} 2/E_b & \text{if } 0<\varepsilon<E_b \\ 0 & \text{otherwise} \end{cases}$, $E_b=87$ kJmol^{-1}.

Heat capacities of NbO_2 doped with Zr and Mo are also measured and the results[78] are shown in Fig. 49. It is seen from the figure that the heat capacity anomaly of NbO_2 doped with Zr becomes small and shifts to a lower temperature, but that doped with Mo does not change significantly. The doping of Zr and V[79] lowers the transition temperature T_t linearly with the concentration of the doping component, but the doping of Mo gives little effect on the transition. In $Nb_{1-x}V_xO_2$, the valence of each cation is expressed as $(Nb^{4+}_{1-2x}Nb_x^{5+}V_x^{3+})$[79] while in $Nb_{1-x}Zr_xO_2$ as $(Nb^{4+}_{1-x}Zr_x^{4+})$. In the low-temperature phase, the Nb^{4+}–Nb^{4+} pairs in $Nb_{1-x}V_xO_2$ and $Nb_{1-x}Zr_xO_2$ are shown as $([2Nb^{4+}]_{(1-2x)/2}Nb_x^{5+}V_x^{3+})O_2$ and $([2Nb^{4+}]_{(1-2x)/2}Nb_x^{4+}Zr_x^{4+})O_2$, respectively, as shown in Fig. 50, where [2 Nb^{4+}] represents a Nb^{4+}–Nb^{4+} pair. It may be suggested that the content of Nb^{4+}–Nb^{4+} pair in these compounds determines the transition temperature. In Mo-doped NbO_2, Mo^{4+}–Nb^{4+} pairs are formed instead of Nb^{4+}–Nb^{4+} pairs, as suggested from the structure of MoO_2, where Mo^{4+}–Mo^{4+} pairs are formed in the distorted rutile structure. The excess entropy changes ΔS for doped samples are obtained similarly to that for pure NbO_2, and the results are shown in Fig. 51
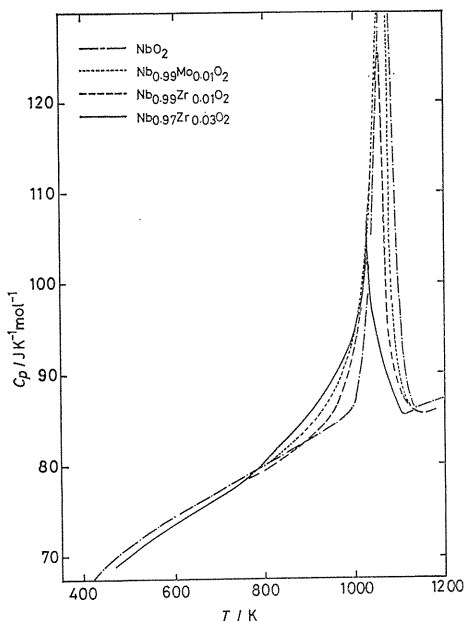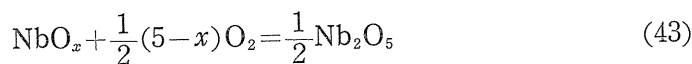
Fig. 49. Heat capacity of doped and undoped NbO_2.[78]

Fig. 50. Electronic configuration of Nb_{1-x}-M_xO_2:[78] (a) M=Zr; (b) M=V; (c) M=Mo.
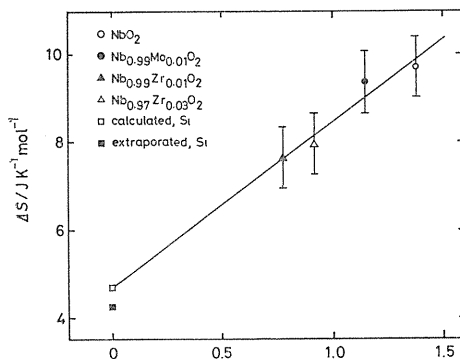
Fig. 51. Dependence of excess entropy change on the jump width of electrical conductivity.[78]

against the jump width J of electrical conductivity. Figure 51 shows that ΔS is proportional to the jump width J as in the cases of U_4O_{9-y}[27] and VO_2[80]. Since the jump in electrical conductivity shows the change in electronic part of the phase transition, the extrapolated excess entropy to $J=0$ indicates the contribution due to the change in lattice vibration ΔS_l. ΔS_l thus obtained is 4.71 $JK^{-1}mol^{-1}$ in good agreement with the value calculated for pure NbO_2, 4.24 $JK^{-1}mol^{-1}$.

5. 2. Heat of formation of niobium oxides

The heat of reaction[81] :

$$NbO_x+\frac{1}{2}(5-x)O_2=\frac{1}{2}Nb_2O_5 \qquad (43)$$

is measured at 920 K with a Tian-Calvet type twin microcalorimeter by introducing excess oxygen gas in order to determine the heats of formation of NbO_x with various x-values. Heats of formation at 298.15K, $\Delta H_f(s, 298.15K)$ for NbO and NbO_2 are obtained as -426.2 ± 5.1 and -792.7 ± 4.2 $kJmol^{-1}$, respectively, which are in good agreement with the JANAF values[82], -419.7 ± 12.6 and -795.0 ± 8.4 $kJmol^{-1}$, respectively. The heats of formation at 920 K for the samples with $x>2.3$ are shown in Fig. 52. It is seen from the figure that in the region NbO_2-$NbO_{2.42}$, the values of $\Delta H_f(NbO_x, s, 920 K)$ vary linearly with the O/Nb ratio.

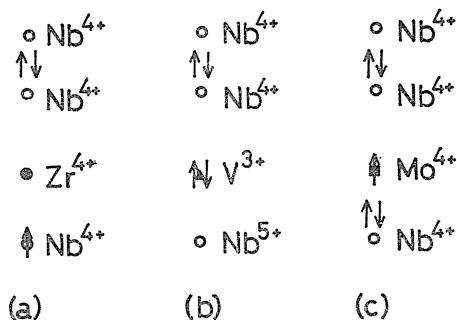Fig. 52. Heat of formation of NbO_x at 920 K against O/Nb ratio.[81]
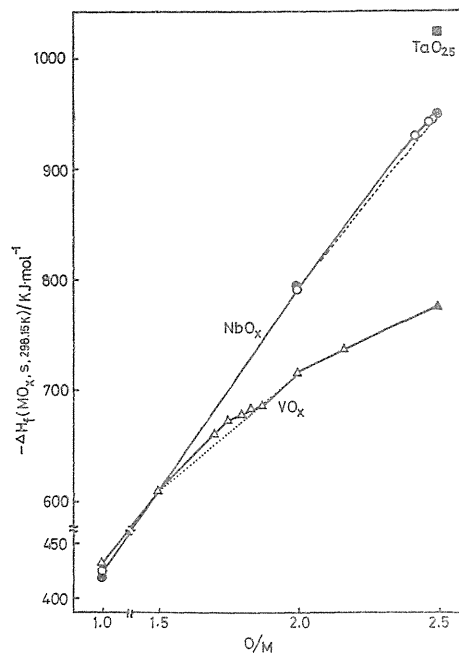
Fig. 53. Heats of formation at 298.15K of NbO_x, VO_x and Ta_2O_5 against the oxygen to metal ratio.[81]

Assuming that the nonstoichiometric range of Ⅱ phase ($NbO_{2.42}$) is very narrow, $\Delta H_f(NbO_{2.42}, s, 920\ K)$ and $\Delta H_f(NbO_{2.42}, s, 298.15\ K)$ are obtained to be -922.4 ± 1.4 and -930.2 ± 1.4 kJmol^{-1}, respectively, using an estimated heated capacity of $NbO_{2.42}$[81]. $\Delta H_f(NbO_{2.42}, s, 298.15K)$ thus obtained is in good agreement with the calculated value -930.5 kJmol^{-1} from the partial molar enthalpy measured by calorimetry in the NbO_2-$NbO_{2.42}$ region by Marucco[83] and the value of heat of formation of NbO_2[82].

The values of $\Delta H_f(NbO_x, s, 298.15K)$ for the niobium oxides obtained in this study are shown as a function of the oxygen to metal ratio in Fig. 53, where the data on 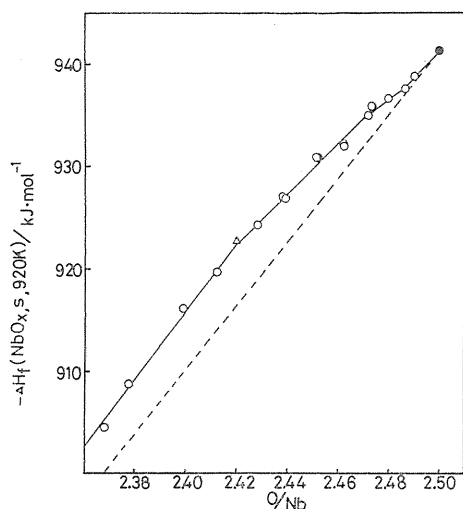VO_x[82,84] and Ta_2O_5[82] are also shown for comparison. It is seen from the figure that $-\Delta H_f$ at 298.15 K is large in the order of $TaO_{2.5}$, $NbO_{2.5}$ and $VO_{2.5}$, which indicates that the metal-oxygen bonding is stronger in the heavier metal compounds. The heats of formation of the intermediate phases, V_nO_{2n-1}, between $VO_{1.5}$ and VO_2 can be compared with the dotted line which connects $-\Delta H_f(VO_{1.5}, s, 298.15\ K)$ and $-\Delta H_f(VO_2, s, 298.15\ K)$[84]. Most $-\Delta H_f$ values of these compounds lie above the dotted line, indicating that these intermediate compounds are energetically more stable than the corresponding mixtures of $VO_{1.5}$ and VO_2. Similar discussion can be made on the intermediate compounds of niobium oxides. As seen in Figs. 52 and 53, $-\Delta H_f$ of $NbO_{2.42}$, $NbO_{2.47}$ and $NbO_{2.485}$ are slightly above the broken line which connects $-\Delta H_f(NbO_2, s, 298,15\ K)$ and $-\Delta H_f(NbO_{2.5}, s, 298.15\ K)$. The most negative value is found in the $NbO_{2.42}$ phase, about 6 kJ mol^{-1} more negative than the corresponding mixture of NbO_2 and $NbO_{2.5}$. The negative value becomes smaller as the O/Nb ratio approaches

2.5. These intermediate compounds are known as the compounds with block struc-
tures, which are thought to be in highly ordered states as in the case of sheared
structures of V_nO_{2n-1}, and therefore the entropy of formation must be relatively
small in the niobium oxides NbO_x with $x > 2.4$ except for the nonstoichiometric
region of $NbO_{2.5-x}$. Hence, it is reasonable that the values of the heat of forma-
tion of the intermediate compounds between NbO_2 and Nb_2O_5 except for $NbO_{2.5-x}$
should have more negative than those of the mixture of NbO_2 and Nb_2O_5.

5. 3. Heat capacity of vanadium-oxygen alloy

Interstitial atoms like oxygen are known to distribute in octahedral sites in
vanadium metal with body-centered cubic structure and form long-range ordered
α' and β' phases for the O/V ratio less than 0.3[85]. In the α' phase, oxygen atoms
preferentially occupy octahedral O_x and O_y sites to give tetragonal symmetry and
form a superstructure with $4 \times 4 \times 6$ metal subcells, where O_x and O_y sites have
their neighboring metal atoms along the axes x and y, respectively Similarly in
the β' phase, oxygen atoms prefer to occupy the O_z site, giving tetragonal sym-
metry, and form a superstructure with $4 \times 4 \times 2$ metal subcells. In the β phase, the

Fig. 54. Heat capacity of $VO_{0.0834}$ and
$VO_{0.1127}$.[86] The left-hand ordinate,
the plots, and the resolution of
heat capacity shown on the lower
side are for $VO_{0.0834}$. The right-
hand ordinate, the plots, and the
resolution of heat capacity shown
on the upper side are for $VO_{0.1127}$.
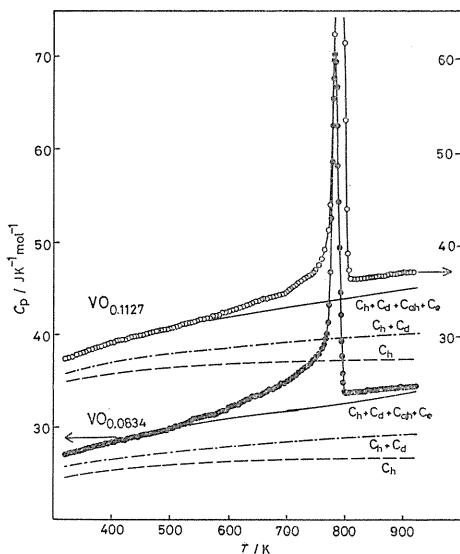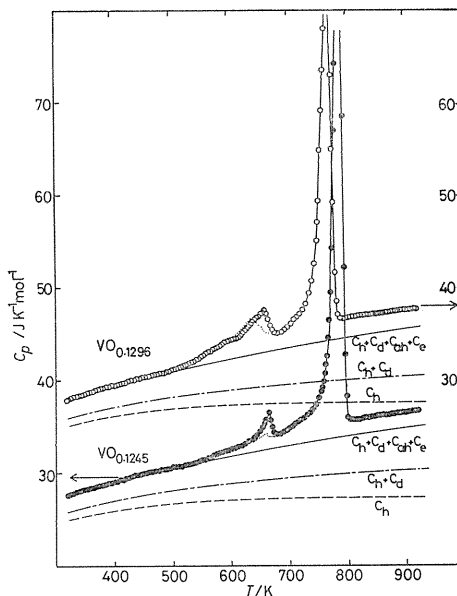
Fig. 55. Heat capacity of $VO_{0.1245}$ and
VO_{1296}.[86] The left-hand ordinate,
the plots, and the resolution of
heat capacity shown on the lower
side are for $VO_{0.1245}$. The right-
hand ordinate, the plots, and the
resolution of heat capacity shown
on the upper side are for $VO_{0.1296}$.
The dotted lines shown between
600 and 700 K are the data for the
second run.

high-temperature form of both α' and β' phases, oxygen atoms preferentially occupy octahedral O_z site to give tetragonal symmetry without long-range ordering.

The heat capacities[86] of $VO_{0.0834}$, $VO_{0.1127}$, $VO_{0.1245}$ and $VO_{0.1296}$ measured by means of scanning calorimetry are shown in Figs. 54 and 55, where a heat capacity anomaly due to order-disorder transition from the α' to β phase is observed around 780 K for each sample and another anomaly from the β' to β phase is observed around 660 K for $VO_{0.1245}$ and $VO_{0.1296}$.

The heat capacity of VO_x, C_p, is expressed by the sum[86]:

$$C_p = C_h + C_d + C_{ah} + C_e + \Delta C, \tag{44}$$

where C_h is the harmonic term of the lattice vibration, C_d the dilational term, C_{ah} the anharmonic term of the lattice vibration, C_e the electronic term, and ΔC the excess heat capacity due to order-disorder transition. The harmonic term of the lattice vibration C_h for VO_x is estimated from the data of elastic constants[87] and neutron inelastic scattering[88]. The thermal expansion of VO_x has been measured[86] using high temperature X-ray diffraction, from which the dilational heat capacity C_d is obtained. C_h and C_d obtained are shown in Figs. 54 and 55. Assuming that at lower temperatures the excess heat capacity is negligibly small and the sum of the electronic and anharmonic terms can be calculated as follows,

$$C_p - C_h - C_d = C_e + C_{ah} = (\gamma + b) T, \tag{45}$$

where γ is the coefficient of the high-temperature electronic heat capacity and b
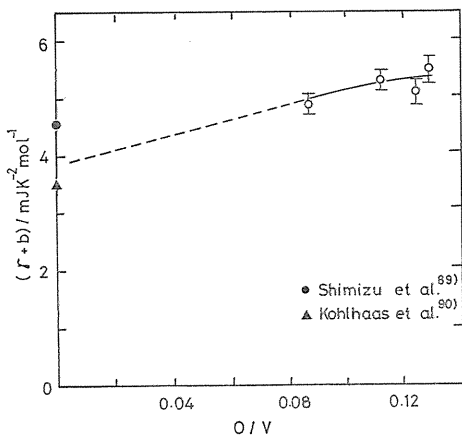

Fig. 56. Sum of the coefficients of electronic and anharmonic heat capacities as a function of O/V ratio at high temperatures.[86]
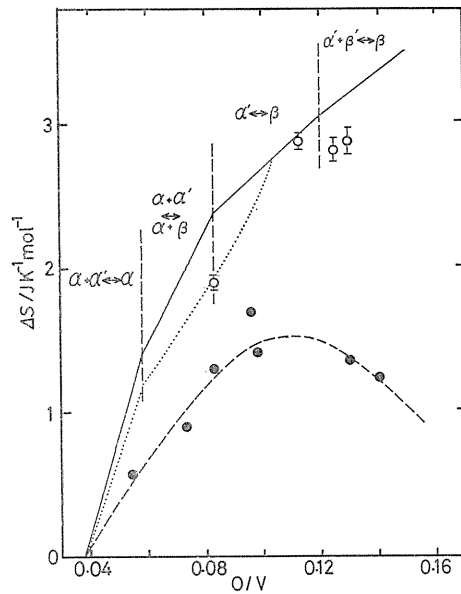
Fig. 57. Observed and calculated entropy changes for the order disorder transition.[86] ○, observed data; --◉--, data by Hiraga and Hirabaya shi;[85] ——, calculated values.

is the coefficient of anharmonic heat capacity. Using the observed values of C_p between 320 and 450 K and the calculated values of C_h and C_d, the value of $(\gamma+b)$ is determined with the condition that the term $(C_p-C_h-C_d)$ vanishes at 0 K. The value of $(\gamma+b)$ obtained is shown in Fig. 56 as a function of O/V ratio. It is seen from the figure that $(\gamma+b)$ gradually decreases with the decrease of O/V ratio, and the extrapolated value O/V=0 is in fairly good agreement with the values of pure vanadium metal obtained from the high temperature heat capacity[89], [90]. The sums thus determined, $C_h+C_d+C_e+C_{ah}$, for various O/V ratios are shown in Figs. 54 and 55. According to Eq. (44), ΔC can be calculated and the entropy change due to order-disorder transition is obtained. The results are shown in Fig. 57, where the sum of the entropy changes for $\alpha'\rightarrow\beta$ and $\beta'\rightarrow\beta$ is shown for the samples with O/V values larger than 0.12, and the results by Hiraga and Hirabayashi are also shown for comparison.

On the other hand, the entropy change due to the order-disorder transition is calculated theoretically as follows. In the O/V$\geq$0.0833 region, the transition $\alpha'\rightarrow\beta$ occurs. Since oxygen atoms occupy only O_z sites in the β phase, the number of available oxygen sites is N and the entropy change ΔS is

$$\Delta S = k\,ln\frac{N!}{xN!(N-xN)!}$$
$$= -R\{x\,ln\,x + (1-x)\,ln(1-x)\}, \quad (x\geq 0.0833) \qquad (46)$$

where perfect ordering in α' phase is assumed. The value of ΔS calculated by Eq. (46) is shown as a solid line in Fig. 57. As seen in the figure, the calculated value of ΔS for $VO_{0.1127}$ is in good agreement with the observed one, but the observed values for other compositions are smaller by about 0.3~0.5 JK^{-1}mol^{-1} than the calculated ones. The difference between the observed and the theoretical entropy changes for $VO_{0.0834}$ can be explained by the residual entropy at low temperatures (see the dotted line in Fig. 57) and those for $VO_{0.1245}$ and $VO_{0.296}$ can be explained by the entropy change due to $\beta'\rightarrow\beta$, which has been reported[85] to be smaller than the theoretical value, since the entropy changes obtained for $VO_{0.1245}$ and $VO_{0.1296}$ are the sum of the entropy changes due to $\beta'\rightarrow\beta$ and $\alpha'\rightarrow\beta$.

5. 4. Heat capacity of niobium oxides and vanadium oxides

A brief review on the heat capacities of niobium oxides and vanadium oxides is to be given in the following. Heat capacities of niobium oxides and vanadium oxides are shown in Fig. 58. $VO_{0.0834}$ and $VO_{0.1296}$[86] show heat capacity anomalies due to order-disorder rearrangement of oxygen atoms, but no corresponding interstitial alloys in an equilibrium state are reported for niobium oxides. VO[91] and NbO[92] show no heat capacity anomaly and heat capacity of VO is larger than that of NbO, indicating the presence of a large excess heat capacity. The origin of the excess heat capacity has not been reported yet, but it would probably be due to the contributions of the anharmonic lattice vibration and conduction electron.

No anomaly in the heat capacity curve of V_2O_3 is observed in the measurement by the drop calorimetry,[93] but a small anomaly is seen around 500 K by the differential scanning calorimetry,[94] where an anomaly in the lattice constant, electrical conductivity and magnetic suspectivity is also detected.
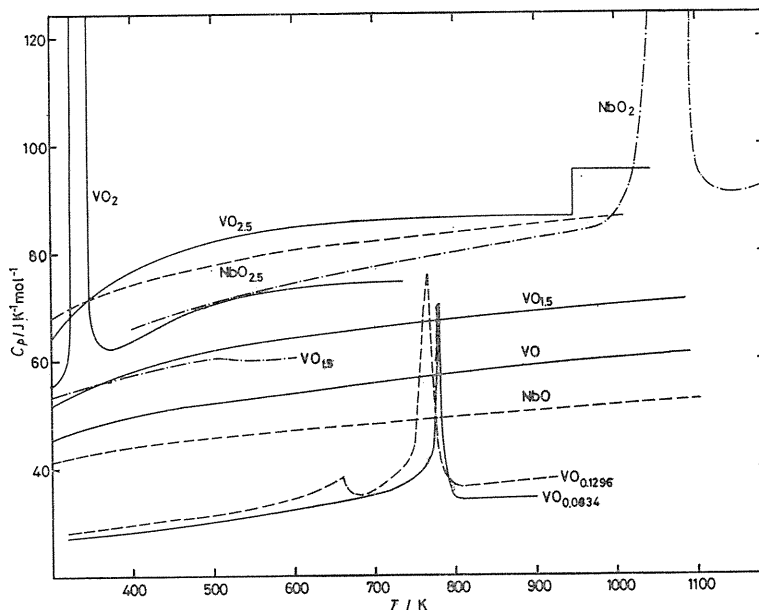
Fig. 58. Heat capacities of vanadium and niobium oxides.

VO_2[95] and NbO_2[72] show a semiconductor-metal transition around 340 and 1070 K, respectively. The difference in the transition temperature between VO_2 and NbO_2 is explained by that in the electronic band structure, especially the energy level of the $\pi*$ band, which is above the antibonding band in NbO_2 whereas it lies between the bonding and antibonding bands in VO[72]. The rather larger heat capacity of NbO_2 above 600 K compared with VO_2 may be explained mainly by the contribution of electronic excess heat capacity in NbO_2[72]. No heat capacity anomaly until the melting point has been reported in Nb_2O_5[96] and V_2O_5[93], and the jump in the heat capacity curve of V_2O_5 at 963 K shown in the figure indicates the occurrence of melting.

Ⅵ. Vaporization of the niobium-oxygen system

The loss of matter owing to vaporization reactions may be the most severe limiting factor in the use of nuclear materials as the nuclear fuels for the nuclear fission reactor and also in the use of the materials as the first wall for the nuclear fusion reactor. In addition to providing the vapor pressure data necessary for the calculation of vaporization loss, the study of vaporization process gives the free energy and enthalpy differences between the products and reactants, from which the nature of high temperature reactions, the energies of chemical bonding in gaseous species, the thermodynamic properties of solids and liquids concerned (the formation energy, the partial molar enthalpy and entropy and defect structure), and phase relation at high temperature can be determined.

As mentioned in the preceding section, refractory metals (group 5A and 6A in

the periodic table) are promising as first wall and structural materials of nuclear fusion reactor. Hence, the study on vaporization of niobium oxides has been carried out in our laboratory in a recent few years. Although some studies on the NbO, NbO_2 and Nb_2O_5 phases have been done by several investigators[97~101], the enthalpies of formation of $NbO_2(g)$ and $NbO(g)$ calculated from the previous studies are not in good agreement and vary from -162.3 to -223.0 kJ·mol⁻¹ and from 152.0 to 211.4 kJ·mol⁻¹, respectively. The vaporization study of NbO_2 (s, l) by mass-effusion method (weight loss measurements) and the studies of Nb–O solid solution and Nb_2O_5 by mass-spectrometric method have not yet been undertaken.

The purpose of the present study is (1) to clarify the congruently vaporizing phase and composition in the Nb–O system; (2) to measure the partial vapor pressures of NbO_2 (g) and NbO (g) as a function of composition, from which the thermodynamic quantities such as enthalpy of formation and dissociation energy for $NbO_2(g)$ and $NbO(g)$ are determined; (3) to determine the partial molar enthalpy and entropy of oxygen, from which the defect structure is to be estimated; (4) to establish the phase relation for the Nb–O system at high temperature.

The apparatus and experimental procedures used for the vaporization study are described in section 2.4. Sample preparation and analysis are shown in the previous papers[102~106].

6. 1. Congruence of the vaporization

6. 1. 1. Congruently vaporizing phase

Vaporization of the four phases, NbO, NbO_2, $Nb_{12}O_{29}$ and Nb_2O_5, was studied in the temperature range from 1655 to 2132 K to determine the congruently vapori zing phase by mass-effusion and Langmuir free vaporization methods[102]. The results are shown in Tables 3 and 4.

For the NbO phase, Shchukarev et al.[101] have suggested that the vaporization is incongruent and the reactions are expressed as $NbO(s)=NbO(g)$ and $2NbO(s)=Nb(s)+NbO_2(g)$ by mass-spectrometric method. We have found the presence of Nb and/or NbO phases as the residue after vaporization, which indicates that NbO (s) is the incongruently vaporizing phase[102].

For the NbO_2 phase, the results by mass-effusion method[102] confirmed that $NbO_2(s)$ vaporizes congruently, although the congruent vaporization of $NbO_2(s)$ was suggested by Shchukarev et al. by the mass-spectrometric study[101].

For the $Nb_{12}O_{29}$ phase, the vaporization study has not been reported previously. Although it is suggested by our study[102] that the vapor over $Nb_{12}O_{29}$ is oxygen rich, the identification of vapor species by mass-spectrometry is to be called for.

For the Nb_2O_5 phase, Golubtsov et al.[97] have suggested by mass-effusion method that the vaporization process may be expressed as $Nb_2O_5(s)=2NbO_2(g)+1/2O_2(g)$ in the temperature range from 1432 to 1756 K. The results obtained in our study[102] in the temperatures range from 1803 to 1893 K above the melting point of Nb_2O_5 (m. p.≃1769 K) indicated that the vapor species over Nb_2O_5 is oxygen rich, hence, Nb_2O_5 vaporizes incongruently and the residue approaches the NbO_2 phase.

It is concluded from these results that the NbO, $Nb_{12}O_{29}$ and Nb_2O_5 phases vaporize incongruently and the NbO_2 phase is the only phase to vaporize congruently.

Table 3. Vaporization characteristics: mass-effusion method[102].

Initial phase[a]	Vaporization conditions			Phases of the residue[a]
	T(K)	Time(h)	Vap. frac.[b]	
NbO	2032	13.0	0.02	NbO
NbO	2053	13.0	0.02	NbO
NbO	2073	24.0	0.02	NbO
NbO	2086	21.0	0.02	NbO
NbO	2092	13.0	0.02	NbO
NbO	2114	14.5	0.08	Nb+NbO
NbO	2125	32.0	0.23	Nb+NbO
NbO_2	1953	22.0	0.03	NbO_2
NbO_2	1990	14.5	0.03	NbO_2
NbO_2	2013	12.0	0.03	NbO_2
NbO_2	2042	12.0	0.04	NbO_2
NbO_2	2052	5.7	0.03	NbO_2
NbO_2	2103	5.0	0.07	NbO_2
NbO_2	2132	8.0	0.03	NbO_2
$Nb_{12}O_{29}$	1655	4.5	<0.01	NbO_2
$Nb_{12}O_{29}$	1698	6.0	<0.01	NbO_2
$Nb_{12}O_{29}$	1729	8.0	<0.01	NbO_2
$Nb_{12}O_{29}$	1866	7.3	0.03	NbO_2
Nb_2O_5	1803	2.5	0.02	several phases[c]
Nb_2O_5	1823	30.0	0.46	NbO_2

a) Phase analysis was carried out by X-ray diffraction.
b) Fraction of the samples vaporized. Vaporized fraction is defined as the ratio of weight loss of samples after vaporization to the initial weight.
c) Residue phases are consisting of several phases including the $Nb_{12}O_{29}$ phase between Nb_2O_5 and NbO_2 which are identified by using the X-ray data obtained by the authors[114].

Table 4. Vaporization characteristics: Langmuir free vaporization method[102].

Initial phases[a]	Vaporization conditions			Phase of the residue[a]
	T(K)	Time(h)	Vap. frac.[b]	
NbO	2053	14.0	0.56	NbO
NbO_2	2073	6.0	0.35	NbO_2
Nb_2O_5	1823	10.0	0.06	several phases[d]
Nb_2O_5	1893	3.0	——[c]	several phases[d]
Nb_2O_5	1893	5.0	——[c]	NbO_2

a) Phase analysis was carried out by X-ray diffraction.
b) Fraction of the samples vaporized.
c) Not measured.
d) Residue phases are consisting of several phases between Nb_2O_5 and NbO_2 which are identified by using the X-ray data obtained by the authors[114].

6. 1. 2. Congruently vaporizing composition

The composition at which the NbO_2 phase vaporizes congruently can be determined from the compositional dependence of the total vapor pressures. Since the main vapor species over the NbO_2 (s, l) phase are NbO_2 (g) and $NbO(g)$ as will be discussed in section 6. 2. 1., the total vapor pressure is determined mainly by the sum of the vapor pressures of NbO_2 (g) and NbO (g). As shown in Fig. 59, the congruently vaporizing composition determined at 2000 K is to be stoichiometric $NbO_{2.000}$[103].

The partial vapor pressures of O (g) and O_2 (g) can be calculated from the partial vapor pressures of NbO_2 (g) and NbO (g) over NbO_2 (s) which vaporizes congruently, on the basis of the following gas reactions[103]:
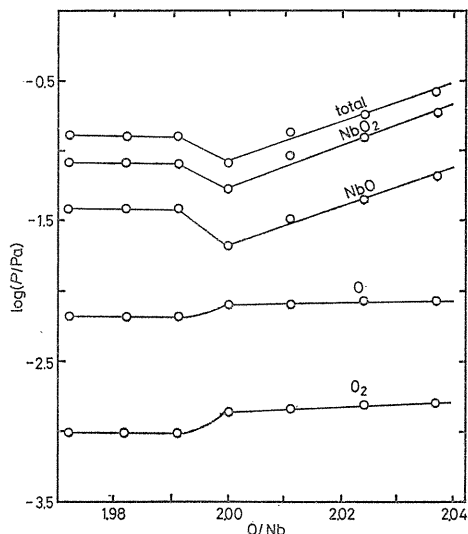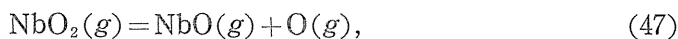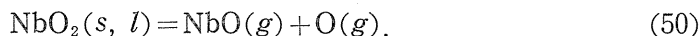

Fig. 59. Total vapor pressures and partial vapor pressures of $NbO_2(g)$, NbO (g), $O(g)$ and $O_2(g)$ as a function of the O/Nb ratio at 2000 K.[103]

$$NbO_2(g) = NbO(g) + O(g), \qquad (47)$$

$$O(g) = 1/2 O_2(g). \qquad (48)$$

The gas equilibrium constant for the reaction (47) used for the calculation was derived from the partial vapor pressures of $NbO_2(g)$, $NbO(g)$ and $O(g)$ over the stoichiometric $NbO_{2.000}$[102,103]. The partial vapor pressure of $O(g)$ over the stoichiometric $NbO_{2.000}(s, l)$ was calculated from the equation:

$$P_O = P_{NbO}(M_O/M_{NbO})^{1/2}, \qquad (49)$$

where M_{NbO} and M_O are the molecular weights of NbO and O, respectively, since the $NbO_{2.000}(s, l)$ vaporizes congruently according to the reaction:

$$NbO_2(s, l) = NbO(g) + O(g). \qquad (50)$$

The gas equilibrium constant for the reaction (48) was taken from JANAF tables[107]. The partial vapor pressures of $O(g)$ and $O_2(g)$ thus calculated at 2000 K are also shown in Fig. 59. The total vapor pressures at various temperatures are shown as a function of the O/Nb ratio in Fig. 60[103]. As shown in these figures, the congruently vaporizing composition was observed to be O/Nb = 2. 000 independent of temperature in the range between 1900 and 2025 K[103].

Fig. 60. Total vapor pressures as a function of the O/Nb ratio at various temperatures.[103]
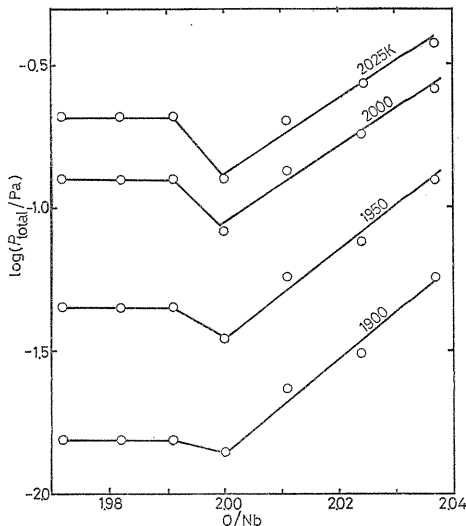
6. 2. Vapor pressures

6. 2. 1. $NbO_2(s, l)$

The partial vapor pressures of $NbO_2(g)$, $NbO(g)$ and $O(g)$ over $NbO_2(s)$ calculated from the total weight loss measurements with use of mass-spectrometric data are shown as a function of temperature in Fig. 61, where the partial vapor pressures of $NbO_2(g)$ and $NbO(g)$ over $NbO_2(s)$ and $NbO_2(l)$ obtained solely by the mass-spectrometric method are also shown[102]. The partial vapor pressures of NbO_2 (g) and NbO (g) measured by mass-effusion method are in good agreement with those obtained by mass-spectrometric method. The partial vapor pressures of $NbO_2(g)$ measured by Shchukarev et al.[101] are considerably (about a factor of 10) higher than our results[102], as seen in Fig. 61, and those of NbO (g) by Shchukarev et al.[101] are approximately a factor of 5 lower than ours. X-ray analysis of the residue after vaporization in our study indicated the existence of a single NbO_2 phase and the O/Nb compositions were not changed from those of the starting sample (2.000 ± 0.003) within experimental error. The sample powder used for the vaporization experiment by Shchukarev et al.[101] was reported to be single phase of NbO_2 with an O/Nb composition of 2.008. The disagreement between our results and the results by
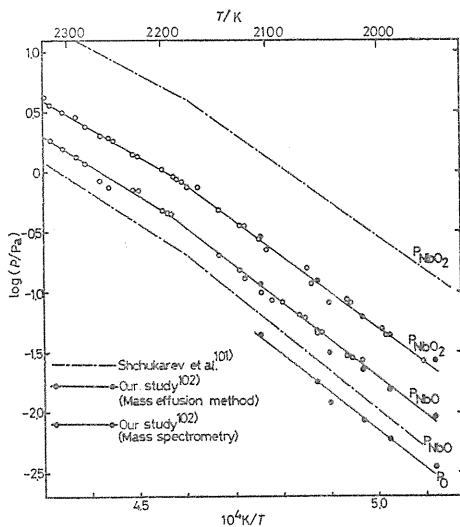

Fig. 61. The equibrium partial vapor pressures of $NbO_2(g)$ and $NbO(g)$ over $NbO_{2.00}(s)$ as a function of the reciprocal temperatures.[102]

Shchukarev et al. may be caused by the difference of the oxygen content of the NbO_2 samples.

As seen in Fig. 61, a change of slope in the plot of vapor pressures vs. reciprocal temperature is observed at 2188 ± 10 K corresponding to the melting point of NbO_2[102]. The melting point of NbO_2 has been reported previously to be 2191 K by the metallographic method[112] and also 2173 K by vapor pressure measurements[101]. The enthalpy and entropy of fusion of NbO_2 estimated from our vaporization data[102] are summarized in Table 5 together with the results of Nb_2O_5[104,108].

Table 5. Enthalpy and entropy of fusion.

Phase	Melting Temp./K	$\Delta H_m/$ kJ·mol^{-1}	$\Delta S_m/$ J·mol^{-1}K^{-1}	Method	Investigators
NbO_2	2188 ± 10	99.6 ± 11.7	45.5 ± 5.4	mass-spectr.	Matsui and Naito[103]
	2173	92	42	mass-spectr.	Shchukarev et al.[101]
Nb_2O_5	1772 ± 5	108.4 ± 19.8	60.7 ± 11.1	mass-spectr.	Matsui and Naito[104]
	1785	102.5	57.6	heat capacity	Orr[108].

6. 2. 2. $NbO_{2 \pm x}(s)$

The partial vapor pressures obtained for hyperstoichiometric $NbO_{2+x}(s)$ and for hypostoichiometric $NbO_{2-x}(s)$ are shown as a function of the reciprocal temperature in Figs. 62 and 63, respectively[103]. At two temperatures shown as Tr_1 and Tr_2 in Fig. 62, the changes of slope in the plot of partial vapor pressures vs. reciprocal temperature are observed for each hyperstoichiometric $NbO_{2+x}(s)$. From the results of the X-ray analysis and the observation of state of the residues, it is concluded that the change at temperatures Tr_1 corresponds to the transition from $NbO_{2+x}(s)$ to the mixture of $NbO_{2+x}(s)$ and liquidus solution, and the change at temperatures Tr_2 around 2188 K corresponds to the transition from the mixture of liquidus solution and $NbO_{2+x}(s)$ to the liquidus solution.

It is noted that the discontinuities in the plot of partial vapor pressure vs. reciprocal temperature observed for the hyperstoichiometric NbO_{2+x} are not usually compatible with the thermodynamic principles. However, the vapor pressure data were obtained reproducibly on heating and cooling, and no change in O/Nb composition and temperature during the measurements were observed. Accordingly these discontinuities in the vapor pressure data can be used as an indication of the phase change. The abnormal changes in the vapor pressure-temperatre curves at the phase transitions from the thermodynamic point of view, have been also observed in some previous works[109~111], though a clear explanation for these observations has not been given.

The change of slope in the vapor pressure-temperature curve is also observed at two temperatures (Tr_1 and Tr_2) for hypostoichiometric $NbO_{2-x}(s)$ as shown in Fig. 63[103]. In this figure, it is considered that the transition temperature Tr_1 (2103 ± 5 K) corresponds to the solidus temperature, that is, the transition temperatue from the mixture of $NbO(s)$ and $NbO_{2-x}(s)$ to the mixture of liquidus solution and $NbO_{2-x}(s)$, and the transition temperature Tr_2 (2188 ± 10 K) corres
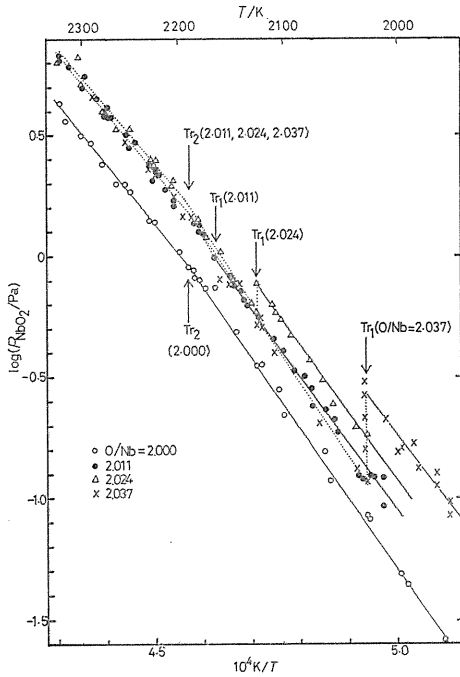
Fig. 62-a Partial vapor pressures of NbO_2 (g) over hyperstoichiometric $NbO_{2+x}(s)$ as a function of the reciprocal temperatures.[103]

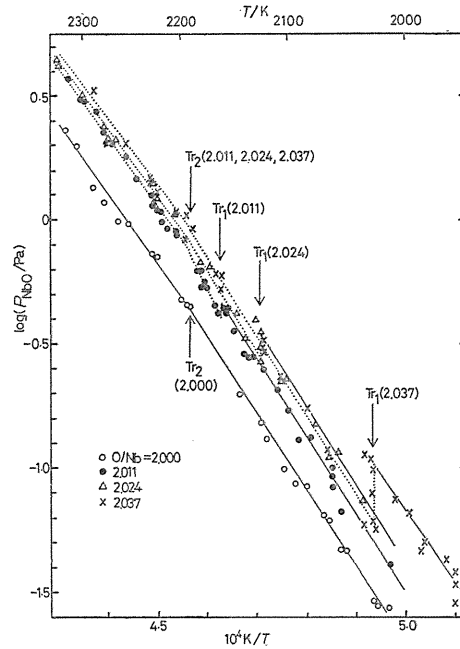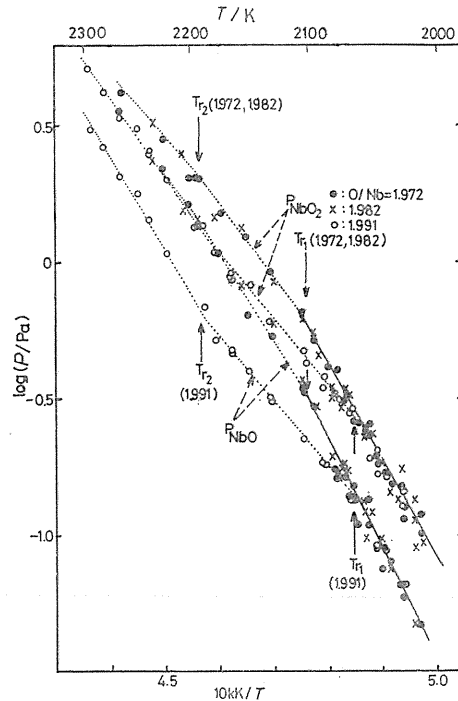

Fig. 62-b Partial vapor pressures of NbO (g) over hyperstoichiometric $NbO_{2+x}(s)$ as a function of reciprocal temperatures.[103]

ponds to the transition from the mixture of liquidus solution and NbO_{2-x} (s) to liquidus solution. The change of slope of the partial vapor pressure curve is also observed for $NbO_{1.991}$ at two temperatures 2063 ± 5 and 2188 ± 10 K. From the X-ray analysis and the observation of the residue after vaporization, it is estimated that the phase existing between 2063 and 2188 K is the $NbO_{2-x}(s)$ phase and that above 2188 K is liquidus solution and the phase below 2063 K is the mixture of $NbO(s)$ and $NbO_{2-x}(s)$.

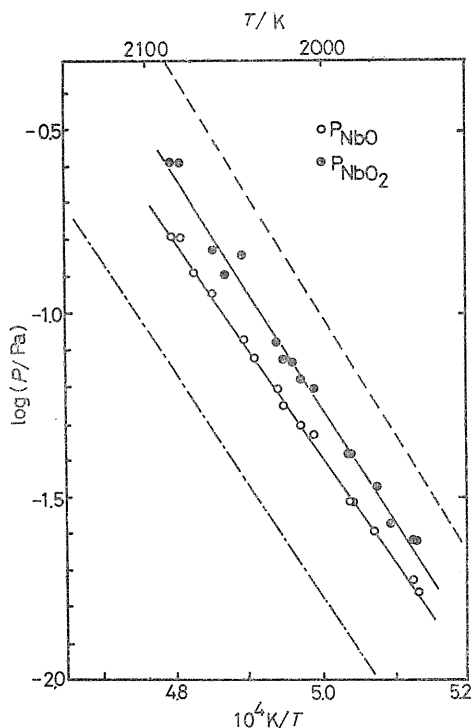Fig. 63 Partial vapor pressures of $NbO_2(g)$ and $NbO(g)$ over $NbO_{1.972}(s)$, $NbO_{1.982}$ (s) and $NbO_{1.991}(s)$ samples.[103]

6. 2. 3. NbO(s)

The incongruency of the vaporization process of NbO(s) was observed from the change of the partial vapor pressures of $NbO_2(g)$ and NbO(g) with time in our study,[105] in accordance with the compositional change during the vaporization at high temperatures above 2100 K near the melting point. To keep the compositional change of the NbO phase as small as possible during the vaporization experiment, all measurements of the vapor pressures over NbO(s) reported were carried out within 2 h in a relatively low temperature range from 1948 to 2085 K.

The partial vapor pressures of $NbO_2(g)$ and NbO(g) over nearly stoichiometric $NbO_{1.003}(s)$ thus obtained[105], are shown in Fig. 64 as a function of the reciprocal temperature together with the results by Shchukarev et al.[101] As seen in the figure, the vapor pressure ratio of P_{NbO_2}/P_{NbO} over $NbO_{1.003}(s)$ observed in our study is considerably small compared with that over $NbO_{0.99}(s)$ measured by Shchukarev et al., similar to the case of $NbO_2(s)$[102]. The vapor pressures obtained by Shchukarev et al. are thought to be those over the samples reduced during the vaporization, since they reported that the residue after vaporization was the mixture of Nb and NbO, different from the starting $NbO_{0.99}(s)$. But the vapor pressure ratio of P_{NbO_2}/P_{NbO} reported by Shchukarev et al. is considered to be too high even though it is for the two phase mixture of NbO(s) and Nb(s).

Fig. 64. Vapor pressures of $NbO_2(g)$ and NbO (g) over NbO(s), ●: P_{NbO_2}, ○: P_{bON} over $NbO_{1.003}(s)$ by Matsui and Naito[105], --: P_{NbO_2}, -·-: P_{NbO} over $NbO_{0.99}(s)$ by Shchukarev et al.[101]

6. 2. 4. Two-phase mixture of Nb(s) and NbO(s)

The partial vapor pressure of NbO_2 (g) and NbO (g) over the two-phase mixture of Nb(s) and NbO(s) measured in the temperature range 1971~2175 K are shown as a function of the reciprocal temperature in Fig. 65[105]. As seen from the figure, the main gaseous species are $NbO_2(g)$ and NbO(g) similar to those over NbO(s), but the vapor pressure ratio of P_{NbO_2}/P_{NbO} is different. Over the mixture of Nb(s) and NbO(s), the partial vapor pressures of NbO(g) are considerably (about a factor of 3 to 4) higher than those of $NbO_2(g)$, while the partial vapor pressures of NbO(g) over single-phase NbO(s) are approximately a factor of 1.3 lower than those of $NbO_2(g)$.

As seen in Fig. 65, the change of slope in the plot of the vapor pressures over the mixture NbO(s) and Nb(s) vs. the reciprocal temperatue was observed at 2178 ± 10 K corresponding to the transition temperature from the mixture of Nb(s) and NbO(s) to the mixture of the liquidus solution and Nb(s), which is in good agreement with the transition temperature 2188 K reported by Elliott previously with the metallographic method[112].
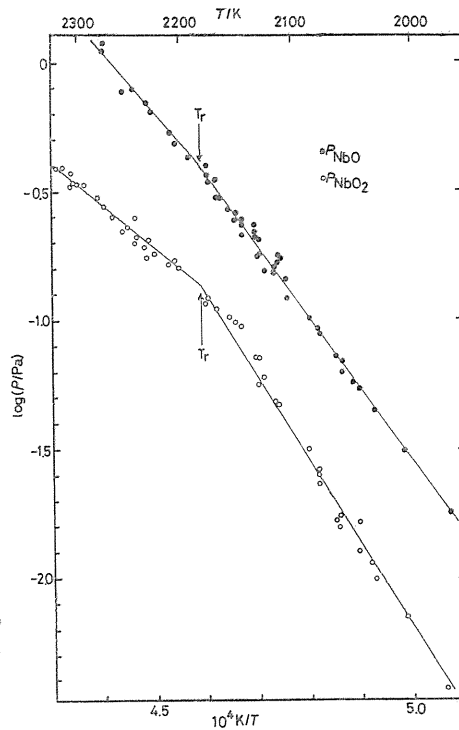
Fig. 65. Vapor pressures of $NbO_2(g)$ and NbO (g) over the two-phase NbO(s)+Nb(s) mixture.[105]

6. 2. 5. $Nb_2O_5(s, l)$

The partial vapor pressurs of $NbO_2(g)$ over $Nb_2O_5(s, l)$ were measured by the authors[104], but those of NbO(g) and $O_2(g)$ could not be measured due to the lower vapor pressures than the detection limit of the mass spectrometer used and to the non-condensable gas, respectively. The results are shown in Fig. 66 together
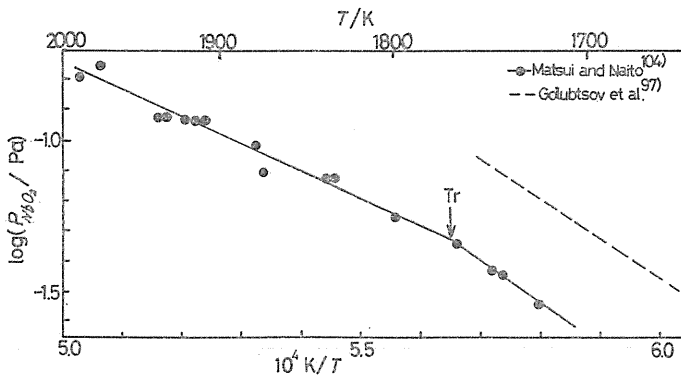
Partial vaper pressures of NbO_2 over Nb_2O_5 (s,l)

Fig. 66. Vapor pressure of $NbO_2(g)$ over $Nb_2O_5(s,l)$.[104]

with the previous results by Golubtsov et $al.$[97], whose results are about two times higher than ours, although the slope in the plot of vapor pressures vs. reciprocal temperature is observed to be fairly in good agreement with each other. As seen in the figure, the change of slope is observed at 1772 K corresponding to the melting temperature of $Nb_2O_5(s)$. The melting temperatures of Nb_2O_5 reported previously are inconsistent and exist between 1738 and 1785 K[108, 112, 113]. The melting temperature 1772 K obtained in this study is close to 1768 K reported by Elliott[112] and 1764 K by Holtzberg[113]. The enthalpy and entropy of fusion of Nb_2O_5 calculated from our vaporization data are summarized in Table 5.

6. 2. 6. Two-phase mixture of $NbO_{2+x}(s)$ and liquid

The vapor pressures of $NbO_2(g)$ and $NbO(g)$ over two-phase mixture of $NbO_{2+x}(s)$ and liquid $(2.063 \leq O/Nb \leq 2.386)$ measured by the authors are shown in Fig. 67[104].

In Fig. 67, the temperatures at which the slopes in the plot of vapor pressures vs. reciprocal temperature change or the vapor pressures increase rapidly, are observed. These temperatures are considered to correspond to the liquidus line, that is, the transition temperatures from the mixture of $NbO_{2+x}(s)$ and liquidus solution to the single liquidus solution, by the observation of the state of the residues quenched from the temperatures above and below the transition temperature.
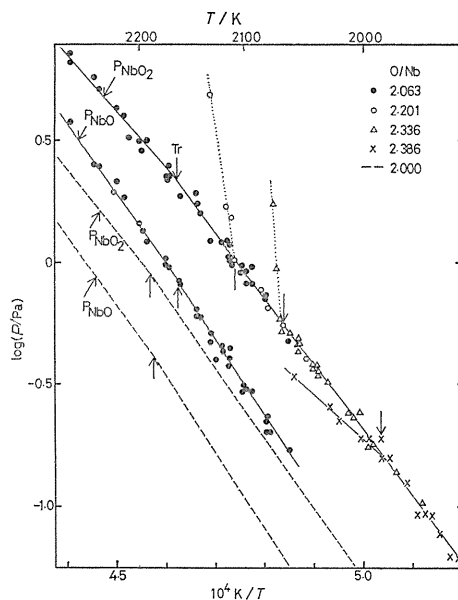

Fig. 67. Vapor pressures of $NbO_2(g)$ and NbO (g) over NbO(s)+liquid[104].

6. 2. 7. Nb-O solid solution

The partial vapor pressures of $NbO(g)$ and $NbO_2(g)$ over the niobium-oxygen solid solution are shown in Figs. 68 and 69, respectively, together with the results over the mixture of $Nb(s)$ and $NbO(s)$[106].

The change of slope in the plot of partial vapor pressures of $NbO(g)$ and $NbO_2(g)$ vs. reciprocal temperature is observed at three temperatures shown as Tr_1, Tr_2 and Tr_3 in Figs. 68 and 69 for the samples with O/Nb atomic ratio between 0.059 and 0.066. On the other hand, the change of slope is observed at only one temperature shown as Tr_3 for the samples with O/Nb atomic ratio less than 0.058 and at Tr_4 for the mixture of $Nb(s)$ and $NbO(s)$. The change of slope at Tr_4 corresponds to the transition from the mixture of $Nb(s)$ and $NbO(s)$ to the mixture of the liquidus solution and $Nb(s)$ as is discussed already. From
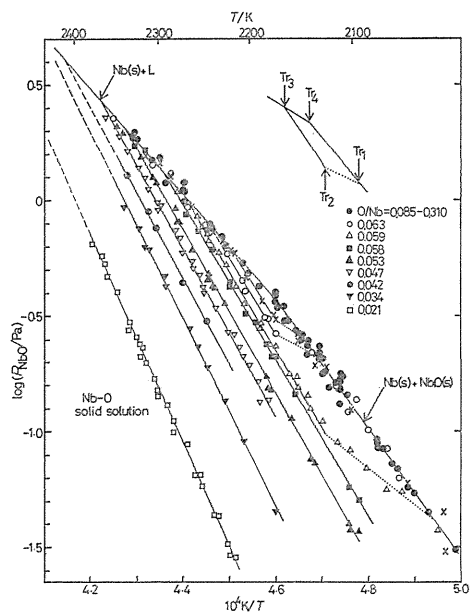
Fig. 68. Partial vapor pressures of NbO(g) over the niobium-oxygen solid solution as a function of the reciprocal temperatures.[106]

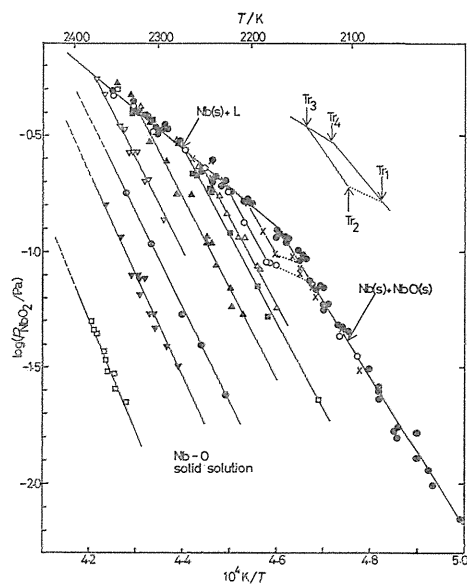Fig. 69. Partial vapor pressures of NbO$_2$(g) over the niobium-oxygen solid solution as a function of the reciprocal temperatures.[106] The meanings of symbols used in this figure are the same as those in Fig. 68.

the X-ray results, it can be concluded that the deviation from linearity at Tr$_1$ corresponds to the transition from the mixture of Nb(s) and NbO(s) to the single Nb phase (niobium-oxygen solid solution), and the slope change at higher temperature at Tr$_3$ corresponds to the transition from the solid solution to the mixture of liquidus solution and Nb(s).

6. 3. Phase equilibria

Phase equilibria in the niobium-oxygen system have been studied by many investigators and the existence of many oxide phases has been reported between NbO$_2$ and Nb$_2$O$_5$[115]. The phase relation and the existence region of several oxides between NbO$_2$ and Nb$_2$O$_5$ below 1700 K proposed recently by the authors[114] are shown in Fig. 70. The phase relations at high temperature above 1700 K have been investigated only by Elliott with metallographic technique[112]. Compared with the methods usually adopted for the study of phase equilibria, such as metallography, X-ray diffractometry, E. M. F. measurements and microcalorimetry, the mass-spectrometric method may be the only method applicable for the study on the phase relations at high temperature above 1700 K. Based on the vapor pressure measurements by the authors[102, 103, 105, 106], the homogeneity range of nonstoichiometric NbO$_{2\pm x}$, liquidus and solidus line around NbO$_{2\pm x}$, NbO and Nb$_2$O$_5$ and solubility limit of oxygen in niobium metal and solidus line of the niobium-

Fig. 70. Tentative phase diagram between NbO₂ and Nb₂O₅ at high temperatures.[114]

Fig. 71. Phase diagram of the Nb-O system.[104]

oxygen solid solution are determined as shown in Fig. 71, where the results by Elliott[112] are also shown.

The oxygen partial pressures for the system between the niobium-oxygen solid solution and $NbO_{2\pm x}$ above 1900 K calculated from the partial pressures of NbO_2 (g) and NbO (g)[102, 103, 105, 106, 115] are plotted against reciprocal temperature in Fig. 72.

The vapor pressures (total vapor pressure, $NbO_2(g)$, $NbO(g)$, $O(g)$ and $O_2(g)$)

Fig. 72. Oxygen potential diagram for the system between Nb and NbO₂ at high temperature.[104]

Fig. 73. Pressure-composition diagram for the Nb-O system.[104]

for the Nb-O system at 2073 K are shown as a function of composition in Fig. 73. This pressure-composition diagram also shows that NbO_2 is the only congruently vaporizing phase and the congruently vaporizing composition is stoichiometric $NbO_{2.000}$.

The relation between vapor pressures including niobium species and oxygen partial pressures for the Nb-O system at 2073 K is also shown in Fig. 74, which is useful to show the existing solid phases and the predominant vapor species as a function of oxygen partial pressure at a temperature.
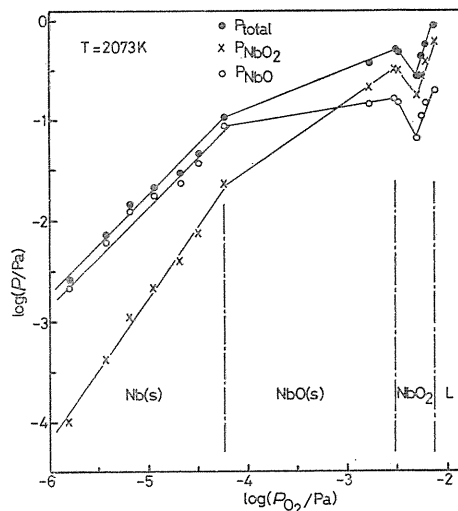

Fig. 74. Relation between vapor pressures for the Nb-O system.

6. 4. Thermodynamic properties

6. 4. 1. Enthalpies of formation for $NbO_2(g)$ and $NbO(g)$

By combining the enthalpies of vaporization obtained in the present study with the following values taken from the JANAF tables: $\Delta H_f^\circ(NbO_2, s, 298.15K) = -795.0$ kJ·mol^{-1}, $\Delta H_f^\circ(NbO_2, l, 298.15K) = -710.9$ kJ·mol^{-1}, $\Delta H_f^\circ(NbO, s, 298.15K) =$

Table 6. Enthalpy of formation and dissociation energy for $NbO_2(g)$.

Reactions used for calculation	$\Delta H_{f,298}^\circ(NbO_2, g, 298.15K)$ kJ·mol^{-1}		$D^\circ(NbO_2, g, 298.15K)$ kJ·mol^{-1}		Method	ref.
	2 nd law	3 rd law	2 nd law	3 rd law		
$2NbO(s) = NbO_2(g) + Nb(s)$	−223.0	——	(352.1 ± 3.0)[a]	——	M. E.[b]	99
	−220.9	−212.1	(347.2)	(345.1)	M. S.[c]	101
	−160.8±23.4	−163.1±1.7	332.9±5.5	333.4±0.5	M. S.	105
$2NbO(l) = NbO_2(g) + Nb(s)$	−172.8	−208.8	(335.7)	(344.4)	M. S.	101
$NbO_2(s) = NbO_2(g)$	−200.8	−195.0	(342.4)	(341.0)	M. S.	107[d]
	−210.9±41.4	−167.3±2.1	344.9±9.9	334.5±0.5	M. E.	102
	−189.0±9.3	−167.0±1.4	339.6±2.3	334.3±0.2	M. S.	102
$NbO_2(l) = NbO_2(g)$	−195.8	−193.7	(340.1)	(340.8)	M. S.	107
	−191.0±12.4	−164.9±0.9	340.1±3.0	333.8±0.2	M. S.	102

a) The valus in parenthesis are calculated from the original data in the literature by the present authors.

b) Mass-effusion (weight loss measurement) method.

c) Mass-spectrometric method.

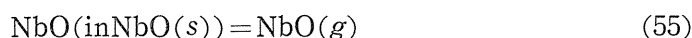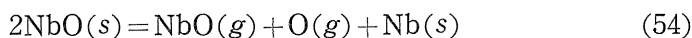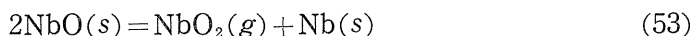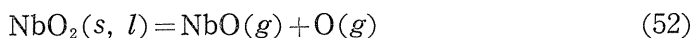d) The values in the JANAF Tables are calculated based on the original data measured by Shchukarev et al.[101]

Table 7. Enthalpy of formation and dissociation energy for NbO(g).

Reaction used for calculation	$\Delta H^{\circ}_{f,298}$(NbO,g,298.15K) kJ·mol^{-1}		D°(NbO, g, 298.15K) kJ·mo^{-1}		Method	ref.
	2 nd law	3 rd law	2 nd law	3 rd law		
NbO(in NbO(s))=NbO(g)	199.6	197.5	(187.3)[a]	(187.8)	M. S.	107[b]
	170.5±34.3	181.9±2.5	(194.2±8.3)	191.5±0.7	M. S.	105
NbO(in NbO(l))=NbO(g)	199.2	198.7	(187.3)	(187.3)	M. S.	107
2NbO(s)=NbO(g)+O(g)+Nb(s)	156.2±25.8	135.8±1.7	(197.7±6.2)	(202.5±0.2)	M. S.	105
NbO$_2$(s)=NbO(g)+O(g)	(211.4)	(165.4)	(184.3)	(195.4)	M. S.	101
	155.7±41.7	134.6±4.7	(197.7±9.9)	202.8±1.15	M. E.	102
	129.0±16.2	131.6±1.9	(203.9±3.9)	203.4±0.5	M. S.	102
NbO$_2$(l)=NbO(g)+O(g)	(179.6)	(152.0)	(191.9)	(198.6)	M. S.	101
	137.9±24.9	127.1±2.9	(201.8±6.0)	(204.6±0.7)	M. S.	102

a) The values in parenthesis are calculated from the original data in the literature by the present authors.

b) The values in the JANAF Tables are calculated from the original data measured by Shchukarev *et al.*[101].

−419.7 kJ·mol^{-1}, ΔH°_f(Nb, g, 298.15K)=733.0 kJ·mol^{-1} and ΔH°_f(O, g, 298.15 K)= 249.2 kJ·mol^{-1}, both enthalpies of formation and dissociation energies for NbO$_2$(g) and NbO(g) are calculated. The results are summarized in Tables 6 and 7 together with the previous results[98, 99, 101, 102, 105, 107], some of which are calculated by the authors based on the original data.

The enthalpies of formation and the dissociation energies of NbO$_2$(g) and NbO(g) determined from the enthalpies of vaporization of the stoichiometric NbO$_2$ for the reactions (51) and (52) by means of a combination of mass-effusion (weight loss measurement) and mass-spectrometric methods[102, 103] are in good agreement with those determined from the reactions (53) and (54)[105] within the experimental error, except the third law values determined from the reaction (55).

$$NbO_2(s, l)=NbO_2(g) \qquad (51)$$

$$NbO_2(s, l)=NbO(g)+O(g) \qquad (52)$$

$$2NbO(s)=NbO_2(g)+Nb(s) \qquad (53)$$

$$2NbO(s)=NbO(g)+O(g)+Nb(s) \qquad (54)$$

$$NbO(inNbO(s))=NbO(g) \qquad (55)$$

The difference between the values for NbO(g) calculated from the reaction (55) and those calculated from the reaction (54) may be attributed to the assumption of unit activity of NbO in the sample of NbO$_{1.003}$(s). The data for NbO$_2$(g) and NbO(g) determined from the reactions (53) and (54) are thought to be more reliable than those from the reactions (55), since the reactions (53) and (54) are univariant systems containing three phases (2 solid+vapor).

6. 4. 2. The partial molar thermodynamic quantities of oxygen and defect structures

From the oxygen partial pressures, the partial molar thermodynamic quantities (the partial molar enthalpy of oxygen and the partial molar entropy of oxygen) are determined.   The results obtained by mass-spectrometry in our study[103, 104, 105, 106, 115] are summarized in Figs. 75 and 76 together with the previous results determined by E. M. F. method [116~121], thermogravimetry[119, 83], gas equilibration[121], electrical conductivity measurements[121, 122] and micro-calorimetry[119, 123].

The partial molar enthalpies and entropies of oxygen in the niobium-oxygen solid solutions are fairly in good agreement with each other considering the differences in the methods and the temperatures of the measurements.   The partial
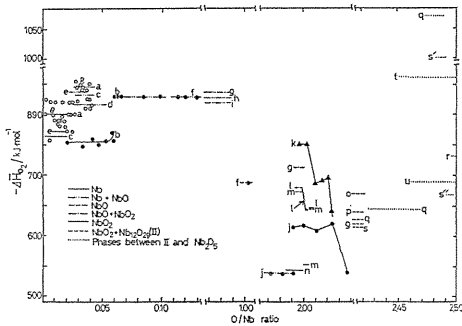

Fig. 75. Partial molar enthalpies of oxygen in the niobium-oxygen system[115]
a: ○[123], b: ◉[106], c[116], d[125], e[120], f: ◉[105] g[129], h[126], i[127], j: ◉[103], k: ▲[118], l (calorimetry)[119], m (TGA, EMF)[119], n[117], o[128], p[121], q: $NbO_{2.42}+NbO_{2.47}$[83], r: Nb_2O_{5-x}[124], s: $NbO_2+Nb_{12}O_{29}$[131], s′: IV+V[131], s″: V+Nb_2O_{5-x}[131], t[123], u[132].
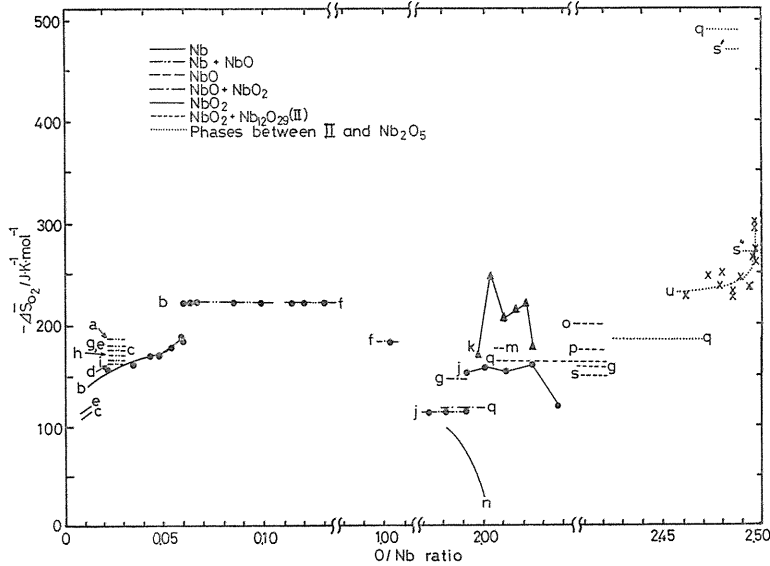
Fig. 76. Partial molar entropies of oxygen in the niobium-oxygen system[115]
a[131], b: ◉[106], c[116], d[125], e[120], f: ◉[105], g[129], h[126], i[127], j: ◉[103], k: ▲[118], m: (EMF)[119], n[117], o[128], p[121], q: $NbO_{2.42}+NbO_{2.47}$[83], s: $NbO_2+Nb_{12}O_{29}$[131], s′: IV+V[131], s″: V+Nb_2O_{5-x}[131], u: x[132].

molar enthalpies of oxygen determined by the authors[106] and by Boureau et al.[123] are nearly constant independent of composition, indicating the presence of weak interactions between interstitial oxygens. The compositional dependence of the partial molar entropies of oxygen determined by the authors[106] can be explained by assuming the occupancy of octahedral sites by the interstitial oxygen in the niobium-oxygen solid solutions. The relation between composition and oxygen partial pressure determined by mass spectrometry at high temperatures 2091-2379 K[106] was found to obey the Henry's law at low oxygen compositions less than about 4 a/o, which also indicates that the oxygen interstitial behaves ideally in the solid solution.

The partial molar enthalpy and entropy of oxygen in $NbO_{1.003}$ are determined to be -688 ± 73 kJ·mol^{-1} and -183 ± 36 J·K^{-1}·mol^{-1}, respectively, by mass spectrometry[105]. The compositional dependence of $NbO_{1\pm x}$ has not been known yet because of the narrow homogeneity range.

The partial molar enthalpies and entropies of oxygen in nonstoichiometric $NbO_{2\pm x}$ have been reported by some investigators[103, 117~119], but there is still some disagreement. The compositional dependence of these quantities determined by the authors[103] shows a complicated change as shown in Figs. 75 and 76. A similar dependence is seen from the results by Vasileva et al[118]. This irregular dependence in the region of large departure from stoichiometric NbO_2 may indicate the presence of a series of different kinds of short range ordering.

The relations between composition (x) and oxygen partial pressure (P_{O_2}) of $NbO_{2\pm x}$ determined by E. M. F. measurements[117, 118], thermogravimetry[119] and mass spectrometry[103] are summarized in Fig. 77, from which the values of n($\log x \propto 1/n \log P_{O_2}$) are observed to be -1 and $+1$ at 1273 K, for hypostoichiometric NbO_{2-x}[117] and hyperstoichiometric NbO_{2+x}[118,119], respectively.

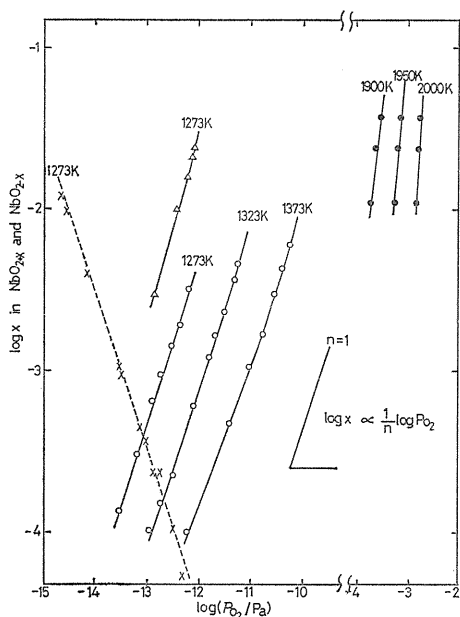Although it is difficult to discuss the defect structure of $NbO_{2\pm x}$, which

Fig. 77. The relation between composition and oxygen partial pressure for $NbO_{2\pm x}$[115]
———: NbO_{2+x}, ●[103], △[118], ○[119],
- - -: NbO_{2-x}, x[117].

shows both metallic and semiconducting behavior[114, 133, 134], the predominant defects for NbO_{2-x} and NbO_{2+x} may be estimated to be interstitial niobium and niobium vacancies, respectively, for either case of an intrinsic semiconductor or a metallic conductor. As also seen in Fig. 77, the slopes for NbO_{2+x}[117, 118] become larger than unity in the region of large departure from stoichiometric NbO_2 except that at 1273 K[117] and more larger slopes are obtained at higher temperatures from 1900 to 2000 K[103]. These slope changes and large slopes suggest the possibility of the coexistence of another type of defects such as niobium divacancies and tri-vacancies.

The partial molar enthalpies and entropies of oxygen in the oxides between NbO_2 and Nb_2O_5 so far reported[83, 119, 122, 129, 131, 132] are not in good agreement. However, according to the classification of homologous phases based on the recent results[114], some of the previous values[130, 131, 132] can be classified into those for the differnt phases[115]. As seen in Figs. 75 and 76, both values of partial molar enthalpy and entropy of oxygen change considerably from phase to phase, which reflects the presence of the different defect structure of each phase in this system[114, 115, 135~137].

6. 5. *Vaporization studies on the* V-O *and* Ta-O *systems*

Vanadium and tantalum are the same 5A group metals in the periodic table as niobium. Vapor pressure measurements on the V-O and Ta-O systems have also been carried out by several investigators[138~146]. The vapor pressures of V(g)
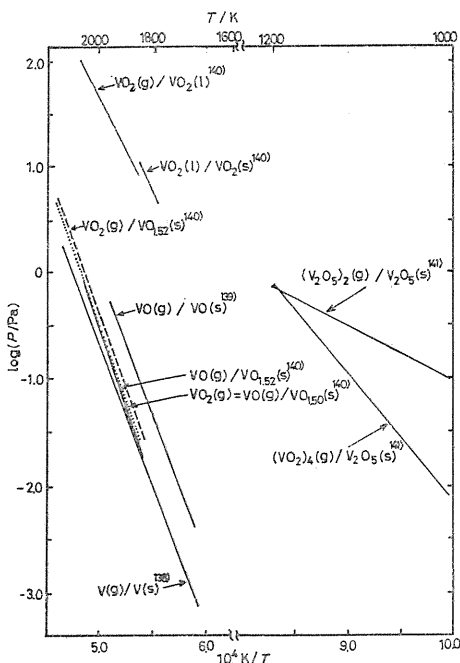

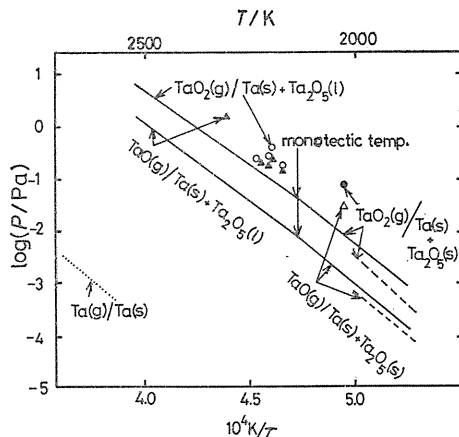Fig. 78. Vapor pressures over the vanadium-oxygen system.

Fig. 79. Vapor pressures over the tantalum-oxygen system: Ta(g)/Ta(s)[142], ——$TaO_2(g)$, TaO(g)/Ta(s)+$Ta_2O_5(s, l)$mixture[145], ---$TaO_2(g)$, TaO(g)/Ta(s)+Ta_2O_5(s) mixture[146], ○: $TaO_2(g)$/Ta(s)+$Ta_2O_5(l)$ mixture[144], ●: TaO_2(g)/Ta(s)+Ta_2O_5(s) mixture[144], ▲: TaO(g)/Ta(s)+$Ta_2O_5(l)$ mixture[144], △: TaO(g)/Ta(s)+Ta_2O_5(s) mixture[144].

over $V(s)$[138], $VO(g)$ over $VO(s)$[139], $VO_2(g)$ and $VO(g)$ over $V_2O_3(s)$[140], $VO_2(g)$ over $VO_2(s, l)$[140], $(VO_2)_4(g)$ and $(V_2O_5)_2(g)$ over $V_2O_5(s)$[141] are summarized in Fig. 78. The vapor pressures of $Ta(g)$ over $Ta(s)$[142] and $TaO(g)$ and $TaO_2(g)$ over two-phase $Ta(s)+Ta_2O_5(s)$ mixture[143~146] are also shown in Fig. 79. These figures show that the vapor pressures over metal are lower than those over metal oxides in the V–O and Ta–O systems like Nb–O system as was already described. These V, Nb, Ta metals can be purified during vaporization because of higher oxygen content of gaseous phases than solid phase. Figure 78 also suggests that $V_2O_3(s)$ is the congruently vaporizing phase in the V–O system. On the other hand there seems to be no congruently vaporizing phase in the Ta–O system as seen from Fig. 79. The recent results of the vapor pressure measurements on the other refractory metal-oxygen systems (4A and 6A groups in the periodic tables) have been reviewed elsewhere[147].

VII. Concluding Remarks

As described above, the calorimetric study includes the measurements of heat capacity and heat of formation by means of various methods.

The heat capacity data of a solid material are necessary for obtaining the free energy function, and the free energy change of a reaction at any temperature can be calculated with use of the free energy functions of the materials concerned together with the data of heat of formation of the materials at a reference temperature. It means that the data of heat capacity and heat of formation enable us to calculate the free energy change of a reaction at any temperature, in other words, the occurrence of any reaction can be predicted by these data. In this sense, calorimetric study gives us the most basic data of the materials, especially at high temperatures because the reaction is expected to be accelerated as the temperature rises.

In addition, the calorimetric study on the materials gives us the informations about the phase relation, the lattice dynamics, the defect structure, etc., which are also very valuable to understand the behavior or stability of the materials as seen in this review.

Although the calorimetric studies have been carried out extensively in our laboratory in recent years, the measurement of heat capacity is limited up to about 1300 K and that of vapor pressure is about 2400 K. The needs for thermal data at higher temperatures are increasing recently in relation to the research and development of high temperature materials, especially in the field of energy or space technology. The calorimetric studies at higher temperature are awaited as well as the increase of precision of the measurement.

Acknowledgement

References

1) K. Naito, N. Kamegashira, N. Yamada and J. Kitagawa, J, Phys. E: Sci. Instrum. **6**, 836 (1973).
2) K. Naito, H. Inaba, M. Ishida, Y. Saito and H. Arima, J. Phys, E. Sci. Instrum. **7**, 464 (1974).
3) J. T. Furukawa, T. B. Douglas. R. E, McCoskey and D. C. Grimmings, J. Res. Nat. Bur. Stand. **57**, 67 (1956).
4) K. Naito, H. Inaba, M. Ishida and K. Seta, J. Phys. E: Sci. Instrum. **12**, 712 (1979).
5) A. T. D. Butland and R. J. Madison, J. Nucl. Mater. **47**, 45 (1973).
6) A. Magnus, Ann. Phys. Lpz. **70**, 303 (1923).
7) Y. Ya Chekhovskoy, J. Chem. Thermodyn. **3**, 287 (1971).
8) F. Grϕnvold, Acta Chem. Scand, **21**, 1695 (1967).
9) Y. Takahashi, H. Yokodawa, H. Kadokura, Y. Sekine and T. Mukaibo, J. Chem. Thermodyn. **11**, 379 (1979).
10) K. Naito, H. Inaba, S. Takahashi and T. Mima, Unpublished data.
11) K. Naito, H. Inaba and Y. Noda, J. Nucl. Sci. Technol. **13**, 508 (1976).
12) D. W. Lee and W. D. Kingery, J. Am. Ceram. Soc. **43**, 594 (1960).
13) J. R. White and A. E. Cameron, Phys. Rev. **74**, 991 (1948).
14) R. E. Honing and D. A. Kramer, Techniques of Metals Research, vol. 1, p. 505 (Interscience, New York, 1970).
15) J. B. Mann, J. Chem. Phys. **46**, 1646 (1967).
16) J. W. Otvos and D. P. Stevenson, J. Am. Chem. Soc. **78**, 546 (1956).
17) D. C. Damoth, Dynamic Mass Spectrometry, The 2 nd European Symposium on the Time-of-Flight Mass Spectrometer P. 199 (Hayden and Sons, Ltd., 1970).
18) B. L. Schram, A. J. H. Boerboom, W. Kleine and J. Kistemader, Physica **32**, 749 (1966).
19) K. Naito and N. Kamegashira, Adv. in Nucl. Sci. and Technol. **9**, 99 (1976).
20) K. Gotoo and K. Naito, J. Phys. Chem. Solids, **26**, 1673 (1965).
21) E. F. Westrum, Y. Takahashi and F. Grϕnvold, J. Phys. Chem. **69**, 3192 (1965).
22) K. Naito, J. Nucl. Mater. **51**, 126 (1974).
23) H. Inaba and K. Naito, Netsusokutei **4**, 10 (1977).
24) H. Inaba and K. Naito, J. Nucl. Mater. **49**, 181 (1973).
25) T. Ishii, K. Naito, K. Oshima and Y. Hamaguchi, J. Phys. Chem. Solids **32**, 235 (1971).
26) B. T. M. Willis, J. Phys. **25**, 431 (1964).
27) H. Inaba, T. Matsui and K. Naito, J. Nucl. Mater. **58**, 115 (1975).
28) H. Inaba, S. Ono and K. Naito, J. Nucl. Mater. **64**, 189 (1977).
29) Y. Noda and K. Naito, J. Nucl. Mater. **66**, 17 (1977).
30) K. K. Seta, T. Matsui, H. Inaba and K. Naito, J. Nucl. Mater. **110**, 47 (1982).
31) K. Naito, T. Tsuji and T. Matsui, J. Nucl. Mater. **48**, 58 (1973).
32) F. Grϕnvold, N. J. Kyeseth, A. Syeen and J. Tichý, J. Chem. Thermodyn. **2**, 665 (1970).
33) A. C. MacLeod, J. Chem. Thermodyn. **4**, 699 (1972).
34) H. L. Girdhar and E. F. Westrum, J. Chem. Eng. Data **13**, 531 (1968).
35) H. Inaba, H. Shimizu and K. Naito, J. Nucl. Mater. **64**, 66 (1977).
36) K. Naito, H. Inaba and S. Takahashi, J. Nucl. Mater. **110**, 317 (1982).
37) B. O. Loopstra, J. Appl. Cryst. **3**, 94 (1970).
38) R. J. Ackermann, A. R. Chang and C. A. Sorrell, J. Inorg. Nucl. Chem. **39**, 75 (1977).
39) Y. Noda and K. Naito, J. Nucl. Mater. **80**, 102 (1979).

40) J. F. Kerrisk and D. G. Clifton, Nucl. Technol. **16**, 531 (1972).
41) D. R. Fredrickson and M. G. Chasanov, J. Chem. Thermodyn. **2**, 623 (1970).
42) R. A. Hein, P. N. Flagella and J. B. Conway, J. Am. Ceram. Soc. **51**, 291 (1968).
43) R. A. Hein, L. H. Sjodahl and R. Szwarc, J. Nucl. Mater. **25**, 99 (1968).
44) A. E. Ogard and J. A. Leary, "Symposium of Thermodynamics of Nuclear Materials" (IAEA, Vienna, 1967).
45) C. Affortit and J. -P. Marcon, Rev. Int. Hautes Temper. Refract. **7**, 236 (1970).
46) R. Szwarc, J. Phys. Chem. Solids **30**, 705 (1969).
47) J. H. Harding, P. Masri and A. M. Stoneham, J. Nucl. Mater. **92**, 73 (1980).
48) C. R. A. Catlow, Proc. Roy. Soc. (London) **A353**, 533 (1977).
49) R. J. Thorn, G. H. Winslow and J. S. Zeomek, J. Nucl. Mater. **87**, 416 (1979).
50) P. Browing, J. Nucl. Mater. **98**, 345 (1981).
51) Y. Noda, Doctoral Dissertation of Nagoya University (1979).
52) A. M. Ross, USAEC Report, CRFD-817, AECL-1096 (1960).
53) I. C. Hobson, R. Taylor and J. B. Ainscough, J. Phys. D: Appl. Phys., **7**, 1003 (1974).
54) L. A. Goldsmith and J. A. M. Douglas, J. Nucl. Mater. **47**, 31 (1973).
55) H. E. Schmidt, High Temp. -High Press. **3**, 345 (1971).
56) K. Naito, H. Inaba and H. Yagi, J. Solid State Chem. **36**, 28 (1981).
57) N. W. Grimes, Spectrochim. Acta Part A **28**, 2217 (1972).
58) F. Grϕnvold and A. Sveen, J. Chem. Thermodyn. **6**, 859 (1974).
59) V. A. M. Brabers, J. Phys. Chem. Solids **32**, 2181 (1971).
60) A Navrotsky and O. J. Kleppa, J. Inorg. Nucl. Chem. **29**, 2701 (1967).
61) Y. Noda and K. Naito, Netsusokutei **5**, 11 (1978).
62) I. K. Kailov, G. M. Shakhshaev, Kh. K. Aliev, G. G. Musaev and M. M. Khamidov, Zh. Eksp. Teor. Fiz. **68**, 586 (1975).
63) V. V. Shchelkotunov, V. N. Danilov and V. V. Lyukshin, Izv. Akad. Nauk SSSR Neorg. Mater. **11**, 1638 (1975).
64) B. Abeles, Phys. Rev. **131**, 1906 (1963).
65) E. W. Gorter, Philips Res. Rep. **9**, 295 (1954).
66) G. D. Rieck and F. C. M. Driessens, Acta Cryst. **20**, 521 (1966).
67) H. Inaba, S. Nakashima and K. Naito, J. Solid State Chem. **41**, 213 (1982).
68) T. Inoue and S, Iida, J. Phys. Soc. Japan, **13**, 656 (1958).
69) M. L. Bochirol, Compt. rend. **232**, 1474 (1951).
70) T. Sakata, K. Sakata and I. Mishida, Phys. Status Solidi **20**, K155 (1967).
71) R. F. Janninck and D. H. Whitemore, J. Phys. Chem. Solids **27**, 1183 (1966).
72) K. Seta and K. Naito, J. Chem. Thermodyn. **14**, 921 (1982).
73) E. G. King, J. Am. Chem. Soc. **80**, 1799 (1958).
74) W. F. Boyle, J. G. Bennett, S. H. Shin and R. J. Sladek, Phys. Rev. **B14**, 526 (1976).
75) F. G. Kuzenko and P. V. Geld, Izv. Vys. Uch. Zav. Tav. Met. **3**, 102 (1960).
76) T. Mitsuhashi and Y. Takahashi, Yogyo-Kyokai-Shi 88, 9 (1980).
77) P. M. Raccah, U. S. NITIS, AD Rep. AD A041509 (1977).
78) K. Seta and K. Naito, J. Chem. Thermodyn. **14**, 937 (1982).
79) C. N. R. Rao, G. R. Rao and G. V. S. Rao, J. Solid State Chem. **6**, 340 (1973).
80) F. Pintchovski, W. S. Glaunsinger and A. Navrotsky, J. Phys. Chem. Solids **39**, 941 (1978).
81) K. Naito, H. Inaba and T. Mima, Unpublished data.
82) M. W. Chase, J. L. Curnutt, H. Prophet et al., JANAF, Thermochemical Tables, Second Edition (1971), Supplement (1974).
83) J. F. Marucco, J. Solid State Chem. **10**, 211 (1974).
84) T. V. Charlu and O. J. Kleppa, High Temp. Sci. **5**, 260 (1973).
85) K. Hiraga and M. Hirabayashi, Trans. JIM **16**, 431 (1975).
86) H. Inaba, S. Tsujimura and K. Naito, J. Solid State Chem. **46**, 162 (1982).
87) J. D. Greiner, O. N. Carlson, and J. F. Smith, J. Appl. Phys. **50**, 4394 (1979).
88) V. V. Sumin, S. A. Danilkin, and S. I. Morozov, Sov. Phys. Solid State **20**, 1001 (1978).

89) M. Shimizu, T. Takahashi and A. Katsuki, J. Phys. Soc. Japan 18, 1192 (1963).
90) R. Kohlhaas, M. Braun and O. Vollmer, Z. Naturforsch. A20, 1077 (1965).
91) R. L. Orr, J. Am. Chem. Soc. 76, 857 (1954).
92) P. V. Gel'd and F. G. Kusenko, Russ. Met. Fuels. 2, 43 (1960).
93) O. A. Cook, J. Am. Chem. Soc. 69, 331 (1947).
94) J. M. D. Coey, Phisica. 91B, 59 (1977).
95) G. V. Chandroshekhar, H. L. Barros and J. M. Honig, Mat. Res. Bull. 8, 369 (1973).
96) R. L. Orr, J. Am. Chem. Soc. 75, 2808 (1953).
97) L. V. Golubtsov, A. V. Lapitskii and V. K. Shiryaev, Izv. Vysshekh Uchebn. Zavede-nii, Khim. i Khim. Tekhnol. 3, 571 (1960).
98) S. A. Shchukarev, G. A. Semenov and K. E. Frantseva, Russ. J. Inorg. Chem. 4, 1217 (1959).
99) S. A. Shchukarev, G. A. Semenov and K. E. Frantseva, Izv. Vysshekh Uchebn. Za-vedenii, Khim. i Khim. Tekhnol. 5, 691 (1962).
100) S. A. Shchukarev, G. A. Semenov and K. E. Frantseva, Dokl. Akad. Nauk SSSR 145, 119 (1962).
101) S. A. Shchukarev, G. A. Semenov and K. E. Frantseva, Russ. J. Inorg. Chem. 11, 129 (1966).
102) N. Kamegashira, T. Matsui, M. Harada and K. Naito, J. Nucl. Mater. 101, 207 (1981).
103) T. Matsui and K. Naito, J. Nucl. Mater. 102, 227 (1981).
104) T. Matsui and K. Naito, 9 th Int. Mass Spectr. Conf., Vienna, Austria, Sept. 1982., Intern. J. Mass Spectr. and Ion Phys. 47, 253 (1983).
105) T. Matsui and K. Naito, J. Nucl. Mater. 107, 83 (1982).
106) T. Matsui and K. Naito, J. Nucl. Mater. 115, 178 (1983).
107) M. W. Chase, J. L. Curnutt, H. Prophet et al., JANAF Thermochemical Tables, 1975 supplement.
108) R. L. Orr, J. Amer. Chem. Soc. 75, 2808 (1953).
109) E. G. Rauh and S. P. Garg, J. Amer. Ceram. Soc. 63, 239 (1980).
110) W. H. Olson and R. N. R. Mulford, J. Phys. Chem. 69, 1223 (1965).
111) B. L. Davydov. Zh. Neorg. Khim. 2, 1460 (1957).
112) R. P. Elliott, Trans. Am. Soc. Metals 52, 990 (1960).
113) F. Holtzberg, A. Reisman, M. Berry and M. Berkenblit, J. Amer. Chem. Soc. 79, 2039 (1957).
114) K. Naito, N. Kamegashira and N. Sasaki, J. Solid State Chem. 35, 305 (1980).
115) K. Naito and T. Matsui, 2 nd Int. Conf. on Transport in Nonstoichiometric Compounds, Perpignan, France, June 1982, to be published in Solid State Ionics (1983).
116) W. Nickerson and C. Altstetter, Scripta Met. 7, 229 (1973).
117) C. B. Alcock, S. Zador and B. C. H. Steele, Proc. Brit. Ceram. Soc. 8, 231 (1967).
118) I. A. Vasileva, J. I. Gerasimov and L. P. Ogotodova, Dokl. Akad. Nauk SSSR 232, 355 (1977).
119) J. F. Marucco, R. Tetot, P. Gerdanian and C. Picard, J. Solid State Chem. 18, 97 (1976).
120) E. Fromm, J. Less Common Metals 22, 139 (1970).
121) W. L. Worrell, J. Phys. Chem. 68, 952 (1964).
122) P. Kofstad and P. B. Anderson, J. Phys. Chem. Solids 21, 280 (1961).
123) G. Boureau and P. Gerdanian, J. Phys. Chem. Solids 42, 749 (1981).
124) J. M. Wimmer and W. C. Tripp, ARL 73-0157 (1973).
125) I. A. Vasileva et al., Zh. Fiz. Khim. 49, 2169 (1975).
126) S. Ignatowitz and M. W. Davies, J. Less Common Metals 15, 100 (1968).
127) V. N. Drovyshev and T. N. Rezukhina, Zh. Fiz. Khim. 39, 151 (1965).
128) J. P. Delmaire, N. Wallet and A. Duguesnoy, Comt. Rend. Acad. Sci. Paris 264, 1290 (1967).
129) W. L. Worrell, Thermodynamics, IAEA, Vienna, (SM-66/66), p. 130 (1966).
130) B. C. H. Steele and C. B. Alcock, Trans. Met. Soc. AIME 233, 1359 (1965).

131) K. Naito, N. Kamegashira and N. Sasaki, unpublished data.
132) R. N. Blumenthal, J. B. Moser and D. H. Whitmore, J. Amer. Ceram. Soc. **48**, 617 (19 65).
133) R. F. Janninck and D. H. Whitmore, J. Phys. Chem. Solids **27**, 1183 (1966).
134) J. A. Roberson and R. A. Rapp, J. Phys. Chem. Solids **30**, 1119 (1969).
135) H. Schäfer, D. Bergner and R. Gruehn, Z. Anorg. Allegem. Chem. **31**, 365 (1969).
136) S. Kimura, J. Solid State Chem. **6**, 438 (1973).
137) T. Kikuchi and M. Goto, J. Solid State Chem. **16**, 363 (1976).
138) J. W. Edwards, H. L. Johnston and P. E. Blackburn, J. Chem. Phys. **73**, 4727 (1951).
139) J. Berkowitz, W. A. Chupka and M. G. Inghram, J. Chem. Phys. **27**, 87 (1957).
140) K. E. Frantseva and G. A. Semenov, Teplofizika Vysokihl Temperature **7**, 55 (1969).
141) M. Farber, O. Manuel Uy and R. D. Srivasteva, J. Chem. Phys. **56**, 5312 (1972).
142) J. W. Edwards, H. L. Johnston and P. E. Blackburn, J. Chem. Phys. **73**, 172 (1951).
143) M. Farber and R. D. Srivastava, J. Chem. Soc. Faraday Trans. I. Phys. Chem. **69**, 390 (1973).
144) M. G. Inghram, W. Chupka and J. Berkowitz, J. Chem. Phys. **27**, 569 (1957).
145) S. Smoes, J. Drowart and C. E. Myers, J. Chem. Thermodynamics **8**, 225 (1976).
146) F. De Greve and J. Drowart, J. Rev. ATB Metallurg. **6**, 115 (1966).
147) T. Matsui and K. Naito, Measurement of heat and temerature and Thermal analysis, Kagakugijutsusha (1983).